INSTITUTO TECNOLÓGICO
Y DE ESTUDIOS SUPERIORES DE OCCIDENTE

Reconocimiento de validez oficial de estudios de nivel superior según acuerdo secretarial 15018,
publicado en el Diario Oficial de la Federación el 29 de noviembre de 1976.

Departamento de Electrónica, Sistemas e Informática

Doctorado en Ciencias de la Ingeniería

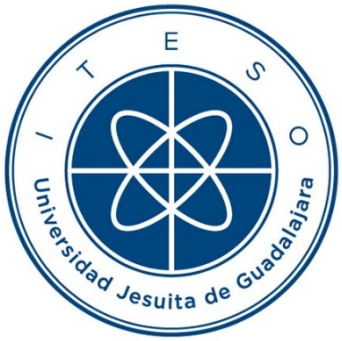

ESTIMACIÓN DE ESTADOS PARA NAVEGACIÓN POR MEDIO DE FILTRO DE KALMAN Y SENSORES DE BAJO COSTO

Tesis que para obtener el grado de
Doctor en Ciencias de la Ingeniería
presenta: Raúl Arturo García Huerta

Director de tesis: Dr. Iván Esteban Villalón Turrubiates
Co-director de tesis: Dr. Luis Enrique González Jiménez

Tlaquepaque, Jalisco. Noviembre de 2020

TÍTULO:	**Estimación de estados para navegación por medio de filtro de Kalman y sensores de bajo costo**
AUTOR:	Raúl Arturo García Huerta Ingeniero Mecánico (ITESO, México) Maestro en Ciencia y Tecnología Espacial (Universidad Técnica de Múnich, Alemania)
DIRECTOR DE TESIS:	Iván Esteban Villalón Turrubiates Departamento de Electrónica, Sistemas e Informática, ITESO Ingeniero Mecánico (Universidad de Guanajuato, México) Maestro en Ingeniería Electrónica (Universidad de Guanajuato, México) Doctor en Ingeniería Electrónica (CINVESTAV, México) *Senior*, IEEE
NÚMERO DE PÁGINAS:	xxviii, 102

ITESO - The Jesuit University of Guadalajara

Departament of Electronics, Systems, and Informatics

Doctoral Program in Engineering Sciences

Kalman Filter State Estimation for Navigation Based on Low-Cost Sensors

Thesis to obtain the degree of

Doctor in Engineering Sciences

Presents: Raúl Arturo García Huerta

Thesis Director: Dr. Iván Esteban Villalón Turrubiates

Thesis Co-director: Dr. Luis Enrique González Jiménez

Tlaquepaque, Jalisco, Mexico

November 2020

TITLE:	**Kalman Filter State Estimation for Navigation Based on Low-Cost Sensors**
AUTHOR:	Raúl Arturo García Huerta Bachelor's in mechanical engineering (ITESO, Mexico) Master's in Space Science and Technology (Technical University of Munich, Germany)
THESIS DIRECTOR:	Iván Esteban Villalón Turrubiates Department of Electronics, Systems, and Informatics, ITESO Bachelor's degree in mechanical engineering (University of Guanajuato, Mexico) Master's degree in electrical engineering (University of Guanajuato, Mexico) Ph.D. degree in electrical engineering (CINVESTAV, Mexico) Senior, IEEE
NUMBER OF PAGES:	xxviii, 102

To my son Alejandro.

All I am, I devote it to you.

Resumen

Este trabajo de tesis doctoral presenta el desarrollo e implementación de un esquema de estimación basado en un filtro de Kalman, para la estimación de los estados de vehículos durante su navegación, fusionando mediciones provenientes de sensores de bajo costo. Los estados de interés para la navegación corresponden a los componentes que definen la posición y orientación de un vehículo. El incorporar información sobre la dinámica de movimiento del vehículo, en conjunto con mediciones obtenidas por medio de uno o varios sensores, favorece a la mejora de la precisión y exactitud con la que se pueden determinar dichos estados. En específico, se propone e implementa un esquema de estimación de estados para aplicaciones pedestres y aéreas. Para aplicaciones pedestres, se propone una metodología para mejorar la estimación de la posición por medio de imágenes aéreas. Adicionalmente, se estudia a profundidad la dinámica de vuelo de sistemas de entrega aérea de precisión, en específico sistemas campana-carga útil denominados micro ligeros. Para estos sistemas, se proponen dos modelos lineales que capturen su dinámica de vuelo, en los cuales se implementa el esquema de estimación de posición y orientación, fusionando mediciones de sensores de bajo costo por medio de un filtro de Kalman. Los resultados obtenidos muestran que la implementación del esquema de estimación es efectiva y viable para aplicaciones de bajo costo. Por un lado, la incorporación de imágenes aéreas en el proceso de estimación de la posición en aplicaciones pedestres permite determinar la exactitud de los sensores de navegación, así como mejorar el proceso de estimación de su posición. Los modelos lineales desarrollados para sistemas micro ligeros de entrega aérea de precisión demuestran capturar su dinámica de vuelo. La incorporación de estos modelos, junto con la fusión de mediciones de sensores de bajo costo en el esquema de estimación, demuestran una mejoría en la determinación de la posición y orientación de los vehículos durante su trayectoria de descenso.

Summary

The research in this doctoral thesis presents the development and implementation of an estimation scheme, based on a Kalman filter, for the state estimation of vehicles during navigation, fusing measurements from low-cost sensors. For navigation purposes, the states of interest are the components that define the position and attitude of the vehicle. The inclusion of information regarding the dynamics of the vehicle, together with measurements from one or several sensors, enhances the accuracy and precision to which the states can be determined. The proposed state estimation scheme is implemented in pedestrian and aerial applications. For pedestrian applications a methodology is developed, to improve the position estimation by using aerial images. Also, the flight dynamics of precision aerial delivery systems is studied thoroughly, specifically for micro-lightweight parafoil-payload systems. For these systems, two linear models that capture their flight dynamics are proposed and implemented in the state estimation scheme for position and attitude determination, fusing measurements from low-cost sensors employing a Kalman filter. The implementation results proved that the state estimation scheme is effective and suitable for low-cost applications. The incorporation of aerial images in the position estimation process for pedestrian applications allows for the accuracy determination of low-cost navigation sensors, as well as improving the estimation of the position. The lineal models developed for micro-lightweight precision aerial delivery systems proved to capture their flight dynamics. The use of these models, together with the fusion of measurements from low-cost sensors in the estimation scheme, demonstrates an improvement in the position and attitude determination of the vehicles during their descent trajectory.

Acknowledgments

It is the author's pleasure to acknowledge those who contributed to the intellectual, professional, and personal development related to this doctoral dissertation.

The author wishes to express his appreciation to Dr. Iván Esteban Villalón Turribiates, professor of the Department of Electronics, Systems, and Informatics at ITESO, for his supervision as doctoral thesis director throughout the course of this work. Particularly, for his encouragement related to the geoscience and remote sensing disciplines, conferences, and academic society.

The author offers his gratitude to Dr. Luis Enrique González Jiménez, professor of the Department of Electronics, Systems, and Informatics at ITESO, for his support as doctoral thesis co-director during the development of this work. Especially, for his insights related to control theory.

Special appreciation to Dr. Gerardo Allende Alba, for his selfless cooperation and willingness to contribute to this research. Notably, for the helpful technical discussions on satellite navigation, the formulation of the Kalman filter, and its performance evaluation.

The author gratefully acknowledges the support provided through ITESO's Program for Academic Level Enhancement (*Programa de Superación del Nivel Académico*, PSNA). Also, the author recognizes his colleagues at the Department of Technological and Industrial Processes, particularly, Dr. Carlos González Figueredo and Dr. Óscar Ariel Rojas Rejón for their constant support and thorough revision of this thesis.

Finally, special thanks are due to my family for their understanding, patience, and continuous loving support.

Contenido

Contents

List of Figures

List of Tables

List of Acronyms

ADC Analog-to-Digital Converter

AGAS Affordable Guided Airdrop System

ALEX Small Autonomous Parafoil Landing Experiment

AM Apparent Mass

CEP Circular Error Probability

CG Center of Gravity

COVID-19 Coronavirus disease 2019

DGPS Differential GPS

DOF Degree of Freedom

GNSS Global Navigation Satellite System

GPS Global Positioning System

IGRA Integrated Global Radiosonde Archive

IMU Inertial Measurement Unit

JPADS Joint Precision Airdrop System

LiDAR Light Detection and Ranging

NED North-East-Down coordinate system

NOAA National Oceanic and Atmospheric Administration

NWS National Weather Service

PADS Precision Aerial Delivery System

UAV Unmanned Aerial Vehicle

USA United States of America

UTC Universal Time Coordinate

UTM Universal Transverse Mercator

WGS84 World Geodetic System 1984

1. Introduction

This doctoral thesis presents the development and implementation of a state estimation scheme based on Kalman filters, for the position and attitude estimation of vehicles, fusing measurements from low-cost sensors. This estimation scheme is implemented for the navigation of pedestrian applications and aerial delivery systems.

A thorough exploration on the flight dynamics of aerial delivery systems is carried out, specifically for micro-lightweight systems. The state estimation scheme proposed in this research is implemented for the navigation trajectory of precision aerial delivery systems. All the calculations, data processing and plots presented in this thesis, were conducted using MATALB[1].

In the following sections, the motivation and background of the applications intended for this research are presented.

1.1. Low-Cost Satellite Navigation

Nowadays, there is a growing field of acquisition processes for remote sensing and surveying applications, based on aerial and terrestrial systems, like Unmanned Aerial Vehicles (UAVs), rovers, aerial delivery systems, and hand-held devices. These systems navigate on a trajectory while acquiring information on their surroundings. Whether the final product is the determination of characteristics of crop fields, monitoring natural reserves and disasters, the generation of data-sets for information extraction, precise farming, or digital elevation models, frequently the followed trajectory of the vehicle is required. Such a trajectory can be processed concurrently to data collection. Likewise, it can be used for the optimization of the intended trajectory (desired overlap in the scenes, georeferencing, energy efficiency, etc.) [Pajares-15; Manfreda-18].

Different strategies and equipment are used for the estimation of traveled trajectories, depending on the required accuracy, the payload capacity of the vehicle, and available resources. For applications demanding high accuracy, Harwin and Lucieer [Harwin-12] use Differential Global Positioning System and thousands of accurately determined ground control points to achieve $5\,\mathrm{cm}$ accuracy in

[1]MATLAB, Version 9.8.0, The MathWorks, Inc., 3 Apple Hill Drive, Natick MA 01760-2098, 2020.

point clouds. Benassi et al. [Benassi-17] incorporates dual-frequency Global Navigation Satellite System (GNSS) receivers and differential corrections provided by local ground stations to obtain accuracies at the $10\,\mathrm{cm}$ level. In addition, different applications of trajectory reconstruction making use of high-end sensors have proved effective to estimate the position of aerial and terrestrial systems at the meter level [Sanz-Ablanedo-18; Gong-19; Scheiner-19; Marucci-17; Adjrad-17; Kingston-04; Peng-00]. Although effective, these methods demand expensive and sometimes heavy sensors. Furthermore, they require the implementation of complex algorithms with high computational demand and therefore power consumption, not suitable for low-cost systems.

Miniaturized low-cost systems typically rely on affordable GPS receivers, making only use of single-frequency code measurements. Additionally, small vehicles have very limited payload capacities, constraining the allocated weight for structural components, energy storage, actuators, sensors, and processing units. For this reason, low-cost applications face the challenge of achieving the best results possible with a limited budget, translated in low-end measuring equipment and reduced onboard computational capabilities.

For an unambiguous understanding of the terms "light" and "low-cost", we consider a system to be compliant with this adjectives if the total payload is smaller than $4\,\mathrm{kg}$, and the sensors and processing units cost under $\$250\,\mathrm{USD}$, altogether integrated into a portable solution. This is neither an exact nor strict value, but it provides a rough idea of the order of magnitude of the budget for the considered application. As such, it is considerably lower than the values reported for high-end applications, in the order of tens of thousands of US dollars [Stempfhuber-11; Manfreda-18].

In this research we focus on applications where the navigation trajectory of a vehicle or pedestrian is required to be estimated, relying on low-cost sensors. We propose the implementation of a discrete Kalman filter to improve the user trajectory estimates provided by the employed GPS receiver. As a further enhancement to user position estimation, we present a method to incorporate landmarks in aerial images into the proposed estimation scheme.

In addition to the pedestrian applications of satellite navigation relying on low-cost receivers, navigation of aerial vehicles is thoroughly explored, specifically related to the delivery of payload by analyzing the controlled descent of parachutes.

1.2. Parachues

Introduced and patented by Jalbert [Jalbert-66], ram-air parachutes have been studied and optimized for a wide range of applications, from the military for emergency ejection escapes, delivery of troops and munitions; civil applications as the delivery of supplies and towed cargo; the aerospace industry for the controlled reentry, recovery and reuse of spacecraft; to other recreational activities as sport jumping.

Ram-air parachutes are constructed from not porous fabric, which allows a compact storage, without any rigid member. When released, they inflate as regular parachutes, but in contrast, these types of parachutes resemble a low aspect ratio wing, once fully deployed. Their construction is based on an upper and a lower membrane connected by spanwise distributed ribs, forming individual cells. As the parafoil expands, air flows through an opening on the leading edge, spreading along the entire wing as the cells have apertures to ensure full inflation, and exits on the trailing edge. It is this airflow that provides rigidity to the structure to perform efficiently as a wing. Finally, suspension lines attached to the ribs are connected to the control unit, if existent, or directly to the payload [Lingard-86]. Different accessories are commonly used, as lateral stabilizer panels and flaps to control the airflow, increasing the controllability of the parachute.

In comparison, traditional round parachutes descend primarily in the vertical direction. Their construction consists of a circular parafoil with radial symmetry and cuts at the top, allowing the air to flow through the inflated canopy and to gain a minimum gliding capability. These cuts, also called vents, provide some stability to the rather unstable structure, otherwise commonly suffering from pendulum oscillations [Lingard-95].

The lift to drag ratio (L/D) represents the aerodynamic efficiency of the parafoil, which directly relates the horizontal and vertical traveled distance. Typical L/D ratios for circular parachutes range from 0.8 to 1.5, whereas ram-air parachute used on PADSs range from a minimum of 2.5 up to 4 for typical applications, reaching up to 6, according to Yakimenko [Yakimenko-16]. The notation X:1 is commonly used to express the glide ratio, equal to the lift to drag ratio, meaning that X horizontal meters can be obtained per unit of height loss, or vertical displacement.

A full description on the overall aerodynamic characteristics of ram-air parachutes, including aspect ratio, lift and drag coefficients, drag contributions per component, lateral and longitudinal

dynamics, as well as flight performance under deflections and maneuvers, is presented by Lingard [Lingard-95].

1.3. Weather Balloons

A sounding balloon is a probe mainly composed of three parts: a filled balloon as an up-thrust source, a parachute, and a payload. The buoyancy force that drives the probe upwards is obtained from filling the balloon with a gas lighter than air, typically helium or hydrogen, reaching altitudes up to $30\,\mathrm{km}$.

According to Knacke [Knacke-91] and Yakimenko [Yakimenko-16], circular parachutes are used mostly to decelerate uncontrolled payloads on their trajectory back to the surface of the Earth. In contrast, controlled descents make use of ram-air parafoils due to their capacity to cover considerably large horizontal distances with respect to a vertical descent, together with their steering capabilities.

A weather balloon is a type of sounding balloon used to acquire atmospheric parameters during its trajectory, collecting information regarding the vertical profile of the lower troposphere, such as temperature, humidity, pressure, wind speed, and wind direction. A typical weather balloon flight can last around 2 hours without being controlled, drifting more than $200\,\mathrm{km}$ from the release point. The information gathered by weather balloons represents the worldwide core input for air pollution models, meteorological forecasts, and the assessment of atmospheric conditions during meteorological events. When a weather balloon is equipped with a radio transmitter, is referred to as a radiosonde.

Nowadays, according to the Integrated Global Radiosonde Archive (IGRA) [NOAA-16], there are almost 1000 stations gathering upper-air information by means of synchronous sounding at 00:00 and 12:00 UTC, by international agreement, 365 days a year, representing around $500\,000$ launches per year. The National Weather Service (NWS) of the United States of America (USA), as part of the National Oceanic and Atmospheric Administration (NOAA), releases approximately $75\,000$ radiosondes each year [NOAA-18]. In Switzerland, through the Federal Office for Meteorology and Climatology, MeteoSwiss, approximately 730 radiosondes are released per year [MeteoSwiss-20].

According to Dabberdt and Turtiainen [Dabberdt-15], just a few countries actively seek to recover and reuse their radiosondes. For example, the USA reuses only between $10\,\%$ and $15\,\%$, whereas

Switzerland, reuses more than $60\,\%$ of their yearly releases. A common way to recover probes is by adding a prepaid envelope to the radiosonde, so that when it is found it can be shipped back by the person who finds it [NOAA-18]. If a weather balloon is not equipped with a transmitter, it must be recovered in order to obtain the collected data, otherwise, the information would be lost. Due to the elevated cost of the equipment that comprises a ground station, some sounding balloons do not broadcast the collected data during flight. The cost of the required gear and antennas of a ground station can go from thousands to the hundreds of thousands of US dollars. Even if a weather balloon is equipped with a transmitter, the decision to seek the payload after the flight is mostly based on the economic factor, since a recovery expedition can be costly in comparison with the radiosonde cost, especially when the landing zone is in an inhospitable area.

A significant risk is taken when using weather balloons since there is no type of control over the probe during its ascent. As the probe ascents, the balloon continuously expands due to the decrease in atmospheric pressure, up to bursting. Typically, the onboard parachute starts deploying immediately after the bursting point, reaching full inflation still at a very high altitude. If the descent is not controlled, the trajectory of the probe is solely modified by the wind during the rest of its flight back to the surface of the Earth, resulting in significant drift distances from the intended point of impact. For this reason, aerial delivery systems have been developed, so that probes can be maneuvered towards desired landing-zones, useful for a wide range of applications. In the following, these delivery systems are analyzed, including a thorough description of their historical development, modeling, functioning and classification.

1.4. Precision Aerial Delivery System

The use of Unmanned Aerial Vehicles (UAVs) has spread to numerous disciplines and will continue to expand in the foreseeable future, as more affordable sensors, actuators, and processing units become available, together with the advances in their legislation around the globe. Nowadays, UAVs are used in several applications in the scientific, civil, and commercial fields; for instance, in precision agriculture, weather monitoring, search and rescue, mining, remote sensing, and delivery of goods [Shakhatreh-19; Park-20].

In this research, we focus on the use of UAVs for the delivery of payloads. A large number of

applications make use of UAVs to deliver food, merchandise, medical supplies, or rescue equipment, among others. When natural disasters occur, such as earthquakes, landslides, blizzards, wildfires, or floods, affecting the terrestrial infrastructure, UAVs can promptly deliver emergency supplies. Additionally, UAVs provide a solution in situations where the rugged topography of a region inhibits fast transportation. For example, the company Zipline is delivering daily blood and blood products to health centers in the regions around the countries of Rwanda and Ghana, in Africa [Ackerman-19]. Given the Coronavirus disease 2019 (COVID-19) pandemic, Zipline is also distributing medical supplies and personal protective equipment, and recently pursuing the possibility to provide COVID-19 supplies in the USA [Ackerman-20].

Several applications of UAVs rely on vehicles instrumented with expensive and delicate sensors. For instance, in remote sensing scenarios, it is common the use of Light Detection and Ranging (LiDAR); optical, multispectral, hyperspectral, and thermal cameras; radar; GNSS receivers; and processing units [Manfreda-18]. In the case of a vehicle malfunction, these instruments could be damaged given a collision with the ground, or lost in the event of loss of flight control or communication, causing landing in an unknown or unreachable location. In these situations, a safe-landing feature is most needed to recover the vehicle and its equipment. PADSs make use of guidance, navigation, and control, to maneuver parafoil-payload systems towards safe-landing zones, increasing the chances of successfully delivering payloads on target, and diminishing the possible damage while landing.

A typical descent flight of a PADS is illustrated in Fig. 1.1. The trajectory is composed of three segments: an initial flight towards the intended landing point (homing); a lemniscate (figure-eight) or circular pattern while losing altitude (energy management); and finally, a narrow turn to reach the target facing into the wind (landing). In this illustration three vehicles are depicted to represent different application scenarios, for example, a cargo aircraft for the delivery of goods, or as a recovery system for a weather balloon or a multicopter.

1.4.1 Flight Dynamics Modeling

Design, modeling, and characterization of PADSs have been taking place since the beginning of the 1970s. Static and dynamic longitudinal stability was first studied by Goodrick [Goodrick-75;

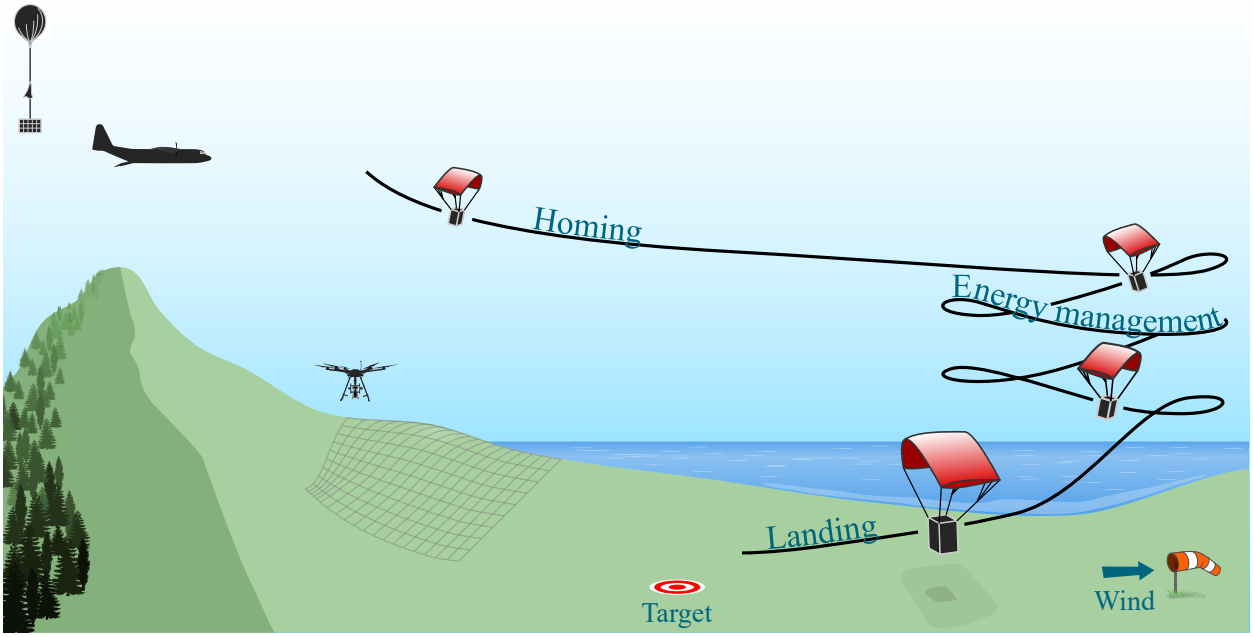

Fig. 1.1. Typical Precision Aerial Delivery System (PADS) flight profile.

Goodrick-79], together with the early development of the equations of motion governing parafoil-payload systems, considering 3- and 6-DOF, and the characterization of a $150\,\mathrm{kg}$ test payload. Simulations that first studied the parafoil-payload as a nonrigid system were introduced by Wolf [Wolf-71], who developed a 5-DOF system allowing for the relative motion between the parafoil and the payload, assembled by a joint, considering three-dimensional translation and bi-dimensional rotation, neglecting the roll angle.

At the beginning of the 2000s, the Small Autonomous Parafoil Landing Experiment (ALEX I and II), described in detail by Jann [Jann-01; Jann-05], set a milestone on modeling, validation, and verification of PADSs using 3- and 4-DOF, employing a ram-air parachute with a payload of $100\,\mathrm{kg}$.

In order to improve the understanding of the governing forces acting on PADSs, models that accounted for the relative motion between the parafoil and the payload became necessary, together with the corresponding validation between real flight data and computer simulations. Typically, sensors dedicated to obtaining information on the motion of the parafoil-payload system are mounted on the payload, or very near to it. While this provides sufficient information on the behavior of the payload itself, it does not add enough information on the flight dynamics of the parafoil, nor about their relative motion. For this reason, efforts arose to determine the behavior of the complete system using different techniques. For example, Strickert and Jann [Strickert-99] used video-image

processing techniques to estimate the relative motion (attitude only) between the parafoil and the payload based on the ALEX vehicle.

Different models have been developed for a varying range of DOF, either considering the parafoil-payload system as a rigid body or allowing relative motion between their components [Lingard-95; Mortaloni-03].

Comparisons between models happen to be a complex task, since different considerations, payload masses, parafoil aerodynamic properties, and general assumptions are used by different authors. To be able to compare the effectiveness between models ranging from 6- to 9-DOF, Gorman and Slegers [Slegers-11a; Gorman-12] developed a parafoil model using the same aerodynamic properties for each scenario, realizing different DOF by modifying the kinematics constraints between the parafoil and the payload, under the same control inputs and initial conditions. The 6-DOF model represents the three inertial position components of the joint connecting the parafoil and the payload, as well as three Euler orientation angles. The 7-, 8-, and 9-DOF models incorporate extra Euler orientation angles for the payload, depending on the connection constraints. The 7-DOF model allows for yaw relative motion, the 8-DOF model allows yaw and pitch, whereas the 9-DOF model allows yaw, pitch, and roll relative motion between the parafoil and the payload. By contrasting experimental data with the models, Gorman and Slegers were able to conclude that the 6-DOF trajectory differed from the 7-, 8-, and 9-DOF trajectories mainly because of the great yaw relative motion (parafoil-payload twist). Since the relative roll and pitch motion is negligible in comparison to the relative yaw motion, the 7-DOF represents the model with the minimum DOF that captures the most significant flight dynamics, while the 6-DOF successfully characterizes the parafoil-payload system as a rigid body, presenting lower complexity than the rest of the proposed models.

Since the PADS analyzed in this investigation is considered a rigid body, a 6-DOF model is adopted.

1.4.2 Classification

Due to the versatility of these delivery systems, and their possible applications in military scenarios, different sectors of the US Army teamed to form the Joint Precision Airdrop System

(JPADS), categorizing their systems by weight as micro-light ($4.5\,\mathrm{kg}$ to $68\,\mathrm{kg}$), ultra-light ($113\,\mathrm{kg}$ to $318\,\mathrm{kg}$), extra-light ($318\,\mathrm{kg}$ to $998\,\mathrm{kg}$), light ($2268\,\mathrm{kg}$ to $4536\,\mathrm{kg}$) and medium ($6804\,\mathrm{kg}$ to $19\,051\,\mathrm{kg}$) [Benney-07; Benney-09].

The lightest platforms developed are the Mosquito Tactical Resupply System, developed and commercialized by STARA Technologies; and Snowflake, developed by the University of Alabama and the Naval Postgraduate School [Yakimenko-09]. Both systems report a Circular Error Probability (CEP) of $30\,\mathrm{m}$. The Snowflake system by itself, considering only a ram-air parafoil, guidance, navigation and control unit, together with its packing, weights at minimum $2\,\mathrm{kg}$, being capable of carrying up to additional $2.2\,\mathrm{kg}$ as payload.

Initially, one of the JPADS requirements was to achieve $\$13.22\,\mathrm{USD}$ per kilogram of payload, a goal only met for the heavy categories, but far from being met for the light categories (micro-light, ultra-light, and extra-light) [Yakimenko-16]. Making more affordable systems has been a priority, even at the expense of reducing their delivery precision. Cost reduction can be achieved by employing cheaper parachutes. Ram-air parafoils are typically expensive, approximately 3 to 4 times more expensive than circular parachutes, and about 20 times more expensive than cruciform parachutes.

The Affordable Guided Airdrop System (AGAS), formed in 1999 [Brown-99], has the goal to minimize as much as possible the cost of delivery systems, obtaining the best achievable accuracy within a threshold of $100\,\mathrm{m}$ CEP. The AGAS initiative has been focusing on the extra-light and lightweight ranges, where mainly $900\,\mathrm{kg}$ payload implementations have been tested using circular parachutes, achieving $211\,\mathrm{m}$ CEP when 12 hours-old wind forecast information was used, and $38\,\mathrm{m}$ CEP when near real-time wind profiles were used [Jorgensen-05]. Lighter systems have been able to achieve up to $10\,\mathrm{m}$ in specific cases [Yakimenko-16]. Reduction in the actual landing distance to the intended point of impact, which translates to small CEP, has been achieved by the development of optimal control and guidance [Kaminer-03; Slegers-09], strongly dependent on high-quality information about the wind profiles during the entire flight, from the beginning of the descent up to touchdown, and the capability to account for variable winds [Cacan-15]. Nevertheless, achieving such high precision comes with a price, requiring computational power and elevated costs on sensors, actuators, and parachutes.

Although the $5\,\mathrm{kg}$ to $19\,000\,\mathrm{kg}$ weight-range has been widely analyzed and tested, delivery

systems for lighter applications have not been thoroughly explored, especially for low-cost solutions. Lightweight applications of PADSs face the challenge of relying on light hardware to perform guidance, navigation, and control. Current parafoil-payload systems make use of high-end processing units, capable of handling sophisticated real-time implementations of highly nonlinear dynamical models to estimate their attitude and position to operate their guidance system. If low-cost miniaturized versions of these delivery systems are to be explored, simplified models that capture their flight dynamics need to be developed. Additionally, estimation schemes for their position and attitude need to be taken into account, especially for further guidance and control implementations on vehicles with limited sensors, actuators, and processing capabilities.

2. Kalman Filter

This chapter presents the formulation of a model-based Kalman filter using a total state-space formulation [Simon-06].

Given a linear discrete-time system with state vector $\mathbf{x}$ and a measurement vector $\mathbf{z}$:

$$\mathbf{x}_k = F_{k-1}\mathbf{x}_{k-1} + G_{k-1}\mathbf{u}_{k-1} + w_{k-1} \tag{2.1}$$

$$\mathbf{z}_k = H\mathbf{x}_k + v_k \tag{2.2}$$

the Kalman filter provides the best estimate of the states $\widehat{\mathbf{x}}$, as a linear combination of the measurements. F represent the state transition matrix, G the control matrix, and H the observation matrix. The observation matrix H communicates the availability of the measurements, relating them with the state vector. The process noise w and measurement noise v, are both assumed to be white, uncorrelated, and zero-mean.

The estimate of the states is denoted as an *a posteriori* estimate $\widehat{\mathbf{x}}_k$, if information from the measurements is available up to, and including, epoch k. If all the measurements are available before epoch k, therefore excluding epoch k, the estimate is denoted as an *a priori* estimate $\widehat{\mathbf{x}}_k^-$. Similarly, the a posteriori covariance of the estimation error is represented as P_k, and the a priori error covariance as P_k^-.

The initialization of the covariance of the state estimation error ($P_{k=0}$), depends on how well the initial state estimate ($\mathbf{x}_{k=0}$) is known. The bigger the uncertainty of the initial state, the larger the initial covariance. In the case the initial state is precisely known, the covariance is initialized close to zero. In the case there is no information about the initial state, the covariance is initialized with close to infinity.

The estimation process is initialized by propagating the a posteriori estimate and covariance, from epoch $k-1$ to k, in the so-called time-update equations:

$$\widehat{\mathbf{x}}_k^- = F_{k-1}\widehat{\mathbf{x}}_{k-1} + G_{k-1}\mathbf{u}_{k-1} \tag{2.3}$$

$$P_k^- = F_{k-1} P_{k-1} F_{k-1}^T + Q_{k-1} \tag{2.4}$$

where Q represent the process noise covariance matrix. Notice that to update the estimation of the states, only the dynamics of the system is required. This represents the estimate of the state at epoch k, but before the measurement $\mathbf{z}_k$ is available.[1]

Next, the a posteriori state estimate $\widehat{\mathbf{x}}_k$ is computed as a linear combination of the a priori estimate $\widehat{\mathbf{x}}_k^-$, and the difference between the measurement vector $\mathbf{z}_k$ and the prediction $H_k\widehat{\mathbf{x}}_k^-$, weighted by the Kalman gain K_k, designed to minimize the a posteriori error covariance P_k, as part of the so-called measurement-update equations:

$$K_k = P_k^- H_k^T \left(H_k P_k^- H_k^T + R_k\right)^{-1} \tag{2.5}$$

$$\widehat{\mathbf{x}}_k = \widehat{\mathbf{x}}_k^- + K_k \left(\mathbf{z}_k - H_k\widehat{\mathbf{x}}_k^-\right) \tag{2.6}$$

$$P_k = \left(I - K_k H_k\right) P_k^- \left(I - K_k H_k\right)^T + K_k R_k K_k^T \tag{2.7}$$

$$= \left(I - K_k H_k\right) P_k^- \tag{2.8}$$

where R represents the measurement noise covariance matrix, and I corresponds to the identity matrix. The information of the measurements is incorporated into the estimation process in (2.6) in the denominated *innovations*, defined as $\left(\mathbf{z}_k - H_k\widehat{\mathbf{x}}_k^-\right)$.

Two alternatives for calculating the a posteriori covariance are presented. The first expression (2.7) is known as the Joseph stabilized version, which is a more robust formulation, less susceptible to numerical instabilities, for example, in a computational algorithm prone to round off errors. The stability and robustness of the Joseph version is gained at the cost of more computational workload [Crassidis-11].

The performance of the filter can be evaluated by investigating the statistics of the innovations. Specifically, it can be verified that the innovations represent a white noise process, with zero mean. Additionally, the estimation accuracy is indicated by the covariance P_k.

[1] Note that (2.3) has the same form as the state vector derived in (5.176) for the linearized model, as well as in (5.180) for the double integrator model, developed in future chapters.

3. Performance of Low-Cost GPS Receiver for Pedestrian Navigation

The diverse and rapidly growing number of low-cost systems dedicated to the surveying of land, oceans and agricultural ecosystems, require affordable sensors and processing units. Typical applications of these systems rely on the estimation of their trajectories while sensing, where conventionally low-cost Global Positioning System (GPS) receivers are used. Consequently, there is a direct relation between the accuracy of the position determination of the system and the quality of the generated surveying products.

This chapter focuses on the accuracy estimation of a low-cost GPS receiver based only on position measurements, and landmarks in aerial images. For comparison purposes, and to validate the performance evaluation, the positioning results are compared with respect to a commercial receiver and coordinates obtained using Differential GPS (DGPS).

Furthermore, we propose a methodology for the estimation of the navigation trajectory, based exclusively on one onboard low-cost GPS receiver combined with aerial images, employing a discrete Kalman filter. A total state-space formulation of the filter is implemented over a reference path to assess its performance. Additionally, error state-space corrections are applied to the filter based on landmarks in aerial images.

3.1. Accuracy Estimation

Tackling the problem of obtaining the position estimation accuracy of a low-cost GPS receiver is a necessary task, in order to evaluate its possible applications. While accuracy evaluations of low-cost GPS receivers have been carried out in previous studies [Matosevic-06; Reisdorf-16; Rodríguez-Pérez-07], most assessments are based on elaborated statistical analyses, depend on having access to code and carrier phase measurements, or ultimately make use of the DGPS technique. In contrast with professional (and costly) receivers, most low-cost GPS receivers do not allow for direct access to the raw satellite measurements, making the analysis based on processing the navigation message

impossible to perform.

The complexity in estimating the positioning accuracy of any Global Navigation Satellite System (GNSS) receiver, relies on the lack of knowledge about the true position of the user at all times during navigation. In order to have access to the true position of the user, alternatives have been proposed based on surveying techniques using in situ measurements [Abdi-12], which are highly time-consuming and require specialized equipment.

The research here presented aims to evaluate the accuracy of a low-cost GPS receiver by comparing its position estimates with respect to a known trajectory of the user, based on aerial images (visible spectrum only). A methodology is developed that allows a direct comparison between the estimated position of the GPS receiver and the true path traveled by the user, by correlating the followed trajectory with landmarks on the image. In order to comparatively evaluate the performance of the low-cost GPS receiver, a commercial GNSS receiver is included in the analysis. Professional equipment that uses DGPS is employed to obtain a pair of highly precise positioning solutions for comparison purposes.

The low-cost GPS receiver under analysis is an u-blox NEO-6M equipped with a $25 \times 25\,\mathrm{mm}$ patch antenna. The commercial GNSS receiver (GPS and GLONASS capable) is a handheld Garmin eTrex 10. Finally, the georeferenced coordinates are obtained by a professional Trimble DGPS receiver. While the exact model of the Trimble receiver is not available, its generated topographic survey is used as reference, reporting a subcentimeter accuracy.

3.1.1 Trajectory Definition

A pedestrian trajectory was followed on a predefined route at ITESO University campus, taking care of selecting a route that can be precisely identified on a high-resolution aerial image. The path was chosen to mostly cover open outdoors routes where visible landmarks could be identified, such as painted sidewalks, jogging track lanes, and recognizable patterns in the concrete.

Although several routes were tested including different types of areas, for example, proximity to buildings that could increase the impact of multipath and a combination of outdoor and indoor walking, only one final route is presented in this work for clarity, designated as the reference path.

The carrier of the receivers, hereinafter denoted as the user, walked through the reference path

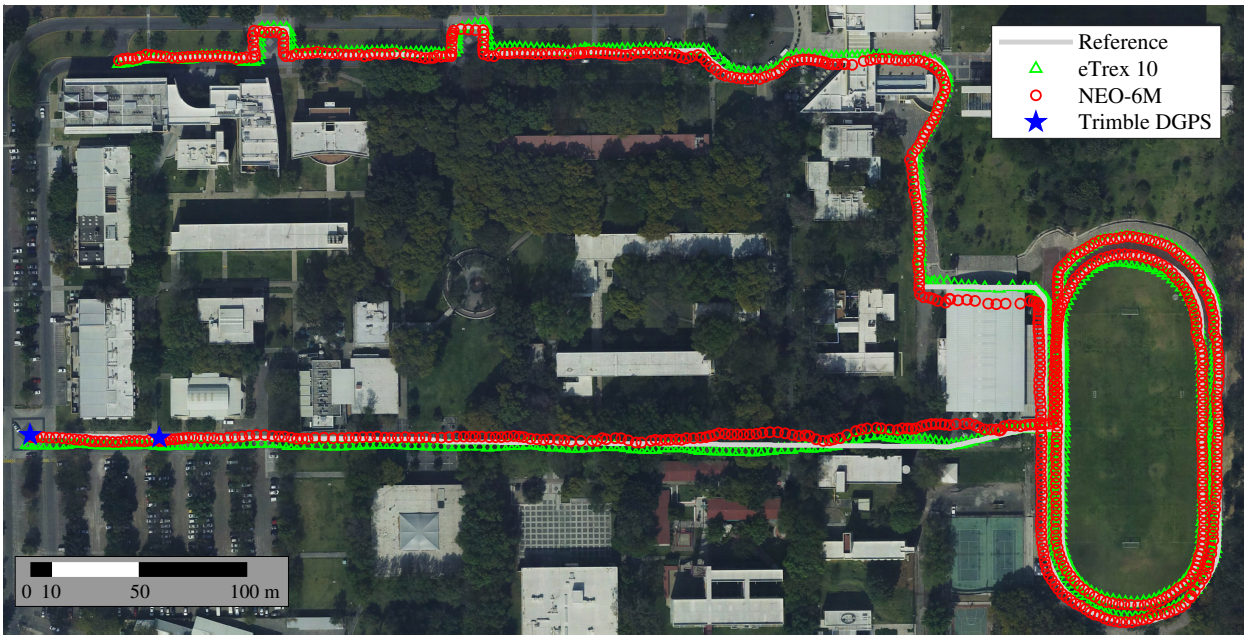

Fig. 3.1. Trajectory under analysis. Position estimates of the low-cost (NEO-6M), commercial (eTrex 10), and professional (Trimble DGPS) receivers are shown over the followed reference path.

holding both receivers, the low-cost u-blox NEO-6M, and the commercial Garmin eTrex 10 receiver, ensuring less than $1\,\mathrm{m}$ of distance between them at all times. Both were set to track the reference path with a $1\,\mathrm{Hz}$ sampling rate. The position estimates are considered as provided by default, i.e., with no manipulation on the solution algorithm used by the receivers.

The resulting estimated positions of the low-cost GPS receiver (NEO-6M), the commercial GNSS receiver (eTrex 10), the followed reference path, as well as the available DGPS coordinates (Trimble DGPS) are presented in Fig. 3.1. The position estimates are overlaid on an orthorectified aerial image, which has a ground sampling distance of $15\,\mathrm{cm}$.

The complete travelled distance was of $1989.0\,\mathrm{m}$, from beginning (top-left) to end (bottom-left) in $25.2\,\mathrm{min}$, representing 1509 samples. Considering a resulting slow pedestrian average motion of around $4.75\,\mathrm{km/h}$, the samples of the receivers tracked along the reference path are assumed to be taken at the exact same epoch.

The accuracy evaluation is based on the direct comparison between the position estimation of the receiver at a given sampled epoch and the true position of the user at that moment. To do so, a synchronization between the location of the user over the reference path and the receiver sample needs to be achieved. In other words, even when the trajectory of the user is perfectly known, its

location at a specific moment (epoch) is not known. This missing information is to be obtained so that the true location of the user at a given epoch can be paired with the correspondent epoch of the receiver.

As an option to achieve such type of synchronization, an additional reference could be incorporated into the system, for example, time stamps recorded along the reference path. Nevertheless, this implies an increment in the complexity for the accuracy estimation methodology, since an additional clock is to be considered.

Since the objective of this research is to develop a methodology that allows for a direct accuracy estimation process, without depending on accurate (and typically expensive) clocks, and increased complexity, an alternative is introduced. In the following, a method based on recognizable features in the aerial image and the reference path is developed in order to perform the discussed synchronization.

3.1.2 Trajectory Synchronization

The shape of the reference path is used to perform the synchronization between the true location of the user and the corresponding epoch of the receiver. The accuracy of the methodology presented in this work relies on the precision and accuracy to which the reference path is known. Therefore, only parts of the trajectory that can be identified to a submeter level in the aerial image are considered for the accuracy estimation process of the receivers. Consequently, parts with occlusions due to the canopy of the trees, or uncertainty on the traveled path where no recognizable landmarks were available, are discarded.

After inspecting the reference path over the orthophoto, $75.5\,\%$ of the traveled trajectory is estimated to be known at the level of decimeters (1139 out of the 1509 data points available), and only these validated data points are to be considered for the analysis. Invalid data points are omitted in all the following calculations and figures. This shows the relevance in the selection of a reference path rich in recognizable landmarks in the orthophoto.

The reference path has been selected so that the user has to walk over landmarks, as well as having both abrupt and smooth changes in the direction of motion. Since the walking direction of the user is known in correspondence with the reference path, the change in its direction is also known and computable. By identifying the change in direction of the user in accordance to the changes in

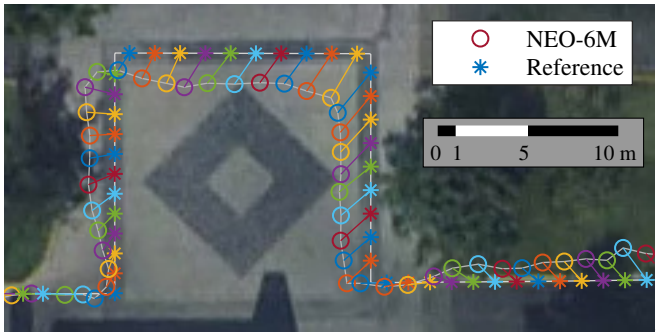

Fig. 3.2. Synchronization of the low-cost GPS receiver with respect to the reference path, based on the change in direction of the user and recognizable landmarks in the orthophoto (only a close-up section of the image is shown for clarity).

the reference path, it is possible to synchronize the location of the user along the reference path, and finally, interpolate the results between recognizable changes of direction or landmarks over the path.

Initially, the estimated latitude and longitude coordinates from the receivers are forward projected to the aerial image using as reference the World Geodetic System 1984 (WGS84). Throughout the reference path there is only an altitude variation of approximately $\pm 5\,\mathrm{m}$, and therefore the area under study is considered to be flat. For all further comparison purposes, only the resulting x and y map coordinates, measured in units of length (m), will be analyzed in order to obtain a horizontal accuracy estimation, discarding the altitude parameter.

The result of the synchronization is shown in Fig. 3.2. It can be clearly observed how features of the referenced path are translated to the receiver estimated trajectory by virtue of the synchronization process. For example, it can be seen how the corresponding locations at the corners have been paired, even when the curvy trajectory of the receiver differs from the reference path with sharp edges. For a better understanding, a line has been explicitly drawn connecting the corresponding epoch on the reference path and on the estimated position of the low-cost GPS receiver.

The accuracy of the low-cost GPS receiver is computed by calculating the Euclidean distance between the position of the user on the reference path and the corresponding receiver position estimation, as:

$$d_{ru} = \sqrt{(p_r - p_u)\,(p_r - p_u)^T} \tag{3.1}$$

where p_u represents the row vector $(x, y)_u$ of map coordinates of the low-cost GPS receiver at a given epoch, and p_r represents the corresponding synchronized row vector $(x, y)_r$ of map coordinates over

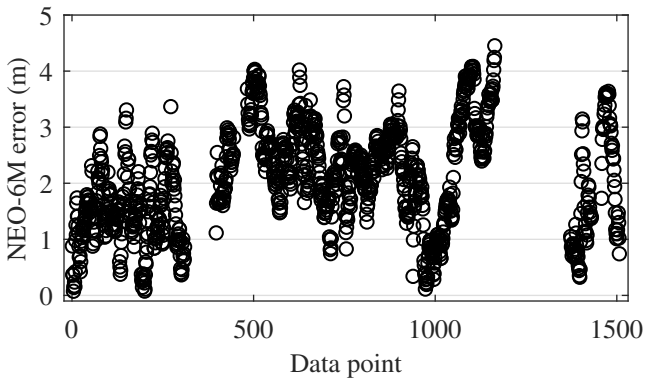

Fig. 3.3. Error of the low-cost GPS receiver with respect to the reference path. Synchronization based on the change in direction of the user and image landmarks.

the reference path. The distance d_{ru} corresponds to the line segment connecting each data point as shown in Fig. 3.2.

Fig. 3.3 shows the error (distance) between the low-cost GPS receiver and the reference path for all valid data points. The accuracy was found to be at a meter level, with a mean value of $2.08\,\mathrm{m}$ and a standard deviation of $0.91\,\mathrm{m}$.

3.1.3 Comparison Without Synchronization

In order to have a better understanding regarding the accuracy of the low-cost GPS receiver, its position estimates are compared to those position estimates provided by a commercial and a professional GNSS receiver.

The methodology implemented in Section 3.1.2 proved to be effective, nevertheless, it requires a reference path with sufficient and distinguishable changes in the direction of the user while traveling, in order to perform the presented synchronization. In the case that the desired reference path cannot comply with these conditions, for example, due to the lack of recognizable landmarks in the image, or pedestrian accessibility (forcing the user to follow a different route), synchronization as previously introduced cannot be accomplished.

An alternative, is to perform the accuracy estimation by calculating, epoch-wise, the minimum Euclidean distance between all points in the reference path, and the position estimates of the receiver. In contrast with the previously demonstrated method, this procedures calculates the distance between each data point of the receiver and the closest data point in the reference path, and not with respect

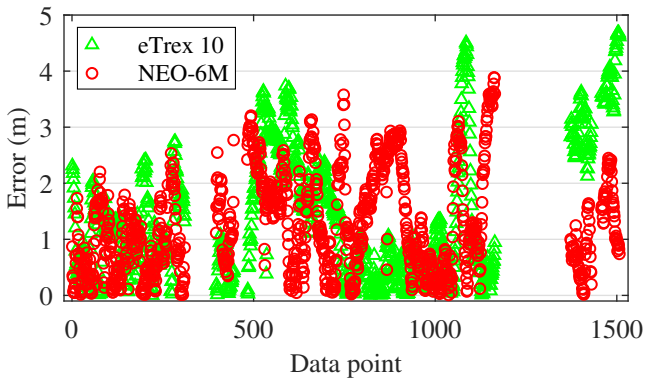

Fig. 3.4. Error considering the minimum distance between the reference path and the estimated position of the low-cost NEO-6M receiver and the commercial eTrex 10 receiver (no synchronization required).

to the location where the user should have been when the position was estimated by the receiver.

The accuracy of the low-cost and the commercial receivers, calculated as the minimum distance with respect to the reference path, is presented in Fig. 3.4. The accuracy of the low-cost NEO-6M receiver was found to be at the meter level, with a mean error value of $1.28\,\mathrm{m}$ and a standard deviation of $0.90\,\mathrm{m}$, while the solutions from the commercial eTrex 10 receiver exhibit a mean error value of $1.39\,\mathrm{m}$, and a standard deviation of $1.16\,\mathrm{m}$.

It is important to keep in mind that the accuracy obtained by this method will always be too optimistic, since it is based on a minimum distance calculation between the position estimation of a receiver and the reference path, regardless of the true position of the user along the trajectory. On the other hand, this method has the advantage of being simpler in terms of its implementation, independent of the shape of the reference path, and still provides a reasonable order of magnitude of the accuracy of the receivers. The difference in the mean error values between the two shown methods (synchronized vs. unsynchronized trajectories) amounts to only $0.8\,\mathrm{m}$ for the NEO-6M GPS receiver.

Finally, the pair of georeferenced coordinates obtained by a professional Trimble DGPS receiver is compared with the position estimates of the other two receivers. The reference path was designed to cross over these coordinates, so that the accuracy in stepping over them can be assessed.

According to the topographic survey of the Trimble DGPS receiver, the landmarks (five-pointed stars in Fig. 3.1) correspond to the Universal Transverse Mercator (UTM) coordinates $13\,\mathrm{N}$ ($105\,\mathrm{W}$) $664\,871.906\,\mathrm{m}$ E, $2\,279\,421.928\,\mathrm{m}$ N (left star), and $664\,931.437\,\mathrm{m}$ E, $2\,279\,420.771\,\mathrm{m}$ N (right

star), respectively.

Following the same minimum distance criterion, the NEO-6M receiver missed by $1.02\,\mathrm{m}$ the right star, and by $1.03\,\mathrm{m}$ the left star. In the same manner, the eTrex 10 receiver missed by $3.65\,\mathrm{m}$ the right star and by $3.72\,\mathrm{m}$ the left star. These results suggest that the low-cost NEO-6M receiver is slightly more accurate than the commercial eTrex 10 receiver for the application intended in this experiment, both in comparison to the reference path and to the Trimble DGPS coordinates.

3.2. Pedestrian Trajectory Estimation

The objective is to estimate as close as possible a navigation trajectory, given discrete position estimates of a low-cost GPS receiver contaminated by measurement errors, under the hypothesis that additional information is known about the followed trajectory. For most of the cases in any navigation scenario, there is knowledge of the expected behavior. For example, it can be known with a specific uncertainty that a vehicle is traveling in a straight line at constant velocity, or that the vehicle navigated over a recognizable landmark as a sidewalk, an intersection, a light pole, etc. This information, along with its determination errors or uncertainties, can be incorporated into an estimation scheme to improve the resulting trajectory.

To achieve this, two steps are followed. Firstly, a discrete Kalman filter is designed in a total state-space formulation, based on assumed dynamics of the vehicle, to get a first estimate of the trajectory. Secondly, information regarding identifiable landmarks in an aerial image is incorporated into the Kalman filter as measurements with known covariance, in an error state-space formulation. Our proposal prioritizes simplicity so that it can be used in low-cost applications. Consequently, the motion of the vehicle is approximated by a linear model.

A kinematic model of the user is assumed with constant acceleration, due to the slow pedestrian dynamics

$$\vec{x}_k = \vec{x}_{k-1} + \dot{\vec{x}}_{k-1}\delta t + \ddot{\vec{x}}_{k-1}\delta t^2/2 \tag{3.2}$$

where the vector state $\vec{x}$ at epoch k represents the user position, as a consequence of being subjected to a constant acceleration for δt seconds (from $k-1$ to k).

Since only position measurements are available, the velocity and acceleration of the user are

estimated as the change in position and velocity of previous epochs respectively as

$$\dot{\vec{x}}_k = \dot{\vec{x}}_{k-1} + \ddot{\vec{x}}_{k-1}\delta t \tag{3.3}$$

$$\ddot{\vec{x}}_{k-1} = (\dot{\vec{x}}_{k-1} - \dot{\vec{x}}_{k-2})/\delta t_{k-1} \tag{3.4}$$

where δt_{k-1} represents the elapsed time from epoch $k-2$ to $k-1$.

3.2.1 Kalman Filter Model

Following a total state-space Kalman filter formulation as described in Chapter 2, the motion of the user as modeled in (3.2) and (3.3) can be rewritten as

$$x_k = [x\, y\, z\, \dot{x}\, \dot{y}\, \dot{z}]_k^T \tag{3.5}$$

$$F = \begin{bmatrix} 1 & 0 & 0 & \delta t + \frac{\delta t^2}{2\delta t_{k-1}} & 0 & 0 \\ 0 & 1 & 0 & 0 & \delta t + \frac{\delta t^2}{2\delta t_{k-1}} & 0 \\ 0 & 0 & 1 & 0 & 0 & \delta t + \frac{\delta t^2}{2\delta t_{k-1}} \\ 0 & 0 & 0 & 1 + \frac{\delta t}{\delta t_{k-1}} & 0 & 0 \\ 0 & 0 & 0 & 0 & 1 + \frac{\delta t}{\delta t_{k-1}} & 0 \\ 0 & 0 & 0 & 0 & 0 & 1 + \frac{\delta t}{\delta t_{k-1}} \end{bmatrix} \tag{3.6}$$

$$G = \begin{bmatrix} -\frac{\delta t^2}{2\delta_{k-1}} & 0 & 0 \\ 0 & -\frac{\delta t^2}{2\delta_{k-1}} & 0 \\ 0 & 0 & -\frac{\delta t^2}{2\delta_{k-1}} \\ -\frac{\delta t}{\delta t_{k-1}} & 0 & 0 \\ 0 & -\frac{\delta t}{\delta t_{k-1}} & 0 \\ 0 & 0 & -\frac{\delta t}{\delta t_{k-1}} \end{bmatrix} \tag{3.7}$$

$$u_k = \hat{\dot{x}}_{k-2} = [\dot{x}\, \dot{y}\, \dot{z}]_{k-2}^T. \tag{3.8}$$

While there is no control input interpreted as an actuator, there is a constant acceleration assumption that modifies the states, interpreted as the change in velocity between the second-last $(k-2)$ and the last $(k-1)$ epoch. The observation matrix H provides the relation between the state

vector and the measurements, reflecting the fact that only position measurements are available

$$H = \begin{bmatrix} 1 & 0 & 0 & 0 & 0 & 0 \\ 0 & 1 & 0 & 0 & 0 & 0 \\ 0 & 0 & 1 & 0 & 0 & 0 \end{bmatrix}. \tag{3.9}$$

The process noise covariance matrix is determined using the autocorrelation function $Q = G\sigma^2 G^T$ with variance $\sigma^2 = [10\,10\,5\,4\,4\,2]^T$ given in m^2 and $\mathrm{m}^2/\mathrm{s}^2$ respectively, obtained by tuning. The measurement noise covariance matrix R_z is determined using as reference the accuracy of the low-cost GPS receiver according to Section 3.1.2.

$$R_{z_k} = \begin{bmatrix} 1.8^2 & 0 & 0 \\ 0 & 1.8^2 & 0 \\ 0 & 0 & 3.6^2 \end{bmatrix} \quad (\mathrm{m}^2). \tag{3.10}$$

Since the sampling rate of the GPS receiver is set to be constant ($1\,\mathrm{Hz}$), matrices F, G, and Q will remain constant and can be computed beforehand, reducing significantly the operations to be performed. In the following, additional knowledge on the trajectory is incorporated into the Kalman filter to enhance the estimation process.

3.2.2 Landmarks for Estimates Improvement

Additional information of the trajectory followed by the user can be incorporated into the estimation process by modifying the previously developed Kalman filter, correcting the estimates with an error state-space formulation.

This information can be a known location where we have high confidence that the user passed by while walking. For example, we know that the user stepped over a recognizable landmark with a horizontal uncertainty of $0.6^2\ \mathrm{m}^2$, and that the user followed a straight line while walking over a certain part of the reference path. Knowledge on the behavior of the user while acquiring measurements from the GPS receiver, can be incorporated to the Kalman filter. This can be achieved by locating these landmarks in an aerial image and then correcting the position estimate.

The error state-space formulation of the Kalman filter modifies the a-posteriori state estimate $\hat{x}_k$

with the weighted difference between the measurement and the prediction.

$$\delta\hat{x}_k = K_k\left(y_k - H\hat{x}_k^-\right) \tag{3.11}$$

$$\hat{x}_k = \hat{x}_k^- + \delta\hat{x}_k. \tag{3.12}$$

The measurement y_k corresponds to the position of the landmark that is known with high confidence, therefore, the measurement covariance matrix R_y must be defined accordingly for each landmark. For example

$$R_{y_k} = \begin{bmatrix} 0.6^2 & 0 & 0 \\ 0 & 0.6^2 & 0 \\ 0 & 0 & 3^2 \end{bmatrix} \quad (\mathrm{m}^2). \tag{3.13}$$

The complete algorithm, including the total and error state-space formulations, is executed as follows:

1. Time update: The current state is estimated based on the motion model and the previous best estimate (2.3), and the error covariance is propagated (2.4), by substituting (3.6)–(3.8).

2. GPS measurement update: Once a GPS measurement $\mathbf{z}$ is received, the Kalman gain (2.5) is computed using the measurement covariance R_z (3.10). The a-posteriori state (2.6) and error covariance (2.8) are determined.

3. Correction: When the user is closest to a landmark, the position of the landmark is used as a measurement y. This measurement, together with its covariance R_y (3.13), is used to calculate the Kalman gain (2.5) and the correction $\delta\hat{x}_k$ (3.11). Finally, the improved estimate of $\hat{x}_k$ (3.12) is computed.

3.2.3 Analysis of Results

The proposed total and error state-space formulations were implemented using real measurements according to the trajectories described in Section 3.1.1 (Fig. 3.1), following the execution steps described at the end of Section 3.2.2. The results are presented in Fig. 3.5, where it can be observed how once the user is closest to a landmark, information with higher confidence is incorporated into

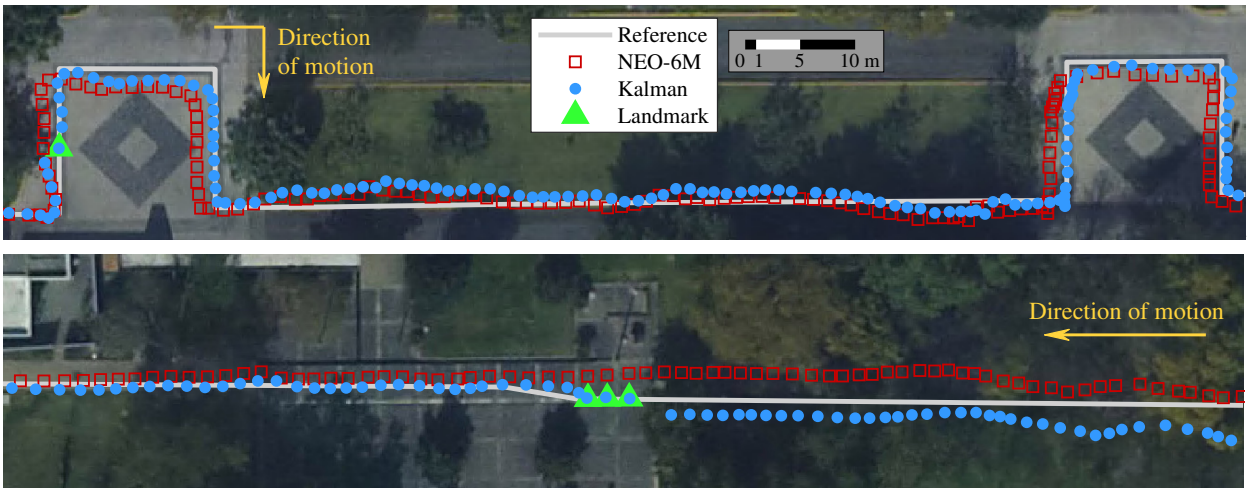

Fig. 3.5. Estimated navigation trajectory. The reference path, NEO-6M GPS measurements, Kalman filter estimates, and landmarks are presented for selected segments of the total trajectory followed by the user. It can be observed how once the user is closest to a landmark, the estimation process is improved by the correction determined by the error state-space formulation, bringing closer the estimated trajectory to the reference path. Plotted data points: top segment 50–184, bottom segment 1327–1398.

the estimation, bringing closer the estimated trajectory to the reference path due to the correction obtained by the error state-space formulation.

The error between the NEO-6M receiver and the reference path, together with the error between the Kalman filter estimates and the reference path, is presented in Fig. 3.6. This error is calculated as the minimum Euclidean distance between the GPS measurements or Kalman filter estimates and the reference path respectively. The NEO-6M receiver presented a mean error of $1.3\,\mathrm{m}$ and a standard deviation of $0.9\,\mathrm{m}$ on its position estimates with respect to the reference path. On the other hand, the estimates of the Kalman filter showed a mean error of $0.8\,\mathrm{m}$ with a standard deviation of $0.6\,\mathrm{m}$.

The reference path consists of $2\,\mathrm{km}$ of a pedestrian trajectory, in which 1509 measurement samples (data points) of the NEO-6M receiver were obtained. Even when the trajectory was chosen so that it could be identifiable in an orthophoto, small segments were not recognizable in the image due to the canopy of the trees or short passages under buildings. Those untraceable segments represent approximately $25\,\%$ of the total trajectory and were disregarded from this study, leading to the small data gaps presented in Fig. 3.6.

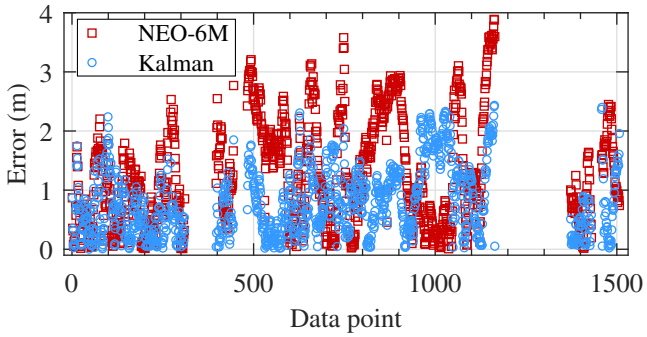

Fig. 3.6. Estimation error between the reference path and the measurements of the NEO-6M receiver, and the Kalman filter estimates respectively.

3.3. Conclusion

The accuracy of a low-cost GPS receiver was evaluated following a methodology based only on the receiver position estimates and aerial images. By defining a reference path with recognizable landmarks on the aerial images, and changes in the direction of motion of the user, the accuracy of an u-blox NEO-6M GPS receiver was found to be at the $1\,\mathrm{m}$ level, with respect to the true position of the user, as well as in the meter level in comparison to a commercial eTrex 10 receiver, and relative to coordinates obtained by a professional Trimble DGPS receiver. The proposed methodology was proved to be effective, and simpler than other procedures exposed in related works, however, requires very precise navigation of the user over a carefully selected reference path in order to ensure a submeter accuracy as true position, as well as the availability of high-resolution aerial images.

A linear motion model for pedestrian systems is proposed together with a total state-space formulation of a discrete Kalman filter, to estimate the navigation trajectory of users tracking their position with a low-cost GPS receiver. Additional information regarding identifiable landmarks in an aerial image, incorporated into the Kalman filter as measurements with low uncertainty in an error state-space formulation, proved to be an effective way of enhancing the trajectory estimation process for low-cost applications.

The applicability of this methodology on vehicles with different dynamics needs to be further investigated. While this method has demonstrated to be effective, it does require the availability of aerial images and well-known landmarks. This makes it difficult to be applied in unsupervised scenarios, where no additional navigation information is available to enhance the estimation process.

The tests using real data of the proposed methodology suggest the possibility of bias mitigation,

by correlating high confidence information based on the aerial image.

4. Estimation Scheme

The state estimation process based on the fusion of dynamic models and measurements obtained from different sensors is commonly and efficiently performed through a model-based Kalman filter. Whether a total state-space formulation of a Kalman filter is used; an error state-space, either with a feedforward or feedback implementation; an extended Kalman filter; an unscented Kalman filter; or any of modern developed variants, the Kalman filter is one of the most used algorithms for sensor fusion, particularly in navigation applications [Sabatini-11; Quinchia-13; Yang-20; Farhangian-20]. The type of Kalman filter implementation strongly depends on the intended application, the dynamics of the process to estimate, the required accuracy, and the computational capabilities at disposal.

According to a study performed by Zhang et al. [Zhang-19], in which the performance of a Kalman filter, an extended Kalman filter, an unscented Kalman filter, and variations of these types of filters were compared for inertial navigation systems, the best accuracy is obtained by the unscented Kalman filter for their experiments. However, the unscented Kalman filter is the algorithm that demands the most computational effort among their comparison. On the other hand, the computational time required for the Kalman filter (not extended nor unscented) showed to be the lowest, 3 to 10 times smaller than the extended or unscented Kalman filter implementation, at the cost of having 6 to 8 times smaller accuracy in the estimates.

Following the current development needs of PADSs, particularly for the micro-lightweight category, as well as the goals established by the AGAS program, in which the improvements of low-cost systems are prioritized even at the expense of decreasing the landing accuracy, a total state-space formulation of a Kalman filter is adopted for the estimation scheme proposed in this investigation. This type of implementation enables the use of low-cost, small, and lightweight sensors and processing units, requiring a linear model that represents the flight dynamics of the system.

The purpose of the estimation scheme is the determination of the position and attitude of PADSs, given the availability of onboard sensors as an Inertial Measurement Unit (IMU) and a GNSS receiver, together with a model that represents the flight dynamics of the parafoil-payload system.

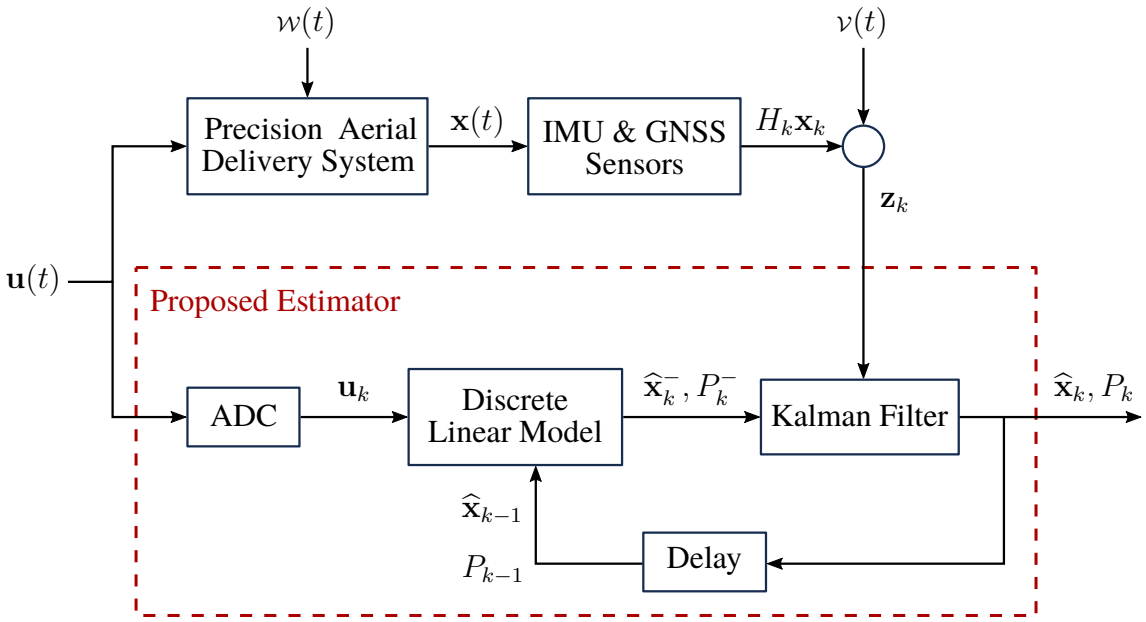

Fig. 4.1. Proposed estimation scheme.

The estimation scheme developed and implemented in this research is presented in Fig. 4.1.

The estimation process begins with the control inputs $\mathbf{u}(t)$, which are executed by the actuators of the PADS as brake deflections that modify the shape of the canopy, steering the system towards the desired landing target. The control inputs are initially processed through an Analog-to-Digital Converter (ADC), to be incorporated into a discrete linear model representative of the flight dynamics of the system, with process noise w. The complete description of the linear models developed for this implementation is detailed in Sections 5.4 and 5.5.

The epoch-wise output states of the linear model $\widehat{\mathbf{x}}_k^-$ are combined with the measurements $\mathbf{z}_k$ from the IMU and GNSS receiver, contaminated with measurement noise v, through the implementation of a total state-space Kalman filter, providing the best estimate $\widehat{\mathbf{x}}_k$ of the position and attitude of the system, together with its error covariance P_k. A detailed explanation of the filter formulation is presented in Chapter 2.

The estimation process is performed every time a set of measurements is received from the sensors, depending on the sampling rate defined for the system represented by the delay block. A comprehensive description of the sampling rate and the characteristics of the sensors used is presented in the following Section 4.1. In addition, the impact of the sampling rate on the performance of the

TABLE 4.1. SENSORS STATISTICAL PARAMETERS

Sensor	Measurement Standard Deviation
GNSS (xy)	$1.8\,\mathrm{m}$
GNSS (z)	$5\,\mathrm{m}$
Magnetometer	$0.5\,\mathrm{deg}$
Gyroscope	$0.1\,\mathrm{deg/s}$
Accelerometer	$0.12\,\mathrm{m/s^2}$

estimation is presented in Section 6.1.1.

The a posteriori estimates of the filter ($\widehat{x}_k$, P_k) are used to predict the new a priori estimates ($\widehat{x}_k^-$, P_k^-), completing the recursive prediction-correction nature of the filter.

4.1. Sensors Characterization

The hardware under consideration must comply with the requirements of a lightweight mission, where the allocated volume and weight for the low-cost sensors are very limited. Since this estimation scheme is intended to be used in low-cost applications.

To evaluate the performance of the estimation scheme, simulated measurements are generated at $5\,\mathrm{Hz}$ sampling rate, based on the state variables of the reference model and the statistical characteristics of the sensors acquiring this information in practice. This characterization is obtained through experimentation with real flight data from similar vehicles. Specifically, measurements from a GNSS receiver, a magnetometer, a gyroscope, and an accelerometer, are simulated by corrupting the position, angular position, angular velocity, and linear acceleration, of the reference model with white Gaussian noise, according to the statistical parameters reported in Table 4.1.

The obtained deviation values from experimentation are similar in comparison to the noise and bias values reported in similar experiments. For example, Slegers and Yakimenko [Slegers-11b] present a bias in GPS measurements of $2\,\mathrm{m}$, plus noise of $0.5\,\mathrm{m}$; $2\,\mathrm{deg}$ bias and $1\,\mathrm{deg}$ noise for the angular position; and finally, $1\,\mathrm{deg/s}$ bias and $1\,\mathrm{deg/s}$ noise for the angular velocity. In their study, they also draw upon a linearization process of the flight dynamics with a sampling rate of $2\,\mathrm{Hz}$,

assuming constant aerodynamic velocity. Cacan et al. [Cacan-15] report $4\,\mathrm{Hz}$ sampling rate for their guidance, navigation, and control algorithm, of a micro-lightweight PADS. Ward et al. [Ward-10] report noise with a standard deviation of $2\,\mathrm{m}$ in positioning measurements, and a standard deviation of $10\,\mathrm{deg}$ and $2\,\mathrm{deg}$ for the heading measurement bias and noise respectively, using $4\,\mathrm{Hz}$ sampling rate.

The sampling rate of $5\,\mathrm{Hz}$ for our investigation was chosen according to the processing capabilities of typical low-end microprocessors and sensors. For example, low-cost GNSS receivers as the u-blox NEO-6M or NEO-M8N can provide navigation information up to $1\,\mathrm{Hz}$ to $5\,\mathrm{Hz}$, limiting the measurement availability [u-blox-13; u-blox-20].

Typical performance of processing units for this lightweight and low-cost application range from a microprocessor with 8-bit, $20\,\mathrm{MHz}$ capabilities, as the ATmega328 chip [Atmel-18]; 32-bit, $216\,\mathrm{MHz}$ as the STM32F765 chip [STMicroelectronics-17]; up to 64-bit, $1.5\,\mathrm{GHz}$ as the BCM2711 chip [Broadcom-20].

5. Modeling the Flight Dynamics of PADSs

This chapter presents the derivation of the equations of motion that govern the flight dynamics of a parafoil-payload system, suitable for lightweight low-cost applications of PADSs. These equations are described in the body reference frame with a North-East-Down (NED) coordinate system, accounting for 6-DOF corresponding to the linear ($\mathbf{v}$) and angular ($\boldsymbol{\omega}$) velocity vectors, with components (u, v, w) and (p, q, r), respectively. The first part of this chapters introduces a nonlinear 6-DOF dynamic model, and then the development of two linear alternatives: a linearized version of the nonlinear 6-DOF model, and a double integrator model.

To validate the accuracy of the models proposed in this research, and for comparison purposes, the 6-DOF model developed and tested by Ward et al. [Ward-12] is adopted as reference (henceforth denoted as the reference model). This model is based on the system identification of a series of flight tests, using a micro-lightweight PADS with a total mass of $2.37\,\mathrm{kg}$ and a canopy with a wingspan of $1.77\,\mathrm{m}$, fitting the objective of this investigation. It captures the nonlinearities of the flight dynamics of the parafoil-payload system, therefore, it will serve as a reference to evaluate the performance of the linear models developed in this study.

5.1. Kinematic Equations of Motion

The kinematic equations provide the relation between the components of the linear velocity (u, v, w) and angular velocity (p, q, r) vectors in the body reference frame, to the components of the inertial velocity $(\dot{x}, \dot{y}, \dot{z})$ and angular velocity $(\dot{\phi}, \dot{\theta}, \dot{\psi})$ vectors:

$$\begin{pmatrix} \dot{x} \\ \dot{y} \\ \dot{z} \end{pmatrix} = T_{BI} \begin{pmatrix} u \\ v \\ w \end{pmatrix} \tag{5.1}$$

$$\begin{pmatrix} \dot{\phi} \\ \dot{\theta} \\ \dot{\psi} \end{pmatrix} = S_{BI} \begin{pmatrix} p \\ q \\ r \end{pmatrix} \tag{5.2}$$

where T_{BI} and S_{BI} are the rotation matrices that transform the linear and angular velocity components from the body to the inertial reference frame:

$$T_{BI} = \begin{bmatrix} \mathrm{c}_\theta \mathrm{c}_\psi & \mathrm{s}_\phi \mathrm{s}_\theta \mathrm{c}_\psi - \mathrm{c}_\phi \mathrm{s}_\psi & \mathrm{c}_\phi \mathrm{s}_\theta \mathrm{c}_\psi + \mathrm{s}_\phi \mathrm{s}_\psi \\ \mathrm{c}_\theta \mathrm{s}_\psi & \mathrm{s}_\phi \mathrm{s}_\theta \mathrm{s}_\psi + \mathrm{c}_\phi \mathrm{c}_\psi & \mathrm{c}_\phi \mathrm{s}_\theta \mathrm{s}_\psi - \mathrm{s}_\phi \mathrm{c}_\psi \\ -\mathrm{s}_\theta & \mathrm{s}_\phi \mathrm{c}_\theta & \mathrm{c}_\phi \mathrm{c}_\theta \end{bmatrix} \tag{5.3}$$

$$S_{BI} = \begin{bmatrix} 1 & \mathrm{s}_\phi \mathrm{t}_\theta & \mathrm{c}_\phi \mathrm{t}_\theta \\ 0 & \mathrm{c}_\phi & -\mathrm{s}_\phi \\ 0 & \mathrm{s}_\phi / \mathrm{c}_\theta & \mathrm{c}_\phi / \mathrm{c}_\theta \end{bmatrix} \tag{5.4}$$

where the shorthand notation c_*, s_*, and t_* denotes $\cos(*)$, $\sin(*)$, and $\tan(*)$, respectively.

5.2. Dynamic Equations of Motion

The equations of motion of the reference model are derived from Newtonian mechanics, considering the parafoil-payload system as a rigid body, i.e., without relative motion between the parafoil and the payload. The dynamic equations are obtained by relating the time derivative of the linear and angular momentum to the sum of forces and moments, about the Center of Gravity (CG) in the body reference frame:

$$\dot{\mathbf{L}} = \sum \boldsymbol{F} \tag{5.5}$$

$$\dot{\mathbf{H}} = \sum \boldsymbol{M}_{cg} \ . \tag{5.6}$$

The forces under consideration include the aerodynamic forces that act on each element of the canopy ($\boldsymbol{F}_{A,i}$). The canopy is discretized in seven elements, allowing for brake deflections only in the outermost elements. The deflection of the left (δ_L) and right (δ_R) brakes provide steerability to the system, by changing the lift and drag coefficients of the corresponding element of the canopy.

Additionally, the aerodynamic forces acting on the payload ($\boldsymbol{F}_{A,P}$), and the weight of the parafoil-payload system ($\boldsymbol{F}_W$) are included. Finally, apparent mass forces and moments, caused by the acceleration of the fluid through which the vehicle moves, are considered according to [Lissaman-93]. Since the dynamic equations are obtained in a rotating reference frame (non-inertial), fictitious forces

($\boldsymbol{F}_F$) and moments ($\boldsymbol{M}_F$) emerge in the equations for the change of linear and angular momentum. For a detailed explanation on the system identification for the parafoil-payload system, refer to Ward et al. [Ward-10; Ward-12].

Incorporating the aforementioned forces into (5.5) and (5.6), results in the dynamic equations of the reference model, representing the change of the state vector as the change in linear and angular velocity in the body reference frame $\dot{\mathbf{x}} = (\dot{u}, \dot{v}, \dot{w}, \dot{p}, \dot{q}, \dot{r})^T$:

$$m\left(\begin{pmatrix}\dot{u}\\ \dot{v}\\ \dot{w}\end{pmatrix} + S_\omega^B \begin{pmatrix}u\\ v\\ w\end{pmatrix}\right) = \boldsymbol{F}_W + \boldsymbol{F}_{AM} + \boldsymbol{F}_{A,P} + \sum_i \boldsymbol{F}_{A,i} \tag{5.7}$$

$$I_T \begin{pmatrix}\dot{p}\\ \dot{q}\\ \dot{r}\end{pmatrix} + S_\omega^B I_T \begin{pmatrix}p\\ q\\ r\end{pmatrix} = \boldsymbol{M}_{AM} + S_{\mathrm{cg},M}^B \boldsymbol{F}_{AM} + S_{\mathrm{cg},P}^B \boldsymbol{F}_{A,P} + \sum_i S_{\mathrm{cg},i}^B \boldsymbol{F}_{A,i} \tag{5.8}$$

where the skew-symmetric matrix S_X^B is used to express the cross product of two vectors:

$$S_\omega^B = \begin{bmatrix} 0 & -r & q \\ r & 0 & -p \\ -q & p & 0 \end{bmatrix} \tag{5.9}$$

$$S_{\mathrm{cg},M}^B = \begin{bmatrix} 0 & -z_{AM} & y_{AM} \\ z_{AM} & 0 & -x_{AM} \\ -y_{AM} & x_{AM} & 0 \end{bmatrix} \tag{5.10}$$

$$S_{\mathrm{cg},P}^B = \begin{bmatrix} 0 & -z_P & y_P \\ z_P & 0 & -x_P \\ -y_P & x_P & 0 \end{bmatrix} \tag{5.11}$$

$$S_{\mathrm{cg},i}^B = \begin{bmatrix} 0 & -z_i & y_i \\ z_i & 0 & -x_i \\ -y_i & x_i & 0 \end{bmatrix}. \tag{5.12}$$

The subscript represents the vector to operate the cross product, whereas the superscript rep-

resents the reference frame where the vectors are express. For example, $S^B_{\mathrm{cg},P}\boldsymbol{F}_{A,P}$ represents the cross product of the position vector of the payload, with components (x_P, y_P, z_P) expressed in the body reference frame (superscript *B*) from the center of gravity (subscript cg), and the aerodynamic force vector of the payload $\boldsymbol{F}_{A,P}$.

The vectors used to compute the cross products correspond to the angular velocity ($\boldsymbol{\omega}$), the position vector from the CG to the reference frame of each canopy element $S^B_{\mathrm{cg},i}$, the position vector from the CG to the center of pressure of the canopy for the apparent mass effect $S^B_{\mathrm{cg},M}$, and the position vector from the CG to the center of mass of the payload $S^B_{\mathrm{cg},P}$. Finally, I_T represents the inertia matrix of the complete system:

$$I_T = \begin{bmatrix} I_{XX} & I_{XY} & I_{XZ} \\ I_{XY} & I_{YY} & I_{YZ} \\ I_{XZ} & I_{YZ} & I_{ZZ} \end{bmatrix} . \tag{5.13}$$

In the following, the nonlinear equations of each of the forces and moments acting in the parafoil-payload system are presented, with physical properties according to the system identification of Ward et al. [Ward-10; Ward-12]. As part of the proposed methodology developed in this research, these nonlinear equations will be further linearized to be incorporated in the estimation scheme.

5.2.1 Weight (*W*)

The force caused by the mass of the parafoil-payload system, located at the CG, is expressed as:

$$\boldsymbol{F}_W = \begin{pmatrix} X_W \\ Y_W \\ Z_W \end{pmatrix} = mg \begin{pmatrix} -\mathrm{s}_\theta \\ \mathrm{s}_\phi \mathrm{c}_\theta \\ \mathrm{c}_\phi \end{pmatrix} \tag{5.14}$$

where m accounts for the total mass of the system ($2.37\,\mathrm{kg}$), and g represents the gravitational constant ($9.81\,\mathrm{m/s^2}$).

It is relevant to notice that the weight force does not depend directly on the states variables (u, v, w, p, q, r) nor on the control inputs (δ_L, δ_R).

5.2.2 Apparent Mass Force (*AM*)

The motion of an object through a fluid, sets the fluid around the object in motion, introducing forces and moments acting on the system. These effects are denominated Apparent Mass (AM) effects. For a detailed description on the history, development and modeling of apparent masses in the context of parachute aerodynamics, refer to Cockrell [Cockrell-91].

The magnitude of the apparent mass effect relates to the mass ratio between the total mass of the vehicle and the displaced air mass while flying. While for heavy aircraft these effects are negligible, for light parafoil-payload systems these are significant and must be taken into account. For the application under study, these effects are described according to the models introduced by Lissaman [Lissaman-93], quantifying the resultant force and moment exerted on the vehicle as:

$$\boldsymbol{F}_{AM} = \begin{pmatrix} X_{AM} \\ Y_{AM} \\ Z_{AM} \end{pmatrix} = -I_{AM} \left(\begin{pmatrix} \dot{u} \\ \dot{v} \\ \dot{w} \end{pmatrix} - S^{B}_{\mathrm{cg},M} \begin{pmatrix} \dot{p} \\ \dot{q} \\ \dot{r} \end{pmatrix} \right) \tag{5.15}$$

$$\boldsymbol{M}_{AM} = \begin{pmatrix} L_{AM} \\ M_{AM} \\ N_{AM} \end{pmatrix} = -I_{AI} \begin{pmatrix} \dot{p} \\ \dot{q} \\ \dot{r} \end{pmatrix} \tag{5.16}$$

with apparent mass (I_{AM}) and inertia (I_{AI}) tensors, according to the properties of the parafoil-payload system:

$$I_{AM} = \begin{bmatrix} A & 0 & 0 \\ 0 & B & 0 \\ 0 & 0 & C \end{bmatrix} = \begin{bmatrix} 0.02 & 0 & 0 \\ 0 & 0.13 & 0 \\ 0 & 0 & 0.64 \end{bmatrix} \quad (\mathrm{kg}) \tag{5.17}$$

$$I_{AI} = \begin{bmatrix} P & 0 & 0 \\ 0 & Q & 0 \\ 0 & 0 & R \end{bmatrix} = \begin{bmatrix} 0.011 & 0 & 0 \\ 0 & 0.013 & 0 \\ 0 & 0 & 0.006 \end{bmatrix} \quad (\mathrm{kg} \cdot \mathrm{m}^2)\,. \tag{5.18}$$

The results presented by Ward et al. [Ward-12] from the system identification of the vehicle do not report the position vector from the CG to the respective centroid where the apparent mass and

moments are applied. Consequently, these values are assumed according to the definitions of the model presented by Lissaman, where the elements of the position vector correspond the distance from the center of mass of the parafoil-payload system, to the centroid of the enclosed volume by the canopy. Assuming a symmetric assembly of the parafoil with respect to the payload, the estimated components of the position vector of the CG to the centroid where the apparent mass force and moment are applied are:

$$(x_{AM}, y_{AM}, z_{AM})^T = (0, 0, -1.1)^T \qquad (m)\,. \tag{5.19}$$

5.2.3 Aerodynamic Forces - Canopy (*A,i*)

The aerodynamic forces in the canopy are function of the relative velocity of the elements of the canopy with respect to the air through which it navigates. The relative velocity, also denoted aerodynamic velocity, of the *i*th element of the canopy is expressed as:

$$\begin{pmatrix} \tilde{u}_i \\ \tilde{v}_i \\ \tilde{w}_i \end{pmatrix} = T_{B,i} \left(\begin{pmatrix} u \\ v \\ w \end{pmatrix} - S^B_{\mathrm{cg},i} \begin{pmatrix} p \\ q \\ r \end{pmatrix} - T_{IB} \begin{pmatrix} V_{W,x} \\ V_{W,y} \\ V_{W,z} \end{pmatrix} \right) \tag{5.20}$$

where $V_{W,x}$, $V_{W,y}$, and $V_{W,z}$ correspond to the components of the external wind vector $\boldsymbol{\lambda}$. The aerodynamic forces are function of the aerodynamic velocity, and are expressed in terms of the Lift (L) and Drag (D) components:

$$F_{A,i} = \begin{pmatrix} X_{A,i} \\ Y_{A,i} \\ Z_{A,i} \end{pmatrix} = \frac{1}{2}\rho S_i \left[T_{B,i}\right]^T \left(C_{L,i}\sqrt{\tilde{u}_i^2 + \tilde{w}_i^2} \begin{pmatrix} \tilde{w}_i \\ 0 \\ -\tilde{u}_i \end{pmatrix} - C_{D,i}\sqrt{\tilde{u}_i^2 + \tilde{v}_i^2 + \tilde{w}_i^2} \begin{pmatrix} \tilde{u}_i \\ \tilde{v}_i \\ \tilde{w}_i \end{pmatrix} \right) \tag{5.21}$$

where ρ represents the density of the air with standard value of $1.225\,\mathrm{kg/m^3}$, which is assumed to remain constant throughout the entire flight. Additionally, $T_{B,i}$ represents the transformation matrix

TABLE 5.1. CANOPY AERODYNAMIC COEFFICIENTS

Element	C_{LA}	C_{DA2}	C_{D0}	C_{DB}	C_{DB3}
1	1.4	2	0.11	0.03	0.1
2	2.32	2	0.11	0.03	0.1
3	2.54	2	0.11	0.03	0.1
4	2.32	2	0.11	0.03	0.1
5	1.4	2	0.11	0.03	0.1
6	0	2	0.11	0.03	0.1
7	0	2	0.11	0.03	0.1

from the body reference frame to a reference frame attached to the *i*th element of the canopy:

$$T_{B,i} = \mathrm{R}_{\phi_i}\mathrm{R}_{\theta_i} = \begin{bmatrix} \mathrm{c}_\theta & 0 & -\mathrm{s}_\theta \\ \mathrm{s}_\phi\mathrm{s}_\theta & \mathrm{c}_\phi & \mathrm{s}_\phi\mathrm{c}_\theta \\ \mathrm{c}_\phi\mathrm{s}_\theta & -\mathrm{s}_\phi & \mathrm{c}_\phi\mathrm{c}_\theta \end{bmatrix}_i . \tag{5.22}$$

The lift and drag coefficients are obtained from the system characterization of the vehicle, for each of the elements of the canopy:

$$C_{L,i} = C_{LA,i}\,\alpha_i \tag{5.23}$$

$$C_{D,i} = C_{D0,i} + C_{DA2,i}\,\alpha_i^2 + C_{DB,i}\,\delta_i + C_{DB3,i}\,\delta_i^3 \tag{5.24}$$

where each aerodynamic coefficient is reported in Table 5.1.

The brake deflections δ_i are applied only in the outermost elements. Consequently, the brake deflections of the first through the fifth element are zero ($\delta_1 = \delta_2 = \delta_3 = \delta_4 = \delta_5 = 0$), whereas the brake deflection of the sixth element is denoted as the left brake deflection ($\delta_6 = \delta_L$), and the brake deflection of the seventh element is denoted as the right brake deflection ($\delta_7 = \delta_R$). The left and right deflections are normalized and can take any value from -1 to 1 (dimensionless).

Both, drag and lift formulations, are functions of the angle of attack of each of the canopy

TABLE 5.2. CANOPY GEOMETRIC PROPERTIES

	Size (m^2)	Orientation (deg)		Distance from CG (m)		
Element	S	ϕ	θ	x_{AM}	y_{AM}	z_{AM}
1	0.28	35	−18	0	0.44	−1.11
2	0.28	17.5	−18	0	0.22	−1.18
3	0.28	0	−18	0	0	−1.2
4	0.28	−17.5	−18	0	−0.22	−1.18
5	0.28	−35	−18	0	−0.44	−1.11
6	0.1	90	0	−0.5	0.8	−1
7	0.1	−90	0	−0.5	−0.8	−1

elements, expressed as:

$$\alpha_i = \tan^{-1}\left(\frac{\tilde{w}_i}{\tilde{u}_i}\right). \tag{5.25}$$

Finally, the moments caused by the aerodynamic forces acting on the canopy, are computed as the cross product between the position vector of each canopy element and its corresponding aerodynamic vector force:

$$\boldsymbol{M}_{A,i} = S^B_{\mathrm{cg},i}\boldsymbol{F}_{A,i}\,. \tag{5.26}$$

The geometric properties of the elements that constitute the canopy are detailed in Table 5.2.

5.2.4 Aerodynamic Force - Payload (*A,P*)

The relative velocity of the payload $(\tilde{u}_P, \tilde{v}_P, \tilde{w}_P)^T$ is computed in the same manner as the relative velocity for the *i*th element of the canopy $(\tilde{u}_i, \tilde{v}_i, \tilde{w}_i)^T$ in (5.20), without the need of the transformation from the body frame to the canopy frame $T_{B,i}$, equivalent to setting $T_{B,i}$ as the identity matrix I:

$$\begin{pmatrix}\tilde{u}_P\\ \tilde{v}_P\\ \tilde{w}_P\end{pmatrix} = I\left(\begin{pmatrix}u\\ v\\ w\end{pmatrix} - S^B_{\mathrm{cg},P}\begin{pmatrix}p\\ q\\ r\end{pmatrix} - T_{IB}\begin{pmatrix}V_{W,x}\\ V_{W,y}\\ V_{W,z}\end{pmatrix}\right). \tag{5.27}$$

The corresponding aerodynamic force in the payload is only composed by the drag component, since it is considered that the payload has no contribution from the lift component:

$$\boldsymbol{F}_{A,P} = \begin{pmatrix} X_{A,P} \\ Y_{A,P} \\ Z_{A,P} \end{pmatrix} = -\frac{1}{2}\rho S_P C_{D,P} \sqrt{\tilde{u}_P^2 + \tilde{v}_P^2 + \tilde{w}_P^2} \begin{pmatrix} \tilde{u}_P \\ \tilde{v}_P \\ \tilde{w}_P \end{pmatrix} \tag{5.28}$$

with reference area $S_p = 0.0325\,\mathrm{m}^2$, and drag coefficient $C_{D,P} = 0.3$ [Ward-10; Ward-12].

The location of the center of mass of the payload is not reported by the system identification process, and therefore is assumed. The geometry of the payload is assumed as a right rectangular cuboid, approximating the inertia of the complete parafoil-payload system (5.13):

$$I_T = \begin{bmatrix} I_{XX} & I_{XY} & I_{XZ} \\ I_{XY} & I_{YY} & I_{YZ} \\ I_{XZ} & I_{YZ} & I_{ZZ} \end{bmatrix} = \begin{bmatrix} 0.423 & 0 & 0.0298 \\ 0 & 0.401 & 0 \\ 0.0298 & 0 & 0.0529 \end{bmatrix} \qquad (\mathrm{kg}\cdot\mathrm{m}^2) \tag{5.29}$$

resulting in the following components of the position vector, with respect to the CG of the parafoil-payload system

$$(x_P, y_P, z_P)^T = (0.018, 0, 0.10)^T \qquad (m)\,. \tag{5.30}$$

The moment caused by the aerodynamic forces acting in the payload, is computed as the cross product between the position vector of the payload and the aerodynamic force of the payload:

$$\boldsymbol{M}_{A,P} = S^B_{\mathrm{cg},P} \boldsymbol{F}_{A,P}\,. \tag{5.31}$$

5.2.5 Fictitious Force ($\boldsymbol{F}$)

The equations of motion of the parafoil-payload system are derived in the body reference frame. This frame is attached to the vehicle, therefore rotating and translating accordingly. Since the equations of motion are derived in a non-inertial reference frame, fictitious forces emerge in the formulation.

The derivation of the fictitious forces and moments is a well known procedure from Newtonian mechanics, emerging from the calculation of the total derivative of a rotating vector. From the

rotational part of the change in linear and angular momentum, the fictitious forces and moments are calculated as:

$$\boldsymbol{F}_F = -mS_\omega^B \mathbf{v} = -m \begin{bmatrix} 0 & -r & q \\ r & 0 & -p \\ -q & p & 0 \end{bmatrix} \begin{pmatrix} u \\ v \\ w \end{pmatrix} = -m \begin{pmatrix} -rv + qw \\ ru - pw \\ -qu + pv \end{pmatrix} \tag{5.32}$$

$$\begin{aligned} \boldsymbol{M}_F = -S_\omega^B I_T \boldsymbol{\omega} = - & \begin{bmatrix} 0 & -r & q \\ r & 0 & -p \\ -q & p & 0 \end{bmatrix} \begin{bmatrix} I_{XX} & 0 & I_{XZ} \\ 0 & I_{YY} & 0 \\ I_{XZ} & 0 & I_{ZZ} \end{bmatrix} \begin{pmatrix} p \\ q \\ r \end{pmatrix} \\ = & \begin{pmatrix} -pqI_{XZ} - qr(I_{ZZ} - I_{YY}) \\ -pr(I_{XX} - I_{ZZ}) + p^2 I_{XZ} - r^2 I_{XZ} \\ -pq(I_{YY} - I_{XX}) + rqI_{XZ} \end{pmatrix} \end{aligned} \tag{5.33}$$

where the elements I_{XY} and I_{YZ}, of the inertial matrix, have been substituted according to the values in (5.29).

5.3. State-Space Representation

This section presents the derivation of the state-space representation for the dynamic equations of motion. This representation is useful for the analysis of the equations in terms of their components, the incorporation of the dynamic models into the Kalman filter, and for comparison purposes with respect to other models. The chosen states to represent the dynamics of the system are the components of the linear and angular velocities, u, v, w, p, q, and r, in the body reference frame. The derivation of the state-space representation of the equations of motion as a linear system is shown in the following section of this chapter.

As mentioned in Section 5.2, the dynamic equations are obtained by relating the time derivative of the linear and angular momentum to the sum of forces and moments, about the CG in the body reference frame:

$$\dot{\mathbf{L}} = \sum \boldsymbol{F} \tag{5.5 revisited}$$

$$\dot{\mathbf{H}} = \sum \boldsymbol{M}_{\text{cg}} \, . \tag{5.6 revisited}$$

The time derivative of the linear and angular momentum for a rigid body are defined as:

$$\dot{\mathbf{L}} = m\left(\dot{\mathbf{v}} + \boldsymbol{\omega} \times \mathbf{v}\right) = m\dot{\mathbf{v}} + mS_{\omega}^{B}\mathbf{v} \tag{5.34}$$

$$\dot{\mathbf{M}} = I_T\dot{\boldsymbol{\omega}} + \boldsymbol{\omega} \times I_T\boldsymbol{\omega} = I_T\dot{\boldsymbol{\omega}} + S_{\omega}^{B}I_T\boldsymbol{\omega} \tag{5.35}$$

which incorporated into the conservation equations for linear and angular momentum, together with the described forces and moments presented in Section 5.2.1 to Section 5.2.4, result in the dynamic equations of motion (5.5) and (5.6), rewritten in compact form:

$$m\dot{\mathbf{v}} + mS_{\omega}^{B}\mathbf{v} = \boldsymbol{F}_W + \boldsymbol{F}_{AM} + \boldsymbol{F}_{A,P} + \sum_i \boldsymbol{F}_{A,i} \tag{5.36}$$

$$I_T\dot{\boldsymbol{\omega}} + S_{\omega}^{B}I_T\boldsymbol{\omega} = \boldsymbol{M}_{AM} + S_{\text{cg},M}^{B}\boldsymbol{F}_{AM} + S_{\text{cg},P}^{B}\boldsymbol{F}_{A,P} + \sum_i S_{\text{cg},i}^{B}\boldsymbol{F}_{A,i} \, . \tag{5.37}$$

Expanding the apparent mass force and moment:

$$m\dot{\mathbf{v}} + mS_{\omega}^{B}\mathbf{v} = \boldsymbol{F}_W - I_{AM}\dot{\mathbf{v}} + I_{AM}S_{\text{cg},M}^{B}\dot{\boldsymbol{\omega}} + \boldsymbol{F}_{A,P} + \textstyle\sum_i \boldsymbol{F}_{A,i} \tag{5.38}$$

$$I_T\dot{\boldsymbol{\omega}} + S_{\omega}^{B}I_T\boldsymbol{\omega} = -I_{AI}\dot{\boldsymbol{\omega}} - S_{\text{cg},M}^{B}I_{AM}\dot{\mathbf{v}} + S_{\text{cg},M}^{B}I_{AM}S_{\text{cg},M}^{B}\dot{\boldsymbol{\omega}} + S_{\text{cg},P}^{B}\boldsymbol{F}_{A,P} + \textstyle\sum_i S_{\text{cg},i}^{B}\boldsymbol{F}_{A,i} \, . \tag{5.39}$$

Solving for the derivative of the states, expressed in vector form as $\dot{\mathbf{v}}$ and $\dot{\boldsymbol{\omega}}$ respectively:

$$m\dot{\mathbf{v}} + I_{AM}\dot{\mathbf{v}} - I_{AM}S_{\text{cg},M}^{B}\dot{\boldsymbol{\omega}} = -mS_{\omega}^{B}\mathbf{v} + \boldsymbol{F}_W + \boldsymbol{F}_{A,P} + \textstyle\sum_i \boldsymbol{F}_{A,i} \tag{5.40}$$

$$I_T\dot{\boldsymbol{\omega}} + I_{AI}\dot{\boldsymbol{\omega}} + S_{\text{cg},M}^{B}I_{AM}\dot{\mathbf{v}} - S_{\text{cg},M}^{B}I_{AM}S_{\text{cg},M}^{B}\dot{\boldsymbol{\omega}} = -S_{\omega}^{B}I_T\boldsymbol{\omega} + S_{\text{cg},P}^{B}\boldsymbol{F}_{A,P} + \textstyle\sum_i S_{\text{cg},i}^{B}\boldsymbol{F}_{A,i} \, . \tag{5.41}$$

Grouping common terms, and substituting the definition of the fictitious force and moment, as well as the payload and canopy aerodynamic moments:

$$\left(m + I_{AM}\right)\dot{\mathbf{v}} - I_{AM}S_{\text{cg},M}^{B}\dot{\boldsymbol{\omega}} = \boldsymbol{F}_F + \boldsymbol{F}_W + \boldsymbol{F}_{A,P} + \textstyle\sum_i \boldsymbol{F}_{A,i} \tag{5.42}$$

$$S_{\text{cg},M}^{B}I_{AM}\dot{\mathbf{v}} + \left(I_T + I_{AI} - S_{\text{cg},M}^{B}I_{AM}S_{\text{cg},M}^{B}\right)\dot{\boldsymbol{\omega}} = \boldsymbol{M}_F + \boldsymbol{M}_{A,P} + \textstyle\sum_i \boldsymbol{M}_{A,i} \, . \tag{5.43}$$

Rearranging in matrix form, and expanding the linear and angular velocity vectors into their respective components, to display the derivative of the states $\dot{u}, \dot{v}, \dot{w}, \dot{p}, \dot{q}, \dot{r}$:

$$\begin{bmatrix} mI + I_{AM} & -I_{AM}S^B_{\text{cg},M} \\ S^B_{\text{cg},M}I_{AM} & I_T + I_{AI} - S^B_{\text{cg},M}I_{AM}S^B_{\text{cg},M} \end{bmatrix} \begin{pmatrix} \dot{u} \\ \dot{v} \\ \dot{w} \\ \dot{p} \\ \dot{q} \\ \dot{r} \end{pmatrix} = \begin{pmatrix} \boldsymbol{F}_F + \boldsymbol{F}_W + \boldsymbol{F}_{A,P} + \sum_i \boldsymbol{F}_{A,i} \\ \boldsymbol{M}_F + \boldsymbol{M}_{A,P} + \sum_i \boldsymbol{M}_{A,i} \end{pmatrix} \tag{5.44}$$

where I represents the identity matrix.

Solving for the derivative of the states ($\dot{\mathbf{x}}$), the equations of motion can be expressed in compact form as:

$$\dot{\mathbf{x}} = [GM]^{-1} \begin{pmatrix} \boldsymbol{F}_F + \boldsymbol{F}_W + \boldsymbol{F}_{A,P} + \sum_i \boldsymbol{F}_{A,i} \\ \boldsymbol{M}_F + \boldsymbol{M}_{A,P} + \sum_i \boldsymbol{M}_{A,i} \end{pmatrix} \tag{5.45}$$

where the matrix GM incorporates the geometry, mass, and inertial properties of the parafoil-payload system of the reference model.

As it can be noted from the formulation of each of the components of (5.45), the resulting equations of motion that govern the flight dynamics of the parafoil-payload system are nonlinear. While this is expected due to the complex nature of the forces and moments acting on the vehicle, this has important consequences for the estimation of the states, based on low-cost sensors and a discrete Kalman filter, as described in detail in Chapter 4. Consequently, a linear model that captures the flight dynamics of the parafoil-payload system is to be developed, to implement a discrete Kalman filter suitable for low-cost applications, with weight restrictions and limited computational resources.

In the following sections, the linearization of each of the forces and moments is presented, where the mathematical formulation for the partial derivatives of the forces and moments with respect to each of the state variables and control inputs are derived. Notice that the weight does not depend on the state variables, nor on the control inputs, therefore a linearization is not derived for this force.

5.4. Linearization of the Equations of Motion

The linear approximation of the equations of motion is computed as the first-order Taylor series, evaluated around stable points of the states and inputs ($\mathbf{x}_s, \mathbf{u}_s$). Considering the general form of the Taylor series:

$$f(\mathbf{x}) = \sum_{n=0}^{\infty} \frac{f^n(a)}{n!}(\mathbf{x} - a)^n \tag{5.46}$$

where $f^n(a)$ represents the *n*th derivative of the function $f(\mathbf{x})$ evaluated at a, adopting the conventions $f^0(\mathbf{x}) = f(\mathbf{x})$ and $0! = 1$.

For the multivariable case under study $f(\mathbf{x}, \mathbf{u}) = f(u, v, w, p, q, r, \delta_L, \delta_R)$, each of the forces and moments that the system experiences can be expressed as a power series representation in the form:

$$\begin{aligned} f(\mathbf{x}, \mathbf{u}) = f(\mathbf{x}_s, \mathbf{u}_s) &+ \left.\frac{\partial f}{\partial u}\right|_{\mathbf{x}_s, \mathbf{u}_s} (u - u_s) + \left.\frac{\partial f}{\partial v}\right|_{\mathbf{x}_s, \mathbf{u}_s} (v - v_s) + \left.\frac{\partial f}{\partial w}\right|_{\mathbf{x}_s, \mathbf{u}_s} (w - w_s) \\ &+ \left.\frac{\partial f}{\partial p}\right|_{\mathbf{x}_s, \mathbf{u}_s} (p - p_s) + \left.\frac{\partial f}{\partial q}\right|_{\mathbf{x}_s, \mathbf{u}_s} (q - q_s) + \left.\frac{\partial f}{\partial r}\right|_{\mathbf{x}_s, \mathbf{u}_s} (r - r_s) \\ &+ \left.\frac{\partial f}{\partial \delta_L}\right|_{\mathbf{x}_s, \mathbf{u}_s} (\delta_L - \delta_{L_s}) + \left.\frac{\partial f}{\partial \delta_R}\right|_{\mathbf{x}_s, \mathbf{u}_s} (\delta_R - \delta_{R_s}) + \mathcal{O} \end{aligned} \tag{5.47}$$

where $\mathcal{O}$ represent higher order terms of the Taylor series, neglected for the linearization.

Since the rigging of the parafoil-payload system is fixed, any given control inputs result in a unique trim condition. In addition to the control inputs, defining initial conditions in the nonlinear model, results in stable states ($\mathbf{x}_s$, $\mathbf{u}_s$), since no wind nor other perturbations are considered. The stabilization period for the vehicle under analysis is approximately $10\,\mathrm{s}$, depending on the magnitude of the maneuver. The stable states and stable control inputs are denoted:

$$\mathbf{x}_s = (u_s, v_s, w_s, p_s, q_s, r_s)^T \tag{5.48}$$

$$\mathbf{u}_s = (\delta_{L_s}, \delta_{R_s})^T . \tag{5.49}$$

Applying this linearization method to the equation of motion (5.44) around the stable points (5.48) and (5.49), and grouping common terms, results in the equation of motion of the linearized

6-DOF model:

$$\dot{\mathbf{x}} = [GM]^{-1} \left(\begin{pmatrix} \boldsymbol{F}_s \\ \boldsymbol{M}_s \end{pmatrix} + \begin{bmatrix} \frac{\partial \boldsymbol{F}}{\partial u} & \frac{\partial \boldsymbol{F}}{\partial v} & \frac{\partial \boldsymbol{F}}{\partial w} & \frac{\partial \boldsymbol{F}}{\partial p} & \frac{\partial \boldsymbol{F}}{\partial q} & \frac{\partial \boldsymbol{F}}{\partial r} \\ \frac{\partial \boldsymbol{M}}{\partial u} & \frac{\partial \boldsymbol{M}}{\partial v} & \frac{\partial \boldsymbol{M}}{\partial w} & \frac{\partial \boldsymbol{M}}{\partial p} & \frac{\partial \boldsymbol{M}}{\partial q} & \frac{\partial \boldsymbol{M}}{\partial r} \end{bmatrix} \begin{pmatrix} u-u_s \\ v-v_s \\ w-w_s \\ p-p_s \\ q-q_s \\ r-r_s \end{pmatrix} + \begin{bmatrix} \frac{\partial \boldsymbol{F}}{\partial \delta_L} & \frac{\partial \boldsymbol{F}}{\partial \delta_R} \\ \frac{\partial \boldsymbol{M}}{\partial \delta_L} & \frac{\partial \boldsymbol{M}}{\partial \delta_R} \end{bmatrix} \begin{pmatrix} \delta_L - \delta_{Ls} \\ \delta_R - \delta_{Rs} \end{pmatrix} \right) \tag{5.50}$$

where $\boldsymbol{F}_s$ and $\boldsymbol{M}_s$ represent the forces and moments evaluated at the stable points.

The linearized equations of motion (5.50) can be expressed in compact form as:

$$\dot{\mathbf{x}} = [GM]^{-1} \left(\begin{pmatrix} \boldsymbol{F}_s \\ \boldsymbol{M}_s \end{pmatrix} + J^{\mathbf{x}}(\mathbf{x} - \mathbf{x}_s) + J^{\mathbf{u}}(\mathbf{u} - \mathbf{u}_s) \right) \tag{5.51}$$

where $J^{\mathbf{x}}$ and $J^{\mathbf{u}}$ represent the corresponding Jacobian matrices.

In the following, the derivation of the elements of the Jacobian matrices is presented, by obtaining the linearized form of the forces and moments present in the equation of motion (5.45). The linearization is performed with respect to the state variables (u, v, w, p, q, r) and control inputs (δ_L, δ_R), by evaluating the nonlinear equations at the stable state points $(\mathbf{x}_s)$ and stable control inputs $(\mathbf{u}_s)$, according to the truncated Taylor series expansion (5.47).

5.4.1 Linearized Aerodynamic Forces - Canopy (*A,i*)

Assuming there is no external wind vector ($\boldsymbol{\lambda} = 0$), the components of the relative velocity vector in (5.20) can be expressed in terms of the linear and angular velocity components of the

parafoil-payload system, represented in the body reference frame:

$$\begin{pmatrix}\tilde{u}_i\\ \tilde{v}_i\\ \tilde{w}_i\end{pmatrix} = [T_{B,i}]\left(\begin{pmatrix}u\\ v\\ w\end{pmatrix} - S^B_{\text{cg},i}\begin{pmatrix}p\\ q\\ r\end{pmatrix} - [T_{IB}]\begin{pmatrix}V_{W,x}\\ V_{W,y}\\ V_{W,z}\end{pmatrix}\right)$$

$$= [T_{B,i}]\left(\begin{pmatrix}u\\ v\\ w\end{pmatrix} - \begin{bmatrix}0 & -z_i & y_i\\ z_i & 0 & -x_i\\ -y_i & x_i & 0\end{bmatrix}\begin{pmatrix}p\\ q\\ r\end{pmatrix}\right)$$

$$= \begin{bmatrix}\mathrm{c}_\theta & 0 & -\mathrm{s}_\theta\\ \mathrm{s}_\phi\mathrm{s}_\theta & \mathrm{c}_\phi & \mathrm{s}_\phi\mathrm{c}_\theta\\ \mathrm{c}_\phi\mathrm{s}_\theta & -\mathrm{s}_\phi & \mathrm{c}_\phi\mathrm{c}_\theta\end{bmatrix}\begin{pmatrix}u + z_iq - y_ir\\ v - z_ip + x_ir\\ w + y_ip - x_iq\end{pmatrix} = \begin{bmatrix}c_1 & c_2 & c_3\\ c_4 & c_5 & c_6\\ c_7 & c_8 & c_9\end{bmatrix}\begin{pmatrix}u + z_iq - y_ir\\ v - z_ip + x_ir\\ w + y_ip - x_iq\end{pmatrix}$$

$$\begin{pmatrix}\tilde{u}_i\\ \tilde{v}_i\\ \tilde{w}_i\end{pmatrix} = \begin{pmatrix}uc_1 + vc_2 + wc_3 + p(c_3y_i - c_2z_i) + q(c_1z_i - c_3x_i) + r_i(c_2x_i - c_1y_i)\\ uc_4 + vc_5 + wc_6 + p(c_6y_i - c_5z_i) + q(c_4z_i - c_6x_i) + r_i(c_5x_i - c_4y_i)\\ uc_7 + vc_8 + wc_9 + p(c_9y_i - c_8z_i) + q(c_7z_i - c_9x_i) + r_i(c_8x_i - c_7y_i)\end{pmatrix} \tag{5.52}$$

where the coefficient c_j represents the *j*th element of the rotation matrix $T_{B,i}$.

Recalling the aerodynamic force equation (5.21):

$$\boldsymbol{F}_{A,i} = \begin{pmatrix}X_{A,i}\\ Y_{A,i}\\ Z_{A,i}\end{pmatrix} = \frac{1}{2}\rho S_i\,[T_{B,i}]^T\left(C_{L,i}\sqrt{\tilde{u}_i^2 + \tilde{w}_i^2}\begin{pmatrix}\tilde{w}_i\\ 0\\ -\tilde{u}_i\end{pmatrix} - C_{D,i}\sqrt{\tilde{u}_i^2 + \tilde{v}_i^2 + \tilde{w}_i^2}\begin{pmatrix}\tilde{u}_i\\ \tilde{v}_i\\ \tilde{w}_i\end{pmatrix}\right) \tag{5.21 revisited}$$

the inverse transformation of the components of the relative velocity vector, from the reference frame attached to the *i*th element of the canopy, to the body reference frame, is computed as:

$$[T_{B,i}]^T\begin{pmatrix}\tilde{w}_i\\ 0\\ -\tilde{u}_i\end{pmatrix} = \begin{bmatrix}c_1 & c_4 & c_7\\ 0 & c_5 & c_8\\ c_3 & c_6 & c_9\end{bmatrix}\begin{pmatrix}\tilde{w}_i\\ 0\\ -\tilde{u}_i\end{pmatrix} = \begin{pmatrix}c_1\tilde{w}_i - c_7\tilde{u}_i\\ -c_8\tilde{u}_i\\ c_3\tilde{w}_i - c_9\tilde{u}_i\end{pmatrix} = \mathbf{v}_{R,L,i} \tag{5.53}$$

$$[T_{B,i}]^T \begin{pmatrix} \tilde{u}_i \\ \tilde{v}_i \\ \tilde{w}_i \end{pmatrix} = \cancel{[T_{B,i}]^T [T_{B,i}]}^{\,I} \begin{pmatrix} u + z_i q - y_i r \\ v - z_i p + x_i r \\ w + y_i p - x_i q \end{pmatrix} = \mathbf{v}_{R,D,i} \tag{5.54}$$

where the notation $\mathbf{v}_{R,L,i}$ and $\mathbf{v}_{R,D,i}$ is adopted, corresponding to the relative (R) velocity vector in the lift (L) and drag (D) direction, respectively, for each *i*th element.

Rewriting the aerodynamic force equation in short-hand notation:

$$\boldsymbol{F}_{A,i} = k_i C_{L,i} A_i \mathbf{v}_{R,L,i} - k_i C_{D,i} B_i \mathbf{v}_{R,D,i} \tag{5.55}$$

where $k_i = \frac{1}{2}\rho S_i$, $A_i = \sqrt{\tilde{u}_i^2 + \tilde{w}_i^2}$, and $B_i = \sqrt{\tilde{u}_i^2 + \tilde{v}_i^2 + \tilde{w}_i^2}$.

The partial derivative of the canopy aerodynamic force (5.55), is written using the dot notation to represent the derivative of a variable with respect to each of the state variables and control inputs:

$$\begin{aligned} \frac{\partial \boldsymbol{F}_{A,i}}{\partial(u,v,w,p,q,r,\delta_L,\delta_R)} = \frac{\partial \boldsymbol{F}_{A,i}}{\partial(\mathbf{x},\mathbf{u})} &= k_i \left[\dot{C}_{L,i} A_i \mathbf{v}_{R,L,i} + C_{L,i}\left(\dot{A}_i \mathbf{v}_{R,L,i} + A_i \dot{\mathbf{v}}_{R,L,i}\right)\right] \\ &\quad - k_i \left[\dot{C}_{D,i} B_i \mathbf{v}_{R,D,i} + C_{D,i}\left(\dot{B}_i \mathbf{v}_{R,D,i} + B_i \dot{\mathbf{v}}_{R,D,i}\right)\right]. \end{aligned} \tag{5.56}$$

In the following, the partial derivatives of each term of (5.56) are presented:

$$A_i = \sqrt{\tilde{u}_i^2 + \tilde{w}_i^2} \tag{5.57}$$

$$\frac{\partial A_i}{\partial u} = \frac{\tilde{u}_i c_1 + \tilde{w}_i c_7}{A_i} \tag{5.58}$$

$$\frac{\partial A_i}{\partial v} = \frac{\tilde{u}_i c_2 + \tilde{w}_i c_8}{A_i} \tag{5.59}$$

$$\frac{\partial A_i}{\partial w} = \frac{\tilde{u}_i c_3 + \tilde{w}_i c_9}{A_i} \tag{5.60}$$

$$\frac{\partial A_i}{\partial p} = \frac{\tilde{u}_i (c_3 y_i - c_2 z_i) + \tilde{w}_i (c_9 y_i - c_8 z_i)}{A_i} \tag{5.61}$$

$$\frac{\partial A_i}{\partial q} = \frac{\tilde{u}_i (c_1 z_i - c_3 x_i) + \tilde{w}_i (c_7 z_i - c_9 x_i)}{A_i} \tag{5.62}$$

$$\frac{\partial A_i}{\partial r} = \frac{\tilde{u}_i (c_2 x_i - c_1 y_i) + \tilde{w}_i (c_8 x_i - c_7 y_i)}{A_i} \tag{5.63}$$

$$\frac{\partial A_i}{\partial \delta_i} = 0 \tag{5.64}$$

$$B_i = \sqrt{\tilde{u}_i^2 + \tilde{v}_i^2 + \tilde{w}_i^2} \tag{5.65}$$

$$\frac{\partial B_i}{\partial u} = \frac{\tilde{u}_i c_1 + \tilde{v}_i c_4 + \tilde{w}_i c_7}{B_i} \tag{5.66}$$

$$\frac{\partial B_i}{\partial v} = \frac{\tilde{u}_i c_2 + \tilde{v}_i c_5 + \tilde{w}_i c_8}{B_i} \tag{5.67}$$

$$\frac{\partial B_i}{\partial w} = \frac{\tilde{u}_i c_3 + \tilde{v}_i c_6 + \tilde{w}_i c_9}{B_i} \tag{5.68}$$

$$\frac{\partial B_i}{\partial p} = \frac{\tilde{u}_i(c_3 y_i - c_2 z_i) + \tilde{v}_i(c_6 y_i - c_5 z_i) + \tilde{w}_i(c_9 y_i - c_8 z_i)}{B_i} \tag{5.69}$$

$$\frac{\partial B_i}{\partial q} = \frac{\tilde{u}_i(c_1 z_i - c_3 x_i) + \tilde{v}_i(c_4 z_i - c_6 x_i) + \tilde{w}_i(c_7 z_i - c_9 x_i)}{B_i} \tag{5.70}$$

$$\frac{\partial B_i}{\partial r} = \frac{\tilde{u}_i(c_2 x_i - c_1 y_i) + \tilde{v}_i(c_5 x_i - c_4 y_i) + \tilde{w}_i(c_8 x_i - c_7 y_i)}{B_i} \tag{5.71}$$

$$\frac{\partial B_i}{\partial \delta_i} = 0 \tag{5.72}$$

$$C_{L,i} = C_{LA,i}\alpha_i \tag{5.23 revisited}$$

$$C_{D,i} = C_{D0,i} + C_{DA2,i}\,\alpha_i^2 + C_{DB,i}\,\delta_i + C_{DB3,i}\,\delta_i^3 \tag{5.24 revisited}$$

$$\alpha = \tan^{-1}\left(\frac{\tilde{w}_i}{\tilde{u}_i}\right) \tag{5.25 revisited}$$

$$\frac{\partial C_{L,i}}{\partial (u, v, w, p, q, r)} = C_{LA,i}\,\dot{\alpha}_i \tag{5.73}$$

$$\frac{\partial C_{L,i}}{\partial \delta_i} = 0 \tag{5.74}$$

$$\frac{\partial C_{D,i}}{\partial (u, v, w, p, q, r)} = 2C_{DA2,i}\,\alpha_i\,\dot{\alpha}_i \tag{5.75}$$

$$\frac{\partial C_{D,i}}{\partial \delta_i} = C_{DB,i} + 3C_{DB3,i}\,\delta_i^2 \tag{5.76}$$

$$\frac{\partial}{\partial u}\left(\frac{\tilde{w}_i}{\tilde{u}_i}\right) = \frac{\tilde{u}_i c_7 - \tilde{w}_i c_1}{\tilde{u}_i^2} \tag{5.77}$$

$$\frac{\partial}{\partial v}\left(\frac{\tilde{w}_i}{\tilde{u}_i}\right) = \frac{\tilde{u}_i c_8 - \tilde{w}_i c_2}{\tilde{u}_i^2} \tag{5.78}$$

$$\frac{\partial}{\partial w}\left(\frac{\tilde{w}_i}{\tilde{u}_i}\right) = \frac{\tilde{u}_i c_9 - \tilde{w}_i c_3}{\tilde{u}_i^2} \tag{5.79}$$

$$\frac{\partial}{\partial p}\left(\frac{\tilde{w}_i}{\tilde{u}_i}\right) = \frac{\tilde{u}_i(c_9 y_i - c_8 z_i) - \tilde{w}_i(c_3 y_i - c_2 z_i)}{\tilde{u}_i^2} \tag{5.80}$$

$$\frac{\partial}{\partial q}\left(\frac{\tilde{w}_i}{\tilde{u}_i}\right) = \frac{\tilde{u}_i(c_7 z_i - c_9 x_i) - \tilde{w}_i(c_1 z_i - c_3 x_i)}{\tilde{u}_i^2} \tag{5.81}$$

$$\frac{\partial}{\partial r}\left(\frac{\tilde{w}_i}{\tilde{u}_i}\right) = \frac{\tilde{u}_i(c_8 x_i - c_7 y_i) - \tilde{w}_i(c_2 x_i - c_1 y_i)}{\tilde{u}_i^2} \tag{5.82}$$

$$\frac{\partial \alpha_i}{\partial u} = \frac{\tilde{u}_i c_7 - \tilde{w}_i c_1}{\tilde{u}_i^2 + \tilde{w}_i^2} \tag{5.83}$$

$$\frac{\partial \alpha_i}{\partial v} = \frac{\tilde{u}_i c_8 - \tilde{w}_i c_2}{\tilde{u}_i^2 + \tilde{w}_i^2} \tag{5.84}$$

$$\frac{\partial \alpha_i}{\partial w} = \frac{\tilde{u}_i c_9 - \tilde{w}_i c_3}{\tilde{u}_i^2 + \tilde{w}_i^2} \tag{5.85}$$

$$\frac{\partial \alpha_i}{\partial p} = \frac{\tilde{u}_i(c_9 y_i - c_8 z_i) - \tilde{w}_i(c_3 y_i - c_2 z_i)}{\tilde{u}_i^2 + \tilde{w}_i^2} \tag{5.86}$$

$$\frac{\partial \alpha_i}{\partial q} = \frac{\tilde{u}_i(c_7 z_i - c_9 x_i) - \tilde{w}_i(c_1 z_i - c_3 x_i)}{\tilde{u}_i^2 + \tilde{w}_i^2} \tag{5.87}$$

$$\frac{\partial \alpha_i}{\partial r} = \frac{\tilde{u}_i(c_8 x_i - c_7 y_i) - \tilde{w}_i(c_2 x_i - c_1 y_i)}{\tilde{u}_i^2 + \tilde{w}_i^2} \tag{5.88}$$

$$\frac{\partial \alpha_i}{\partial \delta_i} = 0 \tag{5.89}$$

$$\mathbf{v}_{R,L,i} = \begin{pmatrix} c_1\tilde{w}_i - c_7\tilde{u}_i \\ -c_8\tilde{u}_i \\ c_3\tilde{w}_i - c_9\tilde{u}_i \end{pmatrix} \tag{5.53 revisited}$$

$$\frac{\partial \mathbf{v}_{R,L,i}}{\partial u} = \begin{pmatrix} 0 \\ -c_8c_1 \\ -(c_1c_9 - c_3c_7) \end{pmatrix} \tag{5.90}$$

$$\frac{\partial \mathbf{v}_{R,L,i}}{\partial v} = \begin{pmatrix} c_1c_8 \\ 0 \\ c_3c_8 \end{pmatrix} \tag{5.91}$$

$$\frac{\partial \mathbf{v}_{R,L,i}}{\partial w} = \begin{pmatrix} c_1c_9 - c_3c_7 \\ -c_8c_3 \\ 0 \end{pmatrix} \tag{5.92}$$

$$\frac{\partial \mathbf{v}_{R,L,i}}{\partial p} = \begin{pmatrix} y_i(c_1c_9 - c_3c_7) - z_ic_1c_8 \\ -y_ic_3c_8 \\ -z_ic_3c_8 \end{pmatrix} \tag{5.93}$$

$$\frac{\partial \mathbf{v}_{R,L,i}}{\partial q} = \begin{pmatrix} -x_i(c_1c_9 - c_3c_7) \\ x_ic_3c_8 - z_ic_1c_8 \\ -z_i(c_1c_9 - c_3c_7) \end{pmatrix} \tag{5.94}$$

$$\frac{\partial \mathbf{v}_{R,L,i}}{\partial r} = \begin{pmatrix} x_ic_1c_8 \\ y_ic_1c_8 \\ x_ic_3c_8 + y_i(c_1c_9 - c_3c_7) \end{pmatrix} \tag{5.95}$$

$$\frac{\partial \mathbf{v}_{R,L,i}}{\partial \delta_i} = 0 \tag{5.96}$$

$$\mathbf{v}_{R,D,i} = \begin{pmatrix} u + z_i q - y_i r \\ v - z_i p + x_i r \\ w + y_i p - x_i q \end{pmatrix} \tag{5.54 revisited}$$

$$\frac{\partial \mathbf{v}_{R,D,i}}{\partial u} = \begin{pmatrix} 1 \\ 0 \\ 0 \end{pmatrix} \tag{5.97}$$

$$\frac{\partial \mathbf{v}_{R,D,i}}{\partial v} = \begin{pmatrix} 0 \\ 1 \\ 0 \end{pmatrix} \tag{5.98}$$

$$\frac{\partial \mathbf{v}_{R,D,i}}{\partial w} = \begin{pmatrix} 0 \\ 0 \\ 1 \end{pmatrix} \tag{5.99}$$

$$\frac{\partial \mathbf{v}_{R,D,i}}{\partial p} = \begin{pmatrix} 0 \\ -z_i \\ y_i \end{pmatrix} \tag{5.100}$$

$$\frac{\partial \mathbf{v}_{R,D,i}}{\partial q} = \begin{pmatrix} z_i \\ 0 \\ -x_i \end{pmatrix} \tag{5.101}$$

$$\frac{\partial \mathbf{v}_{R,D,i}}{\partial r} = \begin{pmatrix} -y_i \\ x_i \\ 0 \end{pmatrix} \tag{5.102}$$

$$\frac{\partial \mathbf{v}_{R,D,i}}{\partial \delta_i} = 0\,. \tag{5.103}$$

The aerodynamic moments on the canopy are calculated as the cross product between the position

vector from the CG of the reference frame of each canopy element and the aerodynamic force vector:

$$\boldsymbol{M}_{A,i} = S^B_{\text{cg},i}\boldsymbol{F}_{A,i} = k_i C_{L,i} A_i S^B_{\text{cg},i}\mathbf{v}_{R,L,i} - k_i C_{D,i} B_i S^B_{\text{cg},i}\mathbf{v}_{R,D,i}\,. \tag{5.104}$$

To evaluate the partial derivatives, it is convenient to compute the cross products $S^B_{\text{cg},i}\mathbf{v}_{R,L,i}$ and $S^B_{\text{cg},i}\mathbf{v}_{R,D,i}$:

$$S^B_{\text{cg},i}\mathbf{v}_{R,L,i} = \begin{bmatrix} 0 & -z_i & y_i \\ z_i & 0 & -x_i \\ -y_i & x_i & 0 \end{bmatrix} \begin{pmatrix} c_1\tilde{w}_i - c_7\tilde{u}_i \\ -c_8\tilde{u}_i \\ c_3\tilde{w}_i - c_9\tilde{u}_i \end{pmatrix} \tag{5.105}$$

$$= \begin{pmatrix} \tilde{u}_i(c_8 z_i - c_9 y_i) + \tilde{w}_i c_3 y_i \\ \tilde{u}_i(c_9 x_i - c_7 z_i) + \tilde{w}_i(c_1 z_i - c_3 x_i) \\ \tilde{u}_i(c_7 y_i - c_8 x_i) - \tilde{w}_i c_1 y_i \end{pmatrix} = \boldsymbol{M}_{R,L,i} \tag{5.106}$$

$$S^B_{\text{cg},i}\mathbf{v}_{R,D,i} = \begin{bmatrix} 0 & -z_i & y_i \\ z_i & 0 & -x_i \\ -y_i & x_i & 0 \end{bmatrix} \begin{pmatrix} u + z_i q - y_i r \\ v - z_i p + x_i r \\ w + y_i p - x_i q \end{pmatrix} \tag{5.107}$$

$$= \begin{pmatrix} -z_i v_i + y_i w_i + (y_i^2 + z_i^2)p_i - y_i x_i q_i - z_i x_i r_i \\ z_i u_i - x_i w_i - x_i y_i p_i + (z_i^2 + x_i^2)q_i - z_i y_i r_i \\ -y_i u_i + x_i v_i - x_i z_i p_i - y_i z_i q_i + (y_i^2 + x_i^2)r_i \end{pmatrix} = \boldsymbol{M}_{R,D,i}\,. \tag{5.108}$$

Rewriting the canopy aerodynamic moment equation in compact form, leads to:

$$\boldsymbol{M}_{A,i} = k_i C_{L,i} A_i \boldsymbol{M}_{R,L,i} - k_i C_{D,i} B_i \boldsymbol{M}_{R,D,i} \tag{5.109}$$

from which the partial derivative with respect to each of the state variables and control inputs is obtained:

$$\frac{\partial \boldsymbol{M}_{A,i}}{\partial(\mathbf{x},\mathbf{u})} = k_i \left[\dot{C}_{L,i} A_i \boldsymbol{M}_{R,L,i} + C_{L,i}\left(\dot{A}_i \boldsymbol{M}_{R,L,i} + A_i \dot{\mathbf{M}}_{R,L,i}\right)\right]$$

$$- k_i \left[\dot{C}_{D,i} B_i \boldsymbol{M}_{R,D,i} + C_{D,i} \left(\dot{B} \boldsymbol{M}_{R,D,i} + B \boldsymbol{M}_{R,D,i} \right) \right] . \tag{5.110}$$

In the following, the partial derivatives of each remaining term of (5.110) are presented:

$$\frac{\partial \boldsymbol{M}_{R,L,i}}{\partial u} = \begin{pmatrix} -y_i(c_1 c_9 - c_3 c_7) + z_i c_1 c_8 \\ x_i(c_1 c_9 - c_3 c_7) \\ -x_i c_1 c_8 \end{pmatrix} \tag{5.111}$$

$$\frac{\partial \boldsymbol{M}_{R,L,i}}{\partial v} = \begin{pmatrix} y_i c_8 c_3 \\ z_i c_8 c_1 - x_i c_8 c_3 \\ -y_i c_8 c_1 \end{pmatrix} \tag{5.112}$$

$$\frac{\partial \boldsymbol{M}_{R,L,i}}{\partial w} = \begin{pmatrix} z_i c_3 c_8 \\ z_i(c_1 c_9 - c_3 c_7) \\ -x_i c_3 c_8 - y_i(c_1 c_9 - c_3 c_7) \end{pmatrix} \tag{5.113}$$

$$\frac{\partial \boldsymbol{M}_{R,L,i}}{\partial p} = \begin{pmatrix} 0 \\ y_i z_i(c_1 c_9 - c_3 c_7) + x_i z_i c_3 c_8 - z_i^2 c_1 c_8 \\ -x_i y_i c_3 c_8 - y_i^2(c_1 c_9 - c_3 c_7) + y_i z_i c_1 c_8 \end{pmatrix} \tag{5.114}$$

$$\frac{\partial \boldsymbol{M}_{R,L,i}}{\partial q} = \begin{pmatrix} -y_i z_i(c_1 c_9 - c_3 c_7) - x_i z_i c_3 c_8 + z_i^2 c_1 c_8 \\ 0 \\ x_i y_i(c_1 c_9 - c_3 c_7) - x_i z_i c_1 c_8 + x_i^2 c_3 c_8 \end{pmatrix} \tag{5.115}$$

$$\frac{\partial \boldsymbol{M}_{R,L,i}}{\partial r} = \begin{pmatrix} x_i y_i c_3 c_8 - y_i z_i c_1 c_8 + y_i^2(c_1 c_9 - c_3 c_7) \\ -x_i y_i(c_1 c_9 - c_3 c_7) + x_i z_i c_1 c_8 - x_i^2 c_3 c_8 \\ 0 \end{pmatrix} \tag{5.116}$$

$$\frac{\partial \boldsymbol{M}_{R,L,i}}{\partial \delta_i} = 0 \tag{5.117}$$

$$\frac{\partial \boldsymbol{M}_{R,D,i}}{\partial u} = \begin{pmatrix} 0 \\ z_i \\ -y_i \end{pmatrix} \tag{5.118}$$

$$\frac{\partial \boldsymbol{M}_{R,D,i}}{\partial v} = \begin{pmatrix} -z_i \\ 0 \\ x_i \end{pmatrix} \tag{5.119}$$

$$\frac{\partial \boldsymbol{M}_{R,D,i}}{\partial w} = \begin{pmatrix} y_i \\ -x_i \\ 0 \end{pmatrix} \tag{5.120}$$

$$\frac{\partial \boldsymbol{M}_{R,D,i}}{\partial p} = \begin{pmatrix} y_i^2 + z_i^2 \\ -x_i y_i \\ -x_i z_i \end{pmatrix} \tag{5.121}$$

$$\frac{\partial \boldsymbol{M}_{R,D,i}}{\partial q} = \begin{pmatrix} -x_i y_i \\ x_i^2 + z_i^2 \\ -y_i z_i \end{pmatrix} \tag{5.122}$$

$$\frac{\partial \boldsymbol{M}_{R,D,i}}{\partial r} = \begin{pmatrix} -x_i z_i \\ -y_i z_i \\ x_i^2 + y_i^2 \end{pmatrix} \tag{5.123}$$

$$\tag{5.124}$$

$$\frac{\partial \boldsymbol{M}_{R,D,i}}{\partial \delta_i} = 0\,. \tag{5.125}$$

5.4.2 Linearized Aerodynamic Force - Payload (*A,P*)

Considering the aerodynamic force equation for the payload (5.28)

$$\boldsymbol{F}_{A,P} = \begin{pmatrix} X_{A,P} \\ Y_{A,P} \\ Z_{A,P} \end{pmatrix} = -\frac{1}{2}\rho S_P C_{D,P} \sqrt{\tilde{u}_P^2 + \tilde{v}_P^2 + \tilde{w}_P^2} \begin{pmatrix} \tilde{u}_P \\ \tilde{v}_P \\ \tilde{w}_P \end{pmatrix} \tag{5.28 revisited}$$

where the relative velocity vector for the payload is computed according to (5.27), without considering any external wind vector:

$$\begin{pmatrix} \tilde{u}_P \\ \tilde{v}_P \\ \tilde{w}_P \end{pmatrix} = \left(\begin{pmatrix} u \\ v \\ w \end{pmatrix} - \begin{bmatrix} 0 & -z_P & \cancelto{0}{y_P} \\ z_P & 0 & -x_P \\ \cancelto{0}{-y_P} & x_P & 0 \end{bmatrix} \begin{pmatrix} p \\ q \\ r \end{pmatrix} \right) = \begin{pmatrix} u + qz_P \\ v - pz_P + rx_P \\ w - qx_P \end{pmatrix} = \mathbf{v}_{R,D,P} \tag{5.126}$$

where the geometry of the parafoil-payload system is assumed to be perfectly symmetrical with respect to its x-z plane. Consequently, the position of the CG of the payload is located in symmetry plane, leading to $y_p = 0$. The notation $\mathbf{v}_{R,D,P}$ is adopted, corresponding to the relative (R) velocity vector, for the drag (D) component of the payload (P).

Rewriting the aerodynamic force equation for the payload, in short notation:

$$\boldsymbol{F}_{A,P} = k_P E \mathbf{v}_{R,D,P} \tag{5.127}$$

where $k_P = -\frac{1}{2}\rho S_P C_{D,P}$ and $E = \sqrt{\tilde{u}_P^2 + \tilde{v}_P^2 + \tilde{w}_P^2}$.

The partial derivative of the payload aerodynamic force (5.127) with respect to each of the state variables and control inputs, is expressed in compact form as:

$$\frac{\partial \boldsymbol{F}_{A,P}}{\partial(\mathbf{x}, \mathbf{u})} = k_P \left(\dot{E} \mathbf{v}_{R,D,P} + E \dot{\mathbf{v}}_{R,D,P} \right). \tag{5.128}$$

In the following, the partial derivatives of each term of (5.128) is presented:

$$E = \sqrt{\tilde{u}_P^2 + \tilde{v}_P^2 + \tilde{w}_P^2} \tag{5.129}$$

$$\frac{\partial E}{\partial u} = \frac{\tilde{u}_P}{E} \tag{5.130}$$

$$\frac{\partial E}{\partial v} = \frac{\tilde{v}_P}{E} \tag{5.131}$$

$$\frac{\partial E}{\partial w} = \frac{\tilde{w}_P}{E} \tag{5.132}$$

$$\frac{\partial E}{\partial p} = -\frac{\tilde{v}_P z_P}{E} \tag{5.133}$$

$$\frac{\partial E}{\partial q} = \frac{\tilde{u}_P z_P - \tilde{w}_P x_P}{E} \tag{5.134}$$

$$\frac{\partial E}{\partial r} = \frac{\tilde{v}_P x_P}{E} \tag{5.135}$$

$$\frac{\partial E}{\partial \delta_i} = 0 \tag{5.136}$$

$$\frac{\partial \mathbf{v}_{R,D,P}}{\partial u} = \begin{pmatrix} 1 \\ 0 \\ 0 \end{pmatrix} \tag{5.137}$$

$$\frac{\partial \mathbf{v}_{R,D,P}}{\partial v} = \begin{pmatrix} 0 \\ 1 \\ 0 \end{pmatrix} \tag{5.138}$$

$$\frac{\partial \mathbf{v}_{R,D,P}}{\partial w} = \begin{pmatrix} 0 \\ 0 \\ 1 \end{pmatrix} \tag{5.139}$$

$$\frac{\partial \mathbf{v}_{R,D,P}}{\partial p} = \begin{pmatrix} 0 \\ -z_p \\ 0 \end{pmatrix} \tag{5.140}$$

$$\frac{\partial \mathbf{v}_{R,D,P}}{\partial q} = \begin{pmatrix} z_p \\ 0 \\ -x_p \end{pmatrix} \tag{5.141}$$

$$\frac{\partial \mathbf{v}_{R,D,P}}{\partial r} = \begin{pmatrix} 0 \\ x_p \\ 0 \end{pmatrix} \tag{5.142}$$

$$\frac{\partial \mathbf{v}_{R,D,P}}{\partial \delta_i} = 0\,. \tag{5.143}$$

The payload aerodynamic moments are calculated as the cross product between the position vector from the CG to the center of mass of the payload, and the payload aerodynamic force vector:

$$\boldsymbol{M}_{A,P} = S^B_{\mathrm{cg},P}\boldsymbol{F}_{A,P} = k_P E S^B_{\mathrm{cg},P}\mathbf{v}_{R,D,P}\,. \tag{5.144}$$

To facilitate the evaluation of the partial derivatives of the moment equation, it is convenient to compute the cross product $S^B_{\mathrm{cg},P}\mathbf{v}_{R,D,P}$:

$$S^B_{\mathrm{cg},P}\mathbf{v}_{R,D,P} = \begin{bmatrix} 0 & -z_P & 0 \\ z_P & 0 & -x_P \\ 0 & x_P & 0 \end{bmatrix} \begin{pmatrix} \tilde{u}_P \\ \tilde{v}_P \\ \tilde{w}_P \end{pmatrix} \tag{5.145}$$

$$= \begin{bmatrix} 0 & -z_P & 0 \\ z_P & 0 & -x_P \\ 0 & x_P & 0 \end{bmatrix} \begin{pmatrix} u + qz_P \\ v - pz_P + rx_P \\ w - qx_P \end{pmatrix} \tag{5.146}$$

$$S^B_{\mathrm{cg},P}\mathbf{v}_{R,D,P} = \begin{pmatrix} -vz_P + pz_P^2 - rz_P x_P \\ uz_P - wx_P + q(z_P^2 + x_P^2) \\ vx_P - pz_P x_P + rx_P^2 \end{pmatrix} = \boldsymbol{M}_{R,D,P}\,. \tag{5.147}$$

Rewriting the payload aerodynamic moment equation in compact form:

$$\boldsymbol{M}_{A,P} = k_P E \boldsymbol{M}_{R,D,P}\,. \tag{5.148}$$

The partial derivative of the moments equation with respect to each of the state variables and control inputs is obtained in compact form as:

$$\frac{\partial \boldsymbol{M}_{A,P}}{\partial(\mathbf{x},\mathbf{u})} = k_P \left(\dot{E}\boldsymbol{M}_{R,D,P} + E\dot{\mathbf{M}}_{R,D,P} \right) \tag{5.149}$$

where the remaining partial derivative of (5.149) correspond to:

$$\frac{\partial \boldsymbol{M}_{R,D,P}}{\partial u} = \begin{pmatrix} 0 \\ z_P \\ 0 \end{pmatrix} \tag{5.150}$$

$$\frac{\partial \boldsymbol{M}_{R,D,P}}{\partial v} = \begin{pmatrix} -z_P \\ 0 \\ x_P \end{pmatrix} \tag{5.151}$$

$$\frac{\partial \boldsymbol{M}_{R,D,P}}{\partial w} = \begin{pmatrix} 0 \\ -x_P \\ 0 \end{pmatrix} \tag{5.152}$$

$$\frac{\partial \boldsymbol{M}_{R,D,P}}{\partial p} = \begin{pmatrix} z_P^2 \\ 0 \\ -z_P x_P \end{pmatrix} \tag{5.153}$$

$$\frac{\partial \boldsymbol{M}_{R,D,P}}{\partial q} = \begin{pmatrix} 0 \\ z_P^2 + x_P^2 \\ 0 \end{pmatrix} \tag{5.154}$$

$$\frac{\partial \boldsymbol{M}_{R,D,P}}{\partial r} = \begin{pmatrix} -z_P x_P \\ 0 \\ x_P^2 \end{pmatrix} \tag{5.155}$$

$$\frac{\partial \boldsymbol{M}_{R,D,P}}{\partial \delta_i} = 0\,. \tag{5.156}$$

5.4.3 Linearized Fictitious Force (F)

Considering the nonlinear equations for the fictitious force and moments:

$$\boldsymbol{F}_F = -mS_\omega^B \mathbf{v} = -m \begin{pmatrix} -rv + qw \\ ru - pw \\ -qu + pv \end{pmatrix} \tag{5.32 revisited}$$

$$\boldsymbol{M}_F = -S_\omega^B I_T \boldsymbol{\omega} = \begin{pmatrix} -pqI_{XZ} - qr(I_{ZZ} - I_{YY}) \\ -pr(I_{XX} - I_{ZZ}) + p^2 I_{XZ} - r^2 I_{XZ} \\ -pq(I_{YY} - I_{XX}) + rqI_{XZ} \end{pmatrix} \tag{5.33 revisited}$$

the partial derivative with respect to each of the state variables and control inputs are:

$$\frac{\partial \boldsymbol{F}_F}{\partial u} = -m \begin{pmatrix} 0 \\ r \\ -q \end{pmatrix} \tag{5.157}$$

$$\frac{\partial \boldsymbol{F}_F}{\partial v} = -m \begin{pmatrix} -r \\ 0 \\ p \end{pmatrix} \tag{5.158}$$

$$\frac{\partial \boldsymbol{F}_F}{\partial w} = -m \begin{pmatrix} q \\ -p \\ 0 \end{pmatrix} \tag{5.159}$$

$$\frac{\partial \boldsymbol{F}_F}{\partial p} = -m \begin{pmatrix} 0 \\ -w \\ v \end{pmatrix} \tag{5.160}$$

$$\frac{\partial \boldsymbol{F}_F}{\partial q} = -m \begin{pmatrix} w \\ 0 \\ -u \end{pmatrix} \tag{5.161}$$

$$\frac{\partial \boldsymbol{F}_F}{\partial r} = -m \begin{pmatrix} -v \\ u \\ 0 \end{pmatrix} \tag{5.162}$$

$$\frac{\partial \boldsymbol{F}_F}{\partial \delta_i} = 0 \tag{5.163}$$

$$\frac{\partial \boldsymbol{M}_F}{\partial (u, v, w)} = 0 \tag{5.164}$$

$$\frac{\partial \boldsymbol{M}_F}{\partial p} = \begin{pmatrix} -qI_{XZ} \\ -r(I_{XX} - I_{ZZ}) + 2pI_{XZ} \\ -q(I_{YY} - I_{XX}) \end{pmatrix} \tag{5.165}$$

$$\frac{\partial \boldsymbol{M}_F}{\partial q} = \begin{pmatrix} -pI_{XZ} - r(I_{ZZ} - I_{YY}) \\ 0 \\ -p(I_{YY} - I_{XX}) + rI_{XZ} \end{pmatrix} \tag{5.166}$$

$$\frac{\partial \boldsymbol{M}_F}{\partial r} = \begin{pmatrix} -q(I_{ZZ} - I_{YY}) \\ -p(I_{XX} - I_{ZZ}) - 2rI_{XZ} \\ qI_{XZ} \end{pmatrix} \tag{5.167}$$

$$\frac{\partial \boldsymbol{M}_F}{\partial \delta_i} = 0\,. \tag{5.168}$$

5.4.4 State Extrapolation

Recalling the linearized equation of motion expressed in compact form:

$$\dot{\mathbf{x}} = [GM]^{-1} \left(\begin{pmatrix} \boldsymbol{F}_s \\ \boldsymbol{M}_s \end{pmatrix} + J^{\mathbf{x}}(\mathbf{x} - \mathbf{x}_s) + J^{\mathbf{u}}(\mathbf{u} - \mathbf{u}_s) \right) \tag{5.51 revisited}$$

distributing the products and renaming constant terms leads to a state-space representation of the linear model as:

$$\dot{\mathbf{x}} = [GM]^{-1} J^{\mathbf{x}}\mathbf{x} + [GM]^{-1} J^{\mathbf{u}}\mathbf{u} + [GM]^{-1} \left(\begin{pmatrix} \boldsymbol{F}_s \\ \boldsymbol{M}_s \end{pmatrix} - J^{\mathbf{x}}\mathbf{x}_s - J^{\mathbf{u}}\mathbf{u}_s \right) \tag{5.169}$$

$$\dot{\mathbf{x}} = A\mathbf{x} + B\mathbf{u} + \boldsymbol{\varepsilon} \tag{5.170}$$

where:

$$A = [GM]^{-1} [J^{\mathbf{x}}] \tag{5.171}$$

$$B = [GM]^{-1} [J^{\mathbf{u}}] \tag{5.172}$$

$$\boldsymbol{\varepsilon} = [GM]^{-1} \left(\begin{pmatrix} \boldsymbol{F}_s \\ \boldsymbol{M}_s \end{pmatrix} - J^{\mathbf{x}}\mathbf{x}_s - J^{\mathbf{u}}\mathbf{u}_s \right). \tag{5.173}$$

Notice that matrices A and B are constant as long as the control inputs remain fixed, considerably simplifying the number of computations to be performed during flight. Similarly, all components of the vector $\boldsymbol{\varepsilon}$ are constant under the same condition, except for the components of the force produced by the weight of the vehicle ($\boldsymbol{F}_W$), which depend on its attitude.

Matrices A and B, as well as vector $\boldsymbol{\varepsilon}$, evaluated at the stable points for each maneuver segment, are given in Appendix C.

The complete description of the position and attitude of the PADS in the inertial reference frame, as well as the linear and angular velocity in the body reference frame, can be expressed in a concise form by combining the kinematic and dynamic equations of motion in a single state-space representation:

$$\begin{pmatrix} \dot{\boldsymbol{p}} \\ \dot{\boldsymbol{\Omega}} \\ \dot{\mathbf{v}} \\ \dot{\boldsymbol{\omega}} \end{pmatrix} = \begin{bmatrix} 0 & 0 & T_{BI} & 0 \\ 0 & 0 & 0 & S_{BI} \\ 0 & 0 & A_{11} & A_{12} \\ 0 & 0 & A_{21} & A_{22} \end{bmatrix} \begin{pmatrix} \boldsymbol{p} \\ \boldsymbol{\Omega} \\ \mathbf{v} \\ \boldsymbol{\omega} \end{pmatrix} + \begin{bmatrix} 0 & 0 \\ 0 & 0 \\ B_{11} & B_{11} \\ B_{21} & B_{22} \end{bmatrix} \begin{pmatrix} \delta_L \\ \delta_R \end{pmatrix} + \begin{pmatrix} 0 \\ 0 \\ \varepsilon_1 \\ \varepsilon_2 \end{pmatrix} \tag{5.174}$$

where matrices A and B, as well as the vector $\boldsymbol{\varepsilon}$ are distributed in components A_{ij}, B_{ij}, and ε_i

respectively, to accommodate for an adequate state-space representation. Additionally, T_{BI} and S_{BI} are the rotation matrices that transform the linear and angular velocity components from the body to the inertial reference frame, already presented in (5.3) and (5.4).

Rewriting (5.174) leads to a compact equation, where the superscript Li is used to indicate that an element corresponds to the linearized model:

$$\dot{\mathbf{x}}^{Li} = A^{Li}\mathbf{x}^{Li} + B^{Li}\mathbf{u}^{Li} + \boldsymbol{\varepsilon}^{Li}. \tag{5.175}$$

While (5.175) represents a time-continuous model, information from the onboard sensors arrive at discrete times. Solving the differential equation for the state vector using Euler's method, with time step Δt, a time-discrete model is obtained as:

$$\begin{aligned} \mathbf{x}_k^{Li} &= \left(A^{Li}\Delta t + I\right)\mathbf{x}_{k-1}^{Li} + B^{Li}\Delta t\mathbf{u}_{k-1}^{Li} + \boldsymbol{\varepsilon}_{k-1}^{Li}\Delta t \\ \mathbf{x}_k^{Li} &= F^{Li}\mathbf{x}_{k-1}^{Li} + G^{Li}\mathbf{u}_{k-1}^{Li} + \boldsymbol{\epsilon}_{k-1}^{Li} \end{aligned} \tag{5.176}$$

where I represents the identity matrix. It is relevant to observe that (5.176) describes 12 components in total, three for each vector: the position vector $\boldsymbol{p} = (x, y, z)^T$ and the angular position vector $\boldsymbol{\Omega} = (\phi, \theta, \psi)^T$, expressed in the inertial reference frame, with the latter corresponding to the Euler orientation angles (roll, pitch, yaw); and the linear velocity vector $\mathbf{v} = (u, v, w)^T$ and angular velocity vector $\boldsymbol{\omega} = (p, q, r)^T$, expressed in the body reference frame.

5.5. Double Integrator Dynamic Model

The development of an alternative linear model is achieved by exploiting the properties of the flight dynamics of PADSs. Since these are vehicles navigating in an underactuated controlled descent flight, typically without propulsion, and subject only to variations in the wind profiles, the flight dynamics are normally smooth, i.e., without sudden changes in the state variables of the parafoil-payload system, except for the voluntary control inputs exerted on the vehicle. Taking this into consideration, a double integrator model is proposed, based on the assumption that between consecutive measurements of the sensors acquiring information regarding the position and attitude of the vehicle, the linear ($\ddot{\boldsymbol{p}}$) and angular ($\ddot{\boldsymbol{\Omega}}$) accelerations remain constant for Δt seconds. Integrating

twice these accelerations with respect to time leads to the following equations of motion for the position and attitude, in the inertial reference frame:

$$\boldsymbol{p}_k = \boldsymbol{p}_{k-1} + \dot{\boldsymbol{p}}_{k-1}\Delta t + \ddot{\boldsymbol{p}}_{k-1}\Delta t^2/2 \tag{5.177}$$

$$\boldsymbol{\Omega}_k = \boldsymbol{\Omega}_{k-1} + \dot{\boldsymbol{\Omega}}_{k-1}\Delta t + \ddot{\boldsymbol{\Omega}}_{k-1}\Delta t^2/2 \tag{5.178}$$

which can be expressed in compact form as:

$$\begin{pmatrix} \boldsymbol{p} \\ \dot{\boldsymbol{p}} \\ \boldsymbol{\Omega} \\ \dot{\boldsymbol{\Omega}} \end{pmatrix}_k = \begin{bmatrix} 1 & \Delta t & 0 & 0 \\ 0 & 1 & 0 & 0 \\ 0 & 0 & 1 & \Delta t \\ 0 & 0 & 0 & 1 \end{bmatrix} \begin{pmatrix} \boldsymbol{p} \\ \dot{\boldsymbol{p}} \\ \boldsymbol{\Omega} \\ \dot{\boldsymbol{\Omega}} \end{pmatrix}_{k-1} + \begin{bmatrix} \frac{\Delta t^2}{2} & 0 \\ \Delta t & 0 \\ 0 & \frac{\Delta t^2}{2} \\ 0 & \Delta t \end{bmatrix} \begin{pmatrix} \ddot{\boldsymbol{p}} \\ \ddot{\boldsymbol{\Omega}} \end{pmatrix}_{k-1} \tag{5.179}$$

$$\mathbf{x}_k^D = F^D \mathbf{x}_{k-1}^D + G^D \mathbf{u}_{k-1}^D \tag{5.180}$$

where the superscript D is used to indicate that an element corresponds to the double integrator model. Notice that (5.180) also describes 12 components in total, corresponding to the position, linear velocity, angular position, and angular velocity vectors, in the inertial reference frame. The position and angular position vectors can be directly compared with the analogous components of the nonlinear and linearized models (5.176). Contrarily, the linear and angular velocity vectors obtained from the double integrator model cannot be directly compared with the similar components from the nonlinear or linearized models, since they are expressed in different reference frames. To be able to compare them, the linear and angular velocity vectors obtained from the double integrator model are transformed to the body reference frame with the rotation matrices T_{BI}^{-1} and S_{BI}^{-1}, respectively.

6. Sensor Fusion for Position and Attitude Estimation

Typically, PADSs are equipped with a GNSS receiver and an IMU, that provide information at discrete times about the position and attitude of the vehicle during its flight. The objective of any guidance, navigation, and control scheme is to process the incoming information from the sensors, in order to estimate the state variables of the system, to plan the most suitable trajectory towards the landing target while managing the energy budget.

This chapter presents the development, implementation, and comparison of a sensor fusion algorithm and estimation scheme for the position and attitude of PADSs, employing a Kalman filter based on two proposed 6-DOF dynamic models, suitable for lightweight low-cost applications.

The implementation is based on the proposed estimation scheme described in Chapter 4, where in Section 4.1 the required sensors and their characteristics suitable to perform the position and attitude estimation were presented. This implementation makes use of the dynamic models that characterize the flight of the parafoil-payload system, presented in Chapter 5, firstly introducing a nonlinear 6-DOF dynamic model, and then the development of two linear alternatives: a linearized version of the nonlinear 6-DOF model, and a double integrator model. The estimation scheme is based on the Kalman filter algorithm, that incorporates the dynamic models and measurements from different sensors, as explained in Chapter 2. The performance of the proposed estimation scheme is evaluated through simulations in this chapter, including the discussion of the results.

By assigning initial conditions and control inputs, the nonlinear equation of motion (5.45) can be solved, and the resulting components can be transformed to the inertial reference frame by rotating according to the Euler orientation angles.

$$\dot{\mathbf{x}} = [GM]^{-1} \begin{pmatrix} \boldsymbol{F}_F + \boldsymbol{F}_W + \boldsymbol{F}_{A,P} + \sum_i \boldsymbol{F}_{A,i} \\ \boldsymbol{M}_F + \boldsymbol{M}_{A,P} + \sum_i \boldsymbol{M}_{A,i} \end{pmatrix} \tag{5.45 revisited}$$

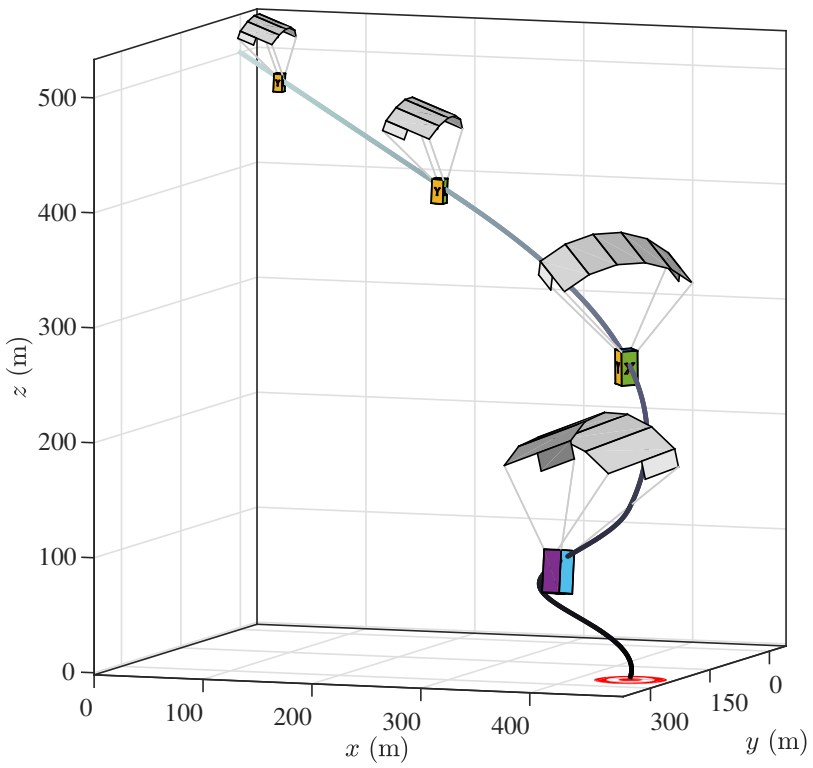

Fig. 6.1. Descent trajectory under study, followed by a Precision Aerial Delivery System (PADS) navigating towards a landing target (parafoil-payload system not to scale). The trajectory corresponds to the implementation of the 6-Degrees of Freedom (DOF) nonlinear reference model.

$$\begin{pmatrix} \dot{x} \\ \dot{y} \\ \dot{z} \end{pmatrix} = T_{BI} \begin{pmatrix} u \\ v \\ w \end{pmatrix} \qquad \text{(5.1 revisited)}$$

$$\begin{pmatrix} \dot{\phi} \\ \dot{\theta} \\ \dot{\psi} \end{pmatrix} = S_{BI} \begin{pmatrix} p \\ q \\ r \end{pmatrix} \qquad \text{(5.2 revisited)}$$

Instead of adopting the start of the descent trajectory as the origin of the inertial z component, this is translated to the intended point of landing to better represent visually the followed trajectory of the PADS. Fig. 6.1 presents the trajectory under study, constructed by implementing the 6-DOF nonlinear model (hereafter denoted as the reference model), executing the three maneuvers described in Table 6.1 as constant control inputs. This trajectory will serve as a reference for the analysis of

TABLE 6.1. CONTROL MANEUVER SEGMENTS

Maneuver Id.	**Start (s)**	δ_L	δ_R
t_1	0	0	0
t_2	26	0.1	0
t_3	80	0	-0.4

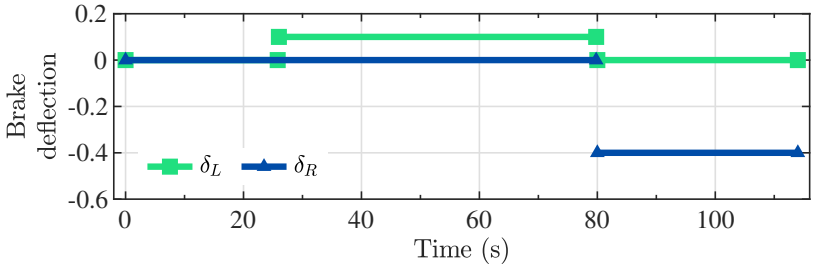

Fig. 6.2. Control maneuver segments graphically represented. The brake deflections shown correspond to the control segments reported in Table 6.1.

the linear models presented in the following sections of this work.[1]

The control inputs remain constant during the flight until the next maneuver is executed. For a better visualization of the control inputs, Fig. 6.2 presents the maneuver execution as described in Table 6.1.

For each of the three segments of constant inputs on the flight trajectory, a set of stable points is determined from the reference model as the resulting state vector. The sable points obtained for each maneuver segment, applying the brake deflections as stable control inputs δ_{Ls} and δ_{Rs}, are listed in Table 6.2.

For the Kalman filter implementation, the process noise covariance matrix is estimated using the autocorrelation function $Q = G\sigma^2 G^T$, with variance $\sigma_{Li}^2 = 800$ for the linearized model, and variance $\sigma_D^2 = 10$ for the double integrator model, determined by tuning the filter during its implementation. The simulated measurements are incorporated into the Kalman filter as the measurement vector $\mathbf{z}$, while the squared of the standard deviations of the characterized sensors (Table 4.1) are used as the elements of the diagonal measurement noise covariance matrix R.

[1] A video showing the descent trajectory flight is available as supplementary material at the research article Garcia-Huerta et al. *Sensors* 2020, 20, 5227 [Garcia-Huerta-20b].

TABLE 6.2. STABLE POINTS

State Variable	**Maneuver Segment**		
$\mathbf{x}_s$	t_1	t_2	t_3
u_s (m/s)	7.49	7.49	7.59
v_s (m/s)	0	0	-0.01
w_s (m/s)	4.09	4.09	4.12
p_s (deg/s)	0	0.06	0.50
q_s (deg/s)	0	0.04	1.46
r_s (deg/s)	0	1.67	10.55

The implementation of the filter using the linearized model is realized by executing the constant brake deflections described in Table 6.1 as control inputs, fusing the simulated measurements obtained by the sensors. On the other hand, the double integrator model requires linear and angular accelerations as control inputs, which typically can be deduced from measurements employing on-board sensors. These accelerations are also simulated based on the reference model, by transforming the linear and angular acceleration from the body reference frame to the inertial reference frame, and adding white Gaussian noise with standard deviations of $0.12\,\mathrm{m/s^2}$ and $2\,\mathrm{deg/s^2}$ respectively, according to experimental data.

All the code developed for this implementation is openly available [Garcia-Huerta-20a]. This comprehends the complete estimation scheme, including the implementation of the 6-DOF nonlinear equations of motion (reference model), the linearized equation of motions, and the Kalman filter.

6.1. Simulation Results

Two separate implementations of the described discrete Kalman filter scheme were performed: one using the linearized model and brake deflections as control inputs, and another using the double integrator model and the simulated accelerations as control inputs. Both implementations were performed using the same initial conditions and simulated measurements.

The Kalman filter estimates based on the proposed linearized model ($\widehat{\mathbf{x}}^{Li}$) and the double integrator model ($\widehat{\mathbf{x}}^{D}$) are presented in Fig. 6.3–6.6, together with the reference model ($\mathbf{x}^{R}$) for

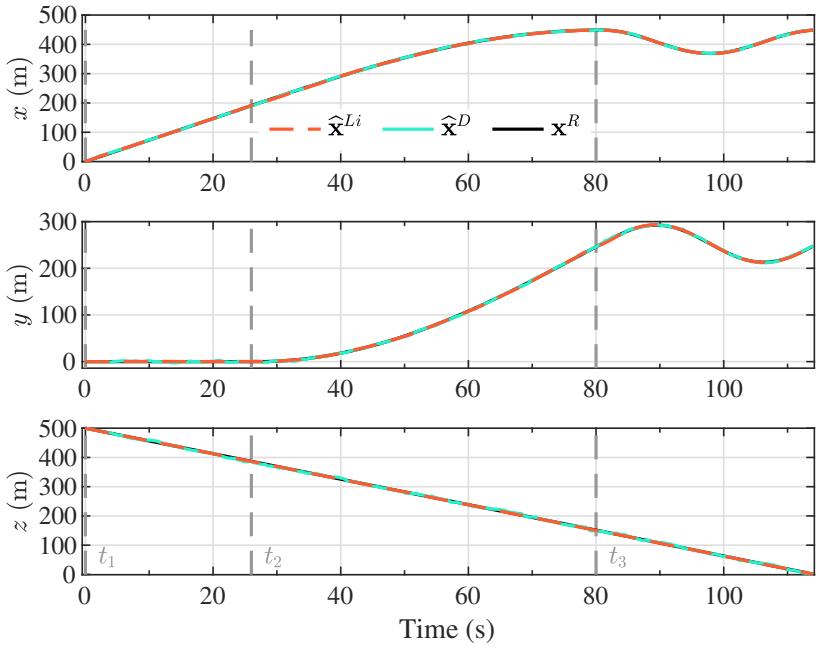

Fig. 6.3. Kalman filter inertial position estimates based on the proposed linearized model ($\widehat{\mathbf{x}}^{Li}$) and the double integrator model ($\widehat{\mathbf{x}}^{D}$), together with the components of the inertial position vector from the reference model ($\mathbf{x}^{R}$).

comparison purposes. The different maneuver segments are presented in all figures with vertical dashed lines at the time of execution, with the maneuver identifier displayed at the bottom to facilitate the interpretation.

From Fig. 6.3, it can be observed that the Kalman filtering scheme based on each of the proposed models was capable of reproducing the components of the inertial position of the vehicle, for any of the flight scenarios corresponding to the maneuver segments. Due to the smooth evolution of each of the components of the inertial position, both the linearized model and the double integrator model were suitable for emulating the behavior of the position of the nonlinear reference model. This mild progression of the inertial position of the PADS closely represented a real flight scenario. From the beginning of the descent trajectory, after the full inflation of the canopy and stabilization of the gliding flight, the only external perturbation experienced by the parafoil-payload system originated from the wind. While strong wind profiles could substantially affect the flight dynamics of small vehicles, a fuselage designed to reduce drag could be employed to mitigate this effect. Additionally, the heavier the payload, the less prone it is to suffer abrupt changes in position due to its inertia.

The components of the linear velocity, presented in Fig. 6.5, demonstrate that the lateral compo-

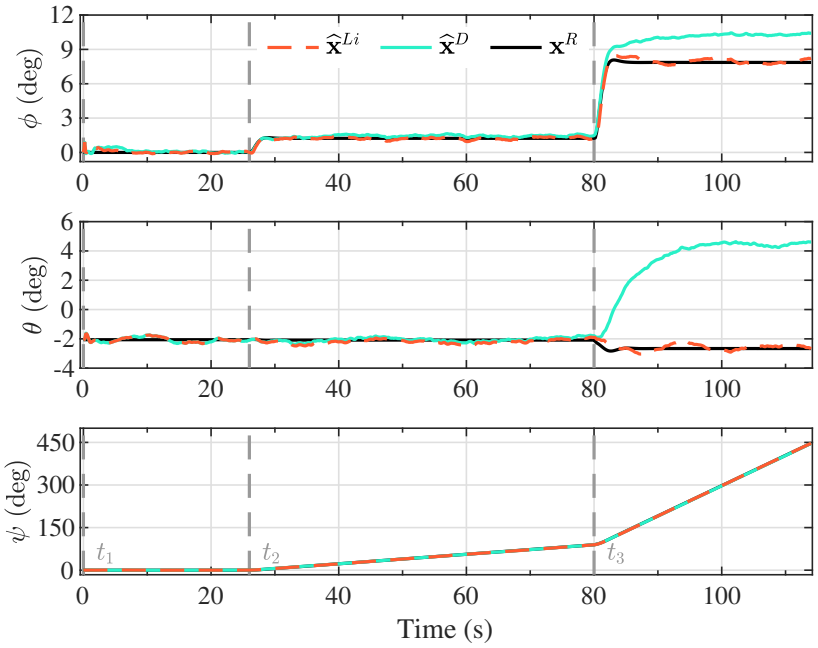

Fig. 6.4. Kalman filter angular position estimates based on the proposed linearized model ($\widehat{\mathbf{x}}^{Li}$) and the double integrator model ($\widehat{\mathbf{x}}^{D}$), together with the components of the angular position vector from the reference model ($\mathbf{x}^{R}$). These components are expressed in the inertial reference frame, corresponding to the Euler orientation angles roll, pitch, and yaw, respectively.

nent of the velocity (v) was virtually zero along the complete descent trajectory. This reflects the fact that there were no perturbations that modify the lateral movement of the vehicle aside from the control inputs, and that the flight was dominated by its longitudinal dynamics. In the three linear velocity components, it was distinctly recognizable that the estimations based on the double integrator model strongly varied around the reference model, in comparison with the estimates from the linearized model. While the bounded variation confirmed that the Kalman filter estimation scheme converged towards the reference model, it was an indication that the Kalman gain was favoring the measurements instead of the model.

Note that along the descent trajectory, the deflection brakes applied on each maneuver were held constant until the next maneuver was reached, or the vehicle landed. Furthermore, the maneuvers were applied instantaneously, as step functions. This means that the delayed response of the actuators, and the elasticity of the lines used to apply the deflection brakes were not taken into account, which would modify the transient response of the state variables. Despite the condition analyzed in this investigation where the brake deflections were applied infinitely fast, the estimation process based on the proposed linearized model was able to follow the dynamics of the reference model,

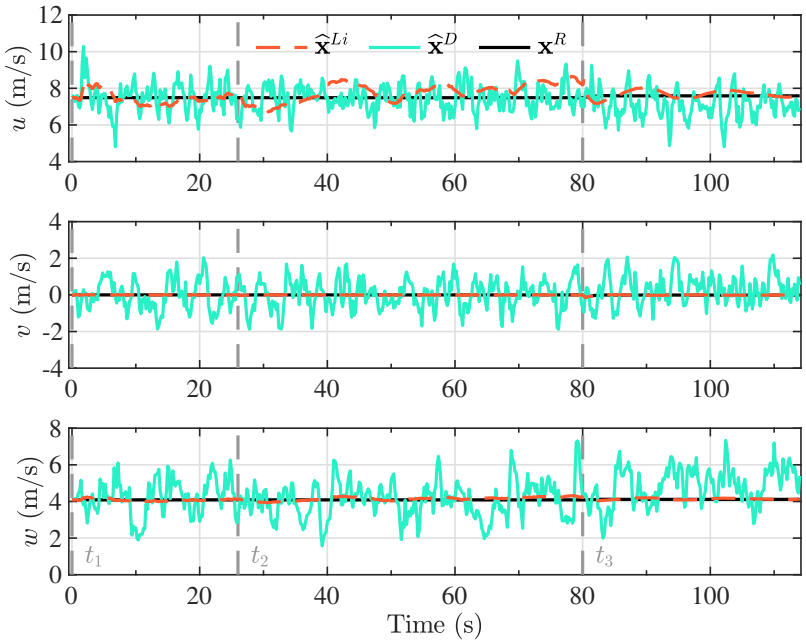

Fig. 6.5. Kalman filter linear velocity estimates based on the proposed linearized model $(\widehat{\mathbf{x}}^{Li})$ and the double integrator model $(\widehat{\mathbf{x}}^{D})$, together with the components of the linear velocity vector from the reference model $(\mathbf{x}^{R})$. These components are expressed in the body reference frame.

suggesting that for smoother executions of the maneuvers, the performance only could improve. In real applications, the maneuvers cannot be applied instantaneously, but gradually, leading to a smoother response on the state variables. The consequence of this abrupt change in the maneuver segments can be observed, for example, in the angular velocity components (p, q, r) in Fig. 6.6, especially when the last maneuver (t_3) is applied.

While Fig. 6.3–6.6 provide valuable information about the 12 components of the state vector estimated by virtue of the proposed Kalman filter scheme, it is difficult to appreciate the shape and magnitude of the error with respect to the reference model. The error was computed as the difference between the reference model $\mathbf{x}^{R}$ and the Kalman filter state estimates based on the linearized model $\widehat{\mathbf{x}}^{Li}$ and the double integrator model $\widehat{\mathbf{x}}^{D}$, respectively. This error is denoted as $\overline{\mathbf{x}}^{Li}$ and $\overline{\mathbf{x}}^{D}$ for each implementation.

To obtain a better understanding of how closely the estimation scheme followed the reference model for the inertial position, the error in the magnitude of the position vector obtained with the reference model and the magnitude of the Kalman filter position vector estimates are presented in Fig. 6.7, denoted as $\|\overline{\boldsymbol{p}}\|$. It can be appreciated that both models were capable of representing the

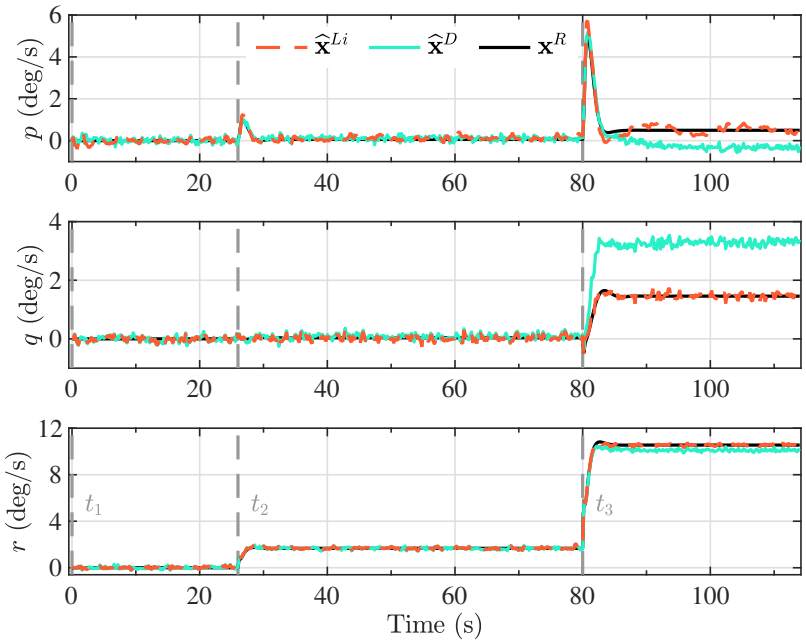

Fig. 6.6. Kalman filter angular velocity estimates based on the proposed linearized model ($\widehat{\mathbf{x}}^{Li}$) and the double integrator model ($\widehat{\mathbf{x}}^{D}$), together with the components of the angular velocity vector from the reference model ($\mathbf{x}^{R}$). These components are expressed in the body reference frame.

tridimensional position of the vehicle during the different flight segments since in general, the error oscillated around zero. In contrast, the filter estimates based on the linearized model presented a smoother variation, with an error magnitude approximately two times smaller.

To evaluate the performance in estimating the attitude of the PADS, Fig. 6.8 presents the error between the Euler angles of the reference model and the Kalman filter estimates using each of the proposed models. Notice that during the first and second maneuver segments (t_1 and t_2), corresponding to a straight flight and a wide turn, the two models captured the same behavior as the reference model. Nevertheless, the double integrator model presented a larger and consistent error for roll (ϕ) and pitch (θ) angles, and a smaller but still noticeable constant error for the yaw angle (ψ), after the third maneuver was applied (t_3), where the flight trajectory with a narrower turn was followed. This is a consequence of the higher rate of change in the angular position that the vehicle experienced during the last flight segment, where a -0.4 right brake deflection was being applied. The double integrator model relied on the assumption that the parafoil-payload system experienced epoch-wise constant inertial acceleration during the integration period. Consequently, the higher the body-fixed angular velocity, the less this assumption was fulfilled, as can be verified from the

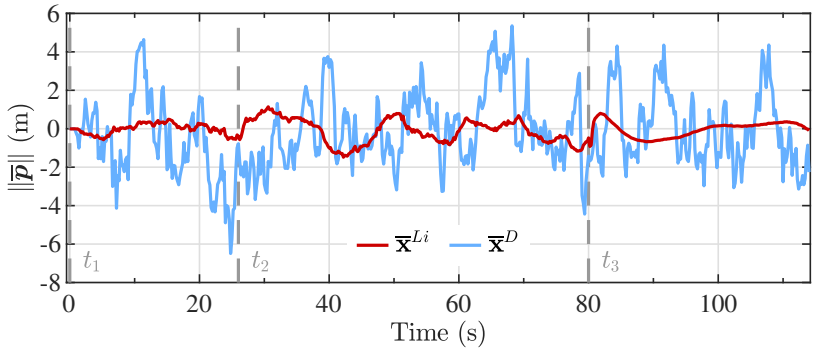

Fig. 6.7. Error in the magnitude of the inertial position vector between the reference model and the Kalman filter estimates from the linearized model ($\overline{\mathbf{x}}^{Li}$) and the double integrator model ($\overline{\mathbf{x}}^{D}$).

error in the angular velocity components presented in Fig. 6.9.

The achievable turn rate for any PADS has a practical limit, since a steep turn rate could induce spiral divergence. For a vehicle with similar characteristics as the simulated in this study, Ward et al. [Ward-11; Ward-14] report maximum turn rates from $15\,\mathrm{deg/s}$ up to $25\,\mathrm{deg/s}$, depending on the flight mode and control scheme. For the case of larger parafoil-payload vehicles, Lingard reports a maximum constant turn rate of $11.5\,\mathrm{deg/s}$ for a canopy with $30\,\mathrm{m}$ of wingspan [Lingard-95].

6.1.1 Sampling rate analysis

The selected $5\,\mathrm{Hz}$ sampling rate for the analysis of the proposed estimation scheme, as mentioned in Section 4.1, was chosen according to the processing capabilities of typical low-end microprocessors and suitable sensors. To evaluate the impact that the sampling rate has on the performance of the overall state estimation process, the previously presented implementation procedure was repeated varying the sampling rate from $0.5\,\mathrm{Hz}$ up to $5\,\mathrm{Hz}$, with sampling period increments of $0.1\,\mathrm{s}$.

For each iteration, the errors $\overline{\mathbf{x}}^{Li}$ and $\overline{\mathbf{x}}^{D}$ were calculated, together with the corresponding standard deviations of the errors $\overline{\boldsymbol{\sigma}}^{Li}$ and $\overline{\boldsymbol{\sigma}}^{D}$. This represents the calculation of one standard deviation per model (Li and D), for each state variable, per sampling rate analyzed (19 in total). To obtain comparable results between state variables, the standard deviations are normalized by dividing by the taxicab norm as:

$$\Gamma_n = \frac{\overline{\sigma}_n}{\sum_n |\overline{\sigma}_n|} \tag{6.1}$$

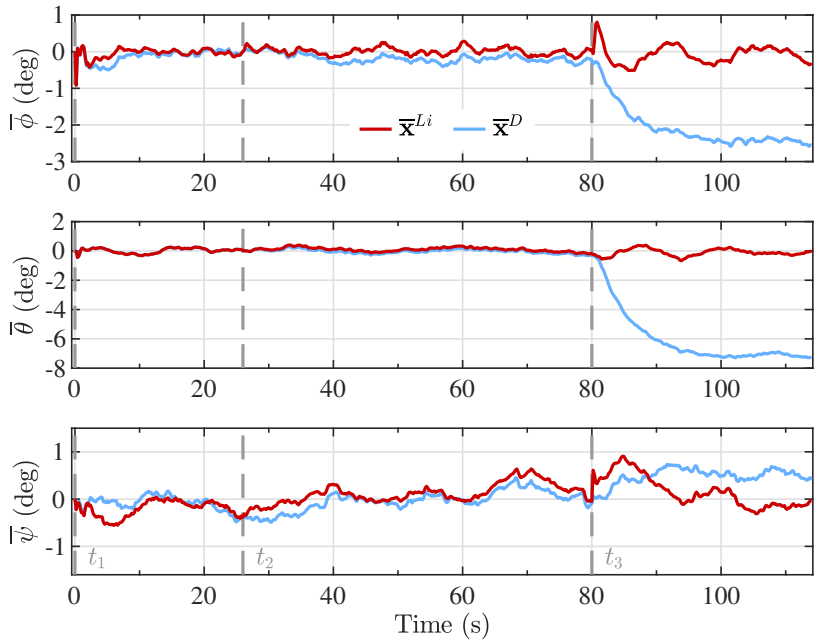

Fig. 6.8. Error in the inertial angular position components between the reference model and the Kalman filter estimates from the linearized model ($\overline{\mathbf{x}}^{Li}$) and the double integrator model ($\overline{\mathbf{x}}^{D}$).

where Γ_n correspond to the normalized standard deviation of the error for each state variable per sampling rate. The numerator $\overline{\sigma}_n$ corresponds to the standard deviation of the *n*th frequency per state variable. Finally, the denominator represents the taxicab norm ($\mathcal{L}_1$ norm) per state variable, determined as the sum of standard deviations across all the frequencies.

Fig. 6.10 presents the normalized standard deviations for each of the linear models (Γ_n^{Li} and Γ_n^{D}), per sampling rate. Any vertical column is the result of stacking the 12 normalized standard deviations for each implementation. A relevant property of the normalization in (6.1) is that the sum of all normalized standard deviation per state variable equals to 1, i.e., the sum of all elements of same color (same state variable) across all frequencies, per linear model, equals to 1 (dimensionless), making the deviations for all the variables comparable according to its size.

In general, the cumulative (stacked) normalized standard deviation from the estimation scheme based on both, the linearized model (Li) and the double integrator model (D), is observed to grow as the sampling rate decreases. This implies that the higher the sampling rate, the less dispersion is present in the state estimates.

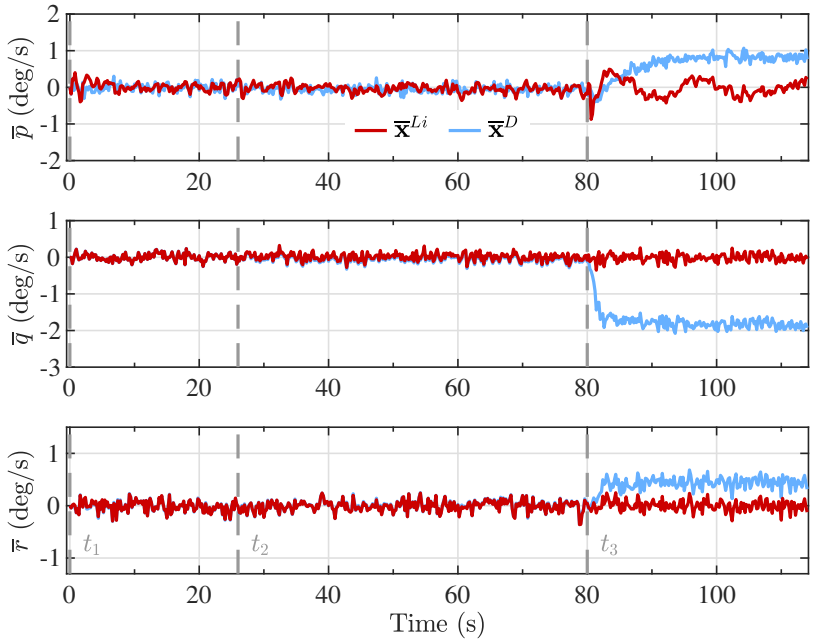

Fig. 6.9. Error in the angular velocity components, expressed in the body reference frame, between the reference model and the Kalman filter estimates from the linearized model ($\overline{\mathbf{x}}^{Li}$) and the double integrator model ($\overline{\mathbf{x}}^{D}$).

6.2. Discussion

It is relevant to highlight some properties and prerequisites for the operation and deduction of the linearized model and the double integrator model. The linearized model requires the calculation of the Jacobian matrices, increasing the complexity of its deduction depending on the forces and moments representing the interaction between the vehicle and its surroundings. This requires the characterization of the parafoil-payload system, limiting the flexibility of this model to be applied in any other vehicle with different properties. Moreover, the stable points need to be computed prior to the descent trajectory. While this demands additional effort, it is important to note that this task is performed on the ground, where typically more computational resources are available, without increasing the real-time computational burden during the flight. Since the flight conditions variate from flight to flight, it is required to calculate a set of stable points assuming the planned maneuvers to reach the target. If the computed stable points differ greatly from the actual conditions during flight, the performance would deteriorate.

In contrast, the double integrator model does not depend on the physical properties of the parafoil-payload system, simplifying the implementation of this model on vehicles with different

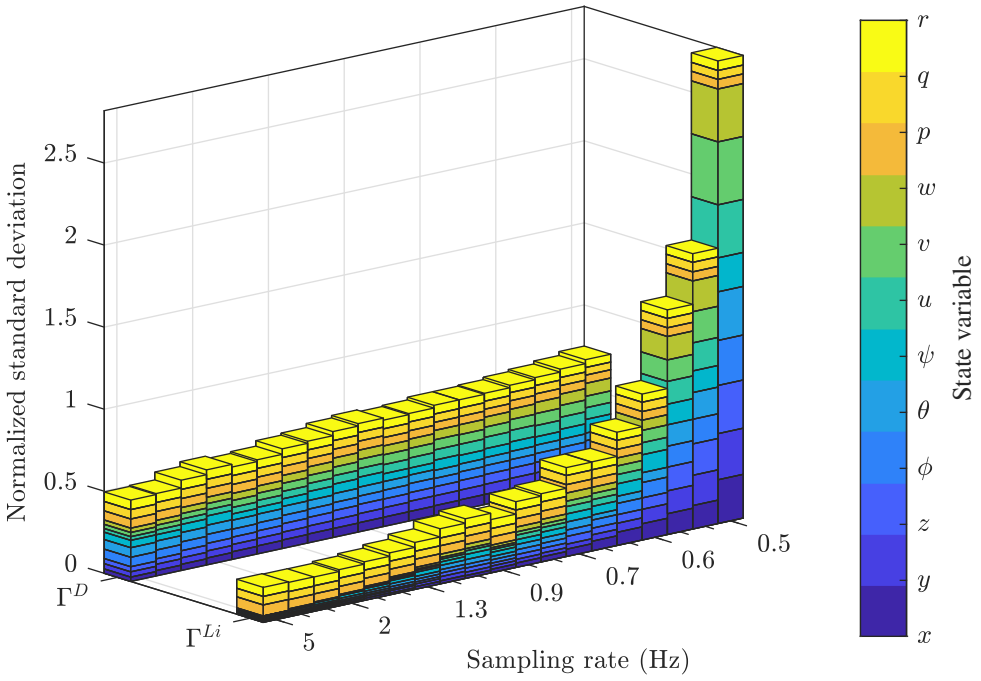

Fig. 6.10. Normalized standard deviation of the errors between the reference model and the Kalman filter estimates from both linear models, for implementations of the estimation scheme utilizing different sampling rates.

characteristics. As a consequence, this model does not directly relate the brake deflections to the state variables, making it not suitable for a straightforward application of a control scheme for guidance. While the implementation of this model is much simpler than the linearized model, without requiring the computation of the stable points or other parameters before the flight, it heavily depends on the sampling rate and quality of the measurements provided by the sensors.

The selected $5\,\mathrm{Hz}$ sampling rate for the measurements is a conservative choice that complies with the capacities of any relatively modern low-cost processing unit and sensors for real-time applications. The higher the capabilities of the sensors and the processing unit, the larger the achievable sampling rate during flight. This might be desirable when fast maneuvers are required or strong wind profiles modify the trajectory of the vehicle, although this implies higher costs associated with instrumentation, energy storage, and a heavier payload, sometimes not feasible for micro-lightweight PADSs.

In the case that exogenous forces are present during the flight as a consequence of strong winds, which are not incorporated into the flight dynamic models as the external wind vector $\boldsymbol{\lambda}$, it is expected that the predictions provided by the models would deteriorate. Another source of perturbations

could be the effect of mismodeled interactions in the parafoil-payload system, due to the relative motion of its components. Nevertheless, the overall performance of the proposed estimation scheme would not be necessarily deteriorated proportionally to the magnitude of the perturbations, since the Kalman gain would favor the measurements from the sensors or the predictions of the dynamic models, attempting to compensate for these effects by minimizing the a posteriori error covariance.

6.3. Conclusion

Throughout this chapter, two models that represent the flight dynamics of micro-lightweight PADSs were developed: a linearized version of a 6-DOF nonlinear model and a double integrator model. Additionally, simulated measurements representative of sensors onboard the vehicle were fused by implementing a Kalman filter algorithm based on the developed models, to estimate the position and attitude of the parafoil-payload system.

The simulation results demonstrate that both models capture the flight dynamics of micro-lightweight PADSs when incorporated into a Kalman filtering scheme for smooth flights. While the double integrator model excels in simplicity, and it is independent of the physical properties of the parafoil-payload system, it falls behind in precision capturing the flight dynamics, especially when the vehicle is subject to intense accelerations. On the other hand, the linearized model is capable of representing the flight dynamics of the vehicle more accurately and preserves precision even during narrow maneuvers, but depends on the determination of stable points close to the operation point of the vehicle. The performance of the proposed estimation scheme, when the control inputs and flight dynamics deviate from the computed stable points of the linearized model, is to be assessed in a follow-on research.

Further investigation is required on the inclusion of the proposed estimation scheme into a global closed-loop control strategy for the vehicle. In particular, tracking of constant waypoints is usually a control objective for this type of system. The utilization of the obtained linearized model could be a solid starting point for the development of a model-based robust controller. The design of a suitable control strategy, that includes the proposed estimation scheme, and its stability analysis is left as future work.

General Conclusions

This doctoral dissertation presented the development and implementation of an estimation scheme, based on a Kalman filter, for the determination of the navigation states of vehicles, fusing measurements from low-cost sensors.

The use of a low-cost GPS receiver, together with high-resolution aerial images, allowed to estimate the accuracy of the positioning solution provided by the receiver, based on recognizable landmarks in the aerial images and changes in the direction of motion of a pedestrian user. While the methodology proposed proved to be effective for the positioning accuracy determination, it relies on a carefully designed and well-known navigation trajectory in order to ensure a submeter accuracy as true position.

The addition of supplementary information regarding identifiable landmarks in an aerial image, incorporated into a Kalman filter as measurements with low uncertainty in an error state-space formulation, proved to be an effective approach for enhancing the trajectory estimation process for low-cost pedestrian applications. The applicability of this methodology on vehicles with different navigation dynamics needs to be further investigated.

The proposed state estimation scheme was implemented for the determination of the position and attitude of micro-lightweight Precision Aerial Delivery Systems (PADSs). For this, a 6-DOF nonlinear model was implemented and adopted as reference. In addition, two models that represent the flight dynamics of micro-lightweight PADSs were developed: a linearized version of a 6-DOF nonlinear model and a double integrator model, both suitable for the proposed sensor fusion algorithm as part of the state estimation scheme.

The implementation of the state estimation scheme proved to be effective in the determination of the position and attitude of PADSs, when incorporating the linear models representing the flight dynamics of the parafoil-payload system, with measurements from low-cost sensors. The use of linear models for the state propagation, allows for the implementation of a total state-space formulation of a discrete Kalman filter, demonstrating its adequacy for low-cost applications with limited computational resources.

The analysis and inclusion of exogenous forces in the equations of motions of PADSs is to be investigated. Furthermore, the incorporation of the state estimation scheme into a suitable robust control strategy is left as future work.

Conclusiones Generales

En este trabajo de tesis doctoral se presentó el desarrollo e implementación de un esquema de estimación basado en un filtro de Kalman, para la determinación de los estados de navegación de vehículos, fusionando mediciones provenientes de sensores de bajo costo.

El uso de receptores de GPS de bajo costo, junto con imágenes aéreas de alta calidad, permitió estimar la exactitud de la solución de posicionamiento provista por el receptor, basado en puntos de referencia reconocibles en las imágenes aéreas, así como cambios en la dirección de movimiento de usuarios pedestres. Si bien la metodología propuesta probó ser efectiva para la determinación de la exactitud del posicionamiento, esta depende de una trayectoria de navegación bien conocida y diseñada para asegurar obtener una exactitud en un orden de magnitud menor a los metros como posición verdadera.

La integración de información suplementaria respecto a puntos de referencia reconocibles en imágenes aéreas, incorporada dentro del filtro de Kalman como mediciones con baja incertidumbre en una formulación de error de espacio de estados, demostró ser una propuesta efectiva como método de mejora de la estimación de la trayectoria de navegación para aplicaciones pedestres de bajo costo. La aplicabilidad de esta metodología en vehículos con dinámicas de movimiento diferentes, debe de ser investigada más a fondo.

El esquema de estimación de estados se implementó para la determinación de la posición y orientación de un sistema de entrega aérea de precisión (PADS, por sus siglas en inglés). Para esto, un modelo no lineal de seis grados de libertad se implementó y adoptó como referencia. Adicionalmente, se desarrollaron dos modelos lineales que representan la dinámica de vuelo de PADSs micro ligeros: una versión linealizada del modelo de seis grados de libertad, así como un modelo basado en un doble integrador, ambos pertinentes para el algoritmo de fusión de sensores propuesto como parte del esquema de estimación de estados.

La implementación del esquema de estimación de estados demostró ser efectiva en la determinación de la posición y orientación de PADSs, al incorporar modelos lineales representativos de la dinámica de vuelo del sistema campana-carga útil, con mediciones de sensores de bajo costo.

El uso de modelos lineales para la propagación de estados, permite la implementación de un filtro de Kalman discreto en su formulación total de espacio de estados, demostrando su idoneidad para aplicaciones de bajo costo con recursos computacionales limitados.

Como trabajo futuro, es de interés el análisis e incorporación de fuerzas exógenas en las ecuaciones de movimiento de PADSs. También, la inclusión del esquema de estimación de estados en una estrategia de control robusta se deja como posible trabajo futuro.

Appendix

A. List of Internal Research Reports

1) R. A. Garcia-Huerta, I. E. Villalon-Turrubiates, and L. E. González-Jiménez, "A study on modeling the flight path of weather balloons," Internal Report *PhDEngScITESO-16-18-R*, ITESO, Tlaquepaque, Mexico, Dec. 2016.

2) R. A. Garcia-Huerta, I. E. Villalon-Turrubiates, and L. E. González-Jiménez, "Implementation of a Kalman filter for UAV tracking," Internal Report *PhDEngScITESO-17-15-R*, ITESO, Tlaquepaque, Mexico, May 2017.

3) R. A. Garcia-Huerta, I. E. Villalon-Turrubiates, and L. E. González-Jiménez, "Review on the modeling and validation of precision aerial delivery systems," Internal Report *PhDEngScITESO-17-58-R*, ITESO, Tlaquepaque, Mexico, Dec 2017.

4) R. A. Garcia-Huerta, I. E. Villalon-Turrubiates, L. E. González-Jiménez, and G. Allende-Alba "Accuracy estimation of a low-cost GPS receiver using landmarks on aerial images," Internal Report *PhDEngScITESO-18-13-R*, ITESO, Tlaquepaque, Mexico, May 2018.

5) R. A. Garcia-Huerta, I. E. Villalon-Turrubiates, L. E. González-Jiménez, and G. Allende-Alba "Kalman filter-based trajectory estimation using a low-cost sensor and aerial images," Internal Report *PhDEngScITESO-18-47-R*, ITESO, Tlaquepaque, Mexico, Dec. 2018.

6) R. A. Garcia-Huerta, I. E. Villalon-Turrubiates, and L. E. González-Jiménez "Review on the application, classification, and modeling of precision aerial delivery systems," Internal Report *PhDEngScITESO-18-58-R*, ITESO, Tlaquepaque, Mexico, Dec. 2018.

7) R. A. Garcia-Huerta, I. E. Villalon-Turrubiates, and L. E. González-Jiménez "State estimation scheme for precision aerial delivery systems," Internal Report *PhDEngScITESO-19-40-R*, ITESO, Tlaquepaque, Mexico, Dec. 2019.

8) R. A. Garcia-Huerta, I. E. Villalon-Turrubiates, and L. E. González-Jiménez "A 6-DOF dynamics model for micro-lightweight parafoil-payload systems," Internal Report *PhDEngScITESO-19-41-R*, ITESO, Tlaquepaque, Mexico, Dec. 2019.

9) R. A. Garcia-Huerta, I. E. Villalon-Turrubiates, and L. E. González-Jiménez "State-space representation of a 6-DOF dynamics model for parafoil-payload systems," Internal Report *PhDEngScITESO-19-43-R*, ITESO, Tlaquepaque, Mexico, Dec. 2019.

10) R. A. Garcia-Huerta, I. E. Villalon-Turrubiates, and L. E. González-Jiménez "Linearization of a 6-DOF dynamics model for PADS," Internal Report *PhDEngScITESO-20-12-R*, ITESO, Tlaquepaque, Mexico, Aug. 2020.

11) R. A. Garcia-Huerta, I. E. Villalon-Turrubiates, and L. E. González-Jiménez "A double integrator dynamic model for PADS," Internal Report *PhDEngScITESO-20-14-R*, ITESO, Tlaquepaque, Mexico, Aug. 2020.

12) R. A. Garcia-Huerta, I. E. Villalon-Turrubiates, and L. E. González-Jiménez "Estimation scheme for position and attitude of PADS," Internal Report *PhDEngScITESO-20-16-R*, ITESO, Tlaquepaque, Mexico, Aug. 2020.

13) R. A. Garcia-Huerta, I. E. Villalon-Turrubiates, and L. E. González-Jiménez “Error analysis of the state estimation scheme of PADS,” Internal Report *PhDEngScITESO-20-18-R*, ITESO, Tlaquepaque, Mexico, Aug. 2020.

B. List of Publications

B.1 Conference Papers

1) R. A. Garcia-Huerta, I. E. Villalon-Turrubiates, L. E. González-Jiménez and G. Allende-Alba, "Accuracy estimation of a low-cost GPS receiver using landmarks on aerial images," IGARSS 2019 – 2019 IEEE International Geoscience and Remote Sensing Symposium, Yokohama, Japan, 2019, pp. 9244–9247, DOI: 10.1109/IGARSS.2019.8899767.

2) R. A. Garcia-Huerta, I. E. Villalon-Turrubiates, L. E. González-Jiménez and G. Allende-Alba, "Kalman filter-based trajectory estimation using a low-cost sensor and aerial images," IGARSS 2020 – 2020 IEEE International Geoscience and Remote Sensing Symposium, Waikoloa, Hawaii, 2020, pp. 6400–6403.

B.2 Journal Papers

1) R. A. Garcia-Huerta, L. E. González-Jiménez, and I. E. Villalon-Turrubiates, "Sensor fusion algorithm using a model-based Kalman filter for the position and attitude estimation of precision aerial delivery systems," Sensors, vol. 20, no. 18, p. 5227, Sep. 2020, DOI: 10.3390/s20185227.

C. Coefficients of the Linearized Flight Dynamic Model of Precision Aerial Delivery System

In the following, the components of matrices A and B, and vector $\boldsymbol{\varepsilon}$, are presented, corresponding to each of the maneuver segments for the linearized model. These values are obtained by evaluating the forces, moments, and Jacobian matrices at the stable points reported in Table 6.2 for the state variables $\mathbf{x}_s$, and the brake deflections reported in Table 6.1 as control inputs $\mathbf{u}_s$. Consequently, their values remain constant throughout each of the control segments. The only elements that are not constant are the components of the force vector caused by the weight of the parafoil-payload system ($\boldsymbol{F}_W$), which depend on the instant attitude and need to be calculated epoch-wise. Recalling:

$$A = [GM]^{-1}\,[J^{\mathbf{x}}] \tag{5.171 revisited}$$

$$B = [GM]^{-1}\,[J^{\mathbf{u}}] \tag{5.172 revisited}$$

$$\boldsymbol{\varepsilon} = [GM]^{-1}\left(\begin{pmatrix}\boldsymbol{F}_s\\ \boldsymbol{M}_s\end{pmatrix} - J^{\mathbf{x}}\mathbf{x}_s - J^{\mathbf{u}}\mathbf{u}_s\right). \tag{5.173 revisited}$$

The matrix GM incorporates information regarding the geometry, mass, and inertia of the parafoil-payload system (5.44). These attributes are fixed, since the vehicle is considered a rigid body, and therefore this matrix remains constant throughout the descent trajectory:

$$[GM]^{-1} = \begin{bmatrix} 0.42 & 0 & 0 & 0 & 0.02 & 0 \\ 0 & 0.41 & 0 & -0.1 & 0 & 0.05 \\ 0 & 0 & 0.33 & 0 & 0 & 0 \\ 0 & -0.1 & 0 & 1.76 & 0 & -0.89 \\ 0.02 & 0 & 0 & 0 & 2.28 & 0 \\ 0 & 0.05 & 0 & -0.89 & 0 & 17.43 \end{bmatrix}$$

Maneuver segment 1:

$$A = \begin{bmatrix} -0.97 & 0 & 1.61 & 0 & -2.99 & 0 \\ 0 & -1.09 & 0 & 3.19 & 0 & -7.14 \\ 0.54 & 0 & -4.76 & 0 & 5.24 & 0 \\ 0 & -4.23 & 0 & -5.18 & 0 & 2.34 \\ 6.11 & 0 & -11.2 & 0 & -7.32 & 0 \\ 0 & 8.74 & 0 & 7.26 & 0 & -6.68 \end{bmatrix}$$

$$B = \begin{bmatrix} -0.047 & -0.047 \\ 0.01 & -0.01 \\ -0.021 & -0.021 \\ -0.174 & 0.174 \\ 0.193 & 0.193 \\ 1.683 & -1.683 \end{bmatrix}$$

$$\boldsymbol{\varepsilon} = [GM]^{-1} \begin{pmatrix} F_{Wx} \\ F_{Wy} \\ F_{Wz} \\ 0 \\ 0 \\ 0 \end{pmatrix} + \begin{pmatrix} 0.35 \\ 0 \\ 7.721 \\ 0 \\ 0.018 \\ 0 \end{pmatrix}$$

Maneuver segment 2:

$$A = \begin{bmatrix} -0.97 & 0.03 & 1.61 & 0 & -2.99 & 0 \\ -0.03 & -1.1 & 0 & 3.19 & 0 & -7.14 \\ 0.54 & 0 & -4.76 & 0 & 5.23 & 0 \\ 0.01 & -4.24 & -0.01 & -5.19 & 0.01 & 2.35 \\ 6.11 & -0.01 & -11.19 & -0.04 & -7.32 & 0 \\ 0.01 & 8.75 & 0.02 & 7.28 & 0 & -6.72 \end{bmatrix}$$

$$B = \begin{bmatrix} -0.052 & -0.048 \\ 0.011 & -0.01 \\ -0.023 & -0.021 \\ -0.19 & 0.175 \\ 0.21 & 0.194 \\ 1.838 & -1.693 \end{bmatrix}$$

$$\varepsilon = [GM]^{-1} \begin{pmatrix} F_{Wx} \\ F_{Wy} \\ F_{Wz} \\ 0 \\ 0 \\ 0 \end{pmatrix} + \begin{pmatrix} 0.359 \\ 0.201 \\ 7.721 \\ -0.031 \\ -0.003 \\ -0.158 \end{pmatrix}$$

Maneuver segment 3:

$$A = \begin{bmatrix} -0.98 & 0.21 & 1.6 & 0.02 & -3.02 & -0.02 \\ -0.17 & -1.1 & 0 & 3.21 & -0.01 & -7.24 \\ 0.57 & 0 & -4.79 & 0.01 & 5.31 & 0 \\ 0.06 & -4.24 & -0.06 & -5.18 & 0.08 & 2.36 \\ 6.13 & -0.09 & -11.27 & -0.25 & -7.35 & 0 \\ 0.05 & 8.72 & 0.13 & 7.19 & 0.02 & -6.51 \end{bmatrix}$$

$$B = \begin{bmatrix} -0.047 & -0.13 \\ 0.01 & -0.026 \\ -0.021 & -0.057 \\ -0.17 & 0.48 \\ 0.188 & 0.532 \\ 1.645 & -4.65 \end{bmatrix}$$

$$\boldsymbol{\varepsilon} = [GM]^{-1} \begin{pmatrix} F_{Wx} \\ F_{Wy} \\ F_{Wz} \\ 0 \\ 0 \\ 0 \end{pmatrix} + \begin{pmatrix} 0.4 \\ 1.279 \\ 7.622 \\ -0.128 \\ 0.235 \\ -1.698 \end{pmatrix}$$

Bibliography

[Abdi-12] E. Abdi, S. R. Sisakht, L. Goushbor, and H. Soufi. "Accuracy assessment of GPS and surveying technique in forest road mapping". In: *Ann. of Forest Res.* 55.2 (July 2012), pp. 309–317–317. ISSN: 20652445. DOI: 10.15287/afr.2012.68.

[Ackerman-19] E. Ackerman and M. Koziol. "In the air with zipline's medical delivery drones". In: *IEEE Spectr.* 56.5 (2019). URL: https://spectrum.ieee.org/robotics/drones/in-the-air-with-ziplines-medical-delivery-drones.

[Ackerman-20] E. Ackerman. "Zipline wants to bring medical drone delivery to U.S. to fight COVID-19". In: *IEEE Spectr.: Technol., Eng., and Sci. News* (Apr. 2020). URL: https://spectrum.ieee.org/automaton/robotics/drones/zipline-medical-drone-delivery-covid19.

[Adjrad-17] M. Adjrad and P. D. Groves. "Enhancing least squares GNSS positioning with 3D mapping without accurate prior knowledge". In: *Navigation* 64.1 (May 2017), pp. 75–91. DOI: 10.1002/navi.178.

[Atmel-18] Atmel. *ATmega328 data sheet*. Available online: http://ww1.microchip.com/downloads/en/DeviceDoc/ATmega48A-PA-88A-PA-168A-PA-328-P-DS-DS40002061A.pdf. (accessed on 30 July 2020). 2018.

[Benassi-17] F. Benassi et al. "Testing accuracy and repeatability of UAV blocks oriented with GNSS-supported aerial triangulation". In: *Remote Sensing* 9.2 (Feb. 2017), pp. 1–23. DOI: 10.3390/rs9020172.

[Benney-07] R. Benney, J. McGrath, J. McHugh, G. Noetscher, S. Tavan, and S. Patel. "DOD JPADS programs overview and NATO activities". In: *19th AIAA Aerodynamic Decelerator Syst. Technol. Conf. and Seminar*. Williamsburg, VA, USA, May 2007, pp. 1–16. DOI: 10.2514/6.2007-2576.

[Benney-09] R. Benney, M. Henry, K. Lafond, A. Meloni, and S. Patel. "DOD new JPADS programs and NATO activities". In: *20th AIAA Aerodynamic Decelerator Syst. Technol. Conf. and Seminar*. Seattle, WA, USA, May 2009, pp. 1–18. DOI: 10.2514/6.2009-2952.

[Broadcom-20] Broadcom. *BCM2711 data sheet*. Available online: https://www.raspberrypi.org/documentation/hardware/raspberrypi/bcm2711/rpi_DATA_2711_1p0.pdf. (accessed on 30 July 2020). Feb. 2020.

[Brown-99] G. Brown, R. Haggard, R. Almassy, R. Benney, and S. Dellicker. "The affordable guided airdrop system (AGAS)". In: *15th Aerodynamic Decelerator Syst. Technol. Conf.* Toulouse, France, June 1999, pp. 1–10. DOI: 10.2514/6.1999-1742.

[Cacan-15] M. R. Cacan, E. Scheuermann, M. Ward, M. Costello, and N. Slegers. "Autonomous airdrop systems employing ground wind measurements for improved landing accuracy". In: *IEEE/ASME Transactions on Mechatronics* 20.6 (Dec. 2015), pp. 3060–3070. DOI: 10.1109/TMECH.2015.2405851.

[Cockrell-91] D. Cockrell. "Apparent mass - Its history and its engineering legacy for parachute aerodynamics". In: *11th Aerodynamic Decelerator Syst. Technol. Conf.* San Diego, CA, USA, Apr. 1991, pp. 1–10. DOI: 10.2514/6.1991-827.

[Crassidis-11] J. L. Crassidis and J. L. Junkins. *Optimal Estimation of Dynamic Systems*. 2nd ed. London, U.K.: Chapman & Hall, Oct. 2011. Chap. 3, pp. 149–151. ISBN: 978-1-4398-3985-0.

[Dabberdt-15] W. F. Dabberdt and H. Turtiainen. "Observation Platforms | Radiosondes". In: *Encyclopedia of Atmospheric Sciences*. 2nd ed. Vol. 4. Oxford: Academic Press, 2015, pp. 273–284. DOI: 10.1016/B978-0-12-382225-3.00344-3.

[Farhangian-20] F. Farhangian and R. Landry. "Accuracy improvement of attitude determination systems using EKF-based error prediction filter and PI controller". In: *Sensors* 20.14 (July 2020), pp. 1–16. DOI: 10.3390/s20144055.

[Garcia-Huerta-20a] R. A. Garcia-Huerta. *Code repository for: Sensor fusion algorithm using a model-based Kalman filter for the position and attitude estimation of precision aerial delivery systems*. Version 1.0. Sept. 2020. DOI: 10.5281/zenodo.3978828.

[Garcia-Huerta-20b] R. A. Garcia-Huerta, L. E. González-Jiménez, and I. E. Villalon-Turrubiates. "Sensor fusion algorithm using a model-based Kalman filter for the position and attitude estimation of precision aerial delivery systems". In: *Sensors* 20.18 (Sept. 2020), p. 5227. ISSN: 1424-8220. DOI: 10.3390/s20185227.

[Gong-19] Z. Gong, R. Ying, F. Wen, J. Qian, and P. Liu. "Tightly coupled integration of GNSS and vision SLAM using 10-DoF optimization on manifold". In: *IEEE Sensors J.* 19.24 (Dec. 2019), pp. 12105–12117. DOI: 10.1109/JSEN.2019.2935387.

[Goodrick-75] T. Goodrick. "Theoretical study of the longitudinal stability of high-performance gliding airdrop systems". In: *5th Aerodynamic Deceleration Syst. Conf.* Albuquerque, NM, USA, Nov. 1975, pp. 1–10. DOI: 10.2514/6.1975-1394.

[Goodrick-79] T. Goodrick. "Simulation studies of the flight dynamics of gliding parachute systems". In: *6th Aerodynamic Decelerator and Balloon Technol. Conf.* Houston, TX, USA, Mar. 1979, pp. 1–6. DOI: 10.2514/6.1979-417.

[Gorman-12] C. M. Gorman and N. Slegers. "Evaluation of multibody parafoil dynamics using distributed miniature wireless sensors". In: *J. Aircr.* 49.2 (Mar. 2012), pp. 546–555. DOI: 10.2514/1.C031566.

[Harwin-12] S. Harwin and A. Lucieer. "Assessing the accuracy of georeferenced point clouds produced via multi-view stereopsis from unmanned aerial vehicle (UAV) imagery". In: *Remote Sensing* 4.6 (May 2012), pp. 1573–1599. DOI: 10.3390/rs4061573.

[Jalbert-66] D. C. Jalbert. "Multi-cell wing type aerial device". U.S. pat. 3285546. Nov. 1966.

[Jann-01] T. Jann. "Aerodynamic model identification and GNC design for the parafoil-load system ALEX". In: *16th AIAA Aerodynamic Decelerator Syst. Technol. Conf. and Seminar*. Boston, MA, USA, Apr. 2001, pp. 1–12. DOI: 10.2514/6.2001-2015.

[Jann-05] T. Jann. "Advanced features for autonomous parafoil guidance, navigation and control". In: *18th AIAA Aerodynamic Decelerator Syst. Technol. Conf. and Seminar*. Munich, Germany, Apr. 2005, pp. 1–12. DOI: 10.2514/6.2005-1642.

[Jorgensen-05] D. Jorgensen and M. Hickey. "The AGAS 2000 precision airdrop system". In: *Infotech@Aerospace*. Arlington, VA, USA, Sept. 2005, pp. 1–11. DOI: 10.2514/6.2005-7072.

[Kaminer-03] I. Kaminer and O. Yakimenko. "Development of control algorithm for the autonomous gliding delivery system". In: *17th AIAA Aerodynamic Decelerator Syst. Technol. Conf. and Seminar*. Monterey, CA, USA, May 2003, pp. 1–15. DOI: 10.2514/6.2003-2116.

[Kingston-04] D. B. Kingston and R. W. Beard. "Real-time attitude and position estimation for small UAVs using low-cost sensors". In: *AIAA 3rd Unmanned Unlimited Tech. Conf., Workshop and Exhibit*. Chicago, IL, USA: American Institute of Aeronautics and Astronautics, Sept. 2004. ISBN: 978-1-62410-081-9. DOI: 10.2514/6.2004-6488.

[Knacke-91] T. W. Knacke. *Parachute Recovery System Design Manual*. Santa Barbara, CA, USA: Para Publishing, 1991.

[Lingard-86] J. S. Lingard. "The aerodynamics of gliding parachutes". In: *9th Aerodynamic Decelerator and Balloon Technology Conf.* Albuquerque, NM, USA, Oct. 1986, pp. 1–41.

[Lingard-95] J. S. Lingard. "Precision aerial delivery seminar ram-air parachute design". In: *13th Aerodynamic Decelerator Syst. Technol. Conf.* Clearwater Beach, FL, USA, May 1995, pp. 1–51.

[Lissaman-93] P. Lissaman and G. Brown. "Apparent mass effects on parafoil dynamics". In: *Aerosp. Des. Conf.* Irvine, CA, Feb. 1993. DOI: 10.2514/6.1993-1236.

[Manfreda-18] S. Manfreda et al. “On the use of unmanned aerial systems for environmental monitoring”. In: *Remote Sensing* 10.4 (Apr. 2018), pp. 1–28. DOI: 10.3390/rs10040641.

[Marucci-17] A. Marucci, A. Colantoni, I. Zambon, and G. Egidi. “Precision farming in hilly areas: the use of network RTK in GNSS technology”. In: *Agriculture* 7.7 (July 2017), pp. 1–10. DOI: 10.3390/agriculture7070060.

[Matosevic-06] M. Matosevic, Z. Salcic, and S. Berber. “A comparison of accuracy using a GPS and a low-cost DGPS”. In: *IEEE Trans. Instrum. Meas.* 55.5 (Oct. 2006), pp. 1677–1683. ISSN: 0018-9456. DOI: 10.1109/TIM.2006.880918.

[MeteoSwiss-20] Federal Office of Meteorology and Climatology MeteoSwiss. *Radio Soundings*. 2020. URL: http://www.meteoswiss.admin.ch/home/measurement-and-forecasting-systems/atmosphere/radio-soundings.html (visited on 2020).

[Mortaloni-03] P. Mortaloni, O. Yakimenko, V. Dobrokhodov, and R. Howard. “On the development of a six-degree-of-freedom model of a low-aspect-ratio parafoil delivery system”. In: *17th AIAA Aerodynamic Decelerator Syst. Technol. Conf. and Seminar*. Monterey, CA, USA, May 2003, pp. 1–10. DOI: 10.2514/6.2003-2105.

[NOAA-16] National Oceanic and Atmospheric Administration. *Integrated Global Radiosonde Archive*. National Centers for Environmental Information. 2016. URL: https://www.ncdc.noaa.gov/data-access/weather-balloon/integrated-global-radiosonde-archive (visited on 2018).

[NOAA-18] National Oceanic and Atmospheric Administration. *Weather Balloons*. National Weather Service. 2018. URL: https://www.weather.gov/bmx/kidscorner_weatherballoons (visited on 2018).

[Pajares-15] G. Pajares. “Overview and current status of remote sensing applications based on unmanned aerial vehicles (UAVs)”. In: *Photogrammetric Eng. & Remote Sensing* 81.4 (Apr. 2015), pp. 281–330. DOI: 10.14358/PERS.81.4.281.

[Park-20] S. Park and Y. Choi. “Applications of unmanned aerial vehicles in mining from exploration to reclamation: A review”. In: *Minerals* 10.8 (July 2020), pp. 1–31. DOI: 10.3390/min10080663.

[Peng-00] H.-M. Peng, Y.-T. Chiang, F.-R. Chang, and L.-S. Wang. “Maximum-likelihood-based filtering for attitude determination via GPS carrier phase”. In: *IEEE 2000. Position Location and Navigation Symp. (Cat. No.00CH37062)*. San Diego, CA, USA, Mar. 2000, pp. 480–487. DOI: 10.1109/PLANS.2000.838342.

[Quinchia-13] A. G. Quinchia, G. Falco, E. Falletti, F. Dovis, and C. Ferrer. "A comparison between different error modeling of MEMS applied to GPS/INS integrated systems". In: *Sensors* 13.8 (July 2013), pp. 9549–9588. DOI: 10.3390/s130809549.

[Reisdorf-16] P. Reisdorf et al. "The problem of comparable GNSS results – An approach for a uniform dataset with low-cost and reference data". In: 5th Int. Conf. Advances in Veh. Syst., Technol. and Appl. Barcelona, Spain, Nov. 2016. ISBN: 978-1-61208-515-9. URL: https://www.iaria.org/conferences2016/VEHICULAR16.html.

[Rodríguez-Pérez-07] J. R. Rodríguez-Pérez, M. F. Álvarez, and E. Sanz-Ablanedo. "Assessment of low-cost GPS receiver accuracy and precision in forest environments". In: *J. of Surveying Eng.* 133.4 (Nov. 2007), pp. 159–167. DOI: 10.1061/(ASCE)0733-9453(2007)133:4(159).

[Sabatini-11] A. M. Sabatini. "Kalman-filter-based orientation determination using inertial/magnetic sensors: Observability analysis and performance evaluation". In: *Sensors* 11.10 (Sept. 2011), pp. 9182–9206. DOI: 10.3390/s111009182.

[Sanz-Ablanedo-18] E. Sanz-Ablanedo, J. H. Chandler, J. R. Rodríguez-Pérez, and C. Ordóñez. "Accuracy of unmanned aerial vehicle (UAV) and SfM photogrammetry survey as a function of the number and location of ground control points used". In: *Remote Sensing* 10.10 (Oct. 2018), pp. 1–19. DOI: 10.3390/rs10101606.

[Scheiner-19] N. Scheiner et al. "Automated ground truth estimation for automotive radar tracking applications with portable GNSS and IMU devices". In: *2019 20th Int. Radar Symp.* Ulm, Germany, June 2019, pp. 1–10. DOI: 10.23919/IRS.2019.8768169.

[Shakhatreh-19] H. Shakhatreh et al. "Unmanned aerial vehicles (UAVs): A survey on civil applications and key research challenges". In: *IEEE Access* 7 (Apr. 2019), pp. 48572–48634. DOI: 10.1109/ACCESS.2019.2909530.

[Simon-06] D. Simon. *Optimal State Estimation: Kalman, H∞, and Nonlinear Approaches*. Hoboken, NJ, USA: Wiley, May 2006. ISBN: 978-0-470-04534-3. DOI: 10.1002/0470045345.ch5.

[Slegers-09] N. Slegers and O. Yakimenko. "Optimal control for terminal guidance of autonomous parafoils". In: *20th AIAA Aerodynamic Decelerator Syst. Technol. Conf. and Seminar*. Seattle, WA, USA, May 2009, pp. 1–21. DOI: 10.2514/6.2009-2958.

[Slegers-11a] N. Slegers and C. Gorman. "Comparison and analysis of multi-body parafoil models with varying degrees of freedom". In: *21st AIAA Aerodynamic Decelerator Syst. Technol. Conf. and Seminar*. Dublin, Ireland, May 2011, pp. 1–27. DOI: 10.2514/6.2011-2615.

[Slegers-11b] N. Slegers and O. A. Yakimenko. "Terminal guidance of autonomous parafoils in high wind-to-airspeed ratios". In: *Proc. Institution Mech. Engineers, Part G: J. Aerosp. Eng.* 225.3 (Mar. 2011), pp. 336–346. DOI: 10.1243/09544100JAERO749.

[Stempfhuber-11] W. Stempfhuber and M. Buchholz. "A precise, low-cost RTK GNSS system for UAV applications". In: *ISPRS - Int. Archives of the Photogrammetry, Remote Sensing and Spatial Inform. Sci.* XXXVIII-1/C22 (2011), pp. 289–293. DOI: 10.5194/isprsarchives-XXXVIII-1-C22-289-2011.

[STMicroelectronics-17] STMicroelectronics. *STM32F765 data sheet*. Available online: https://www.st.com/resource/en/datasheet/stm32f765zi.pdf. (accessed on 30 July 2020). Sept. 2017.

[Strickert-99] G. Strickert and T. Jann. "Determination of the relative motion between parafoil canopy and load using advanced video-image processing techniques". In: *15th Aerodynamic Decelerator Syst. Technol. Conf.* Toulouse, France, June 1999, pp. 1–8. DOI: 10.2514/6.1999-1754.

[u-blox-13] u-blox. *u-blox 6 receiver description. Including Protocol Specification*. Apr. 18, 2013. URL: https://www.u-blox.com/sites/default/files/products/documents/u-blox6_Recei%20verDescrProtSpec_(GPS.G6-SW-10018)_Public.pdf (visited on 07/2020).

[u-blox-20] u-blox. *u-blox M8 concurrent GNSS modules*. Apr. 30, 2020. URL: https://www.u-blox.com/sites/default/files/NEO-M8-FW3_DataSheet_%5C%28UBX-15031086%5C%29.pdf (visited on 07/2020).

[Ward-10] M. Ward, M. Costello, and N. Slegers. "On the benefits of in-flight system identification for autonomous airdrop systems". In: *J. of Guid., Control, and Dyn.* 33.5 (Sept. 2010), pp. 1313–1326. DOI: 10.2514/1.49030.

[Ward-11] M. Ward, A. Gavrilovski, and M. Costello. "Flight test results for glide slope control of parafoil canopies of various aspect ratios". In: *21st AIAA Aerodynamic Decelerator Syst. Technol. Conf. and Seminar*. Dublin, Ireland, May 2011, pp. 1–15. DOI: 10.2514/6.2011-2620.

[Ward-12] M. Ward, M. Costello, and N. Slegers. "Specialized system identification for parafoil and payload systems". In: *J. of Guid., Control, and Dyn.* 35.2 (Mar. 2012), pp. 588–597. DOI: 10.2514/1.53364.

[Ward-14] M. Ward, S. Culpepper, and M. Costello. "Parafoil control using payload weight shift". In: *J. Aircr.* 51.1 (Jan. 2014), pp. 204–215. DOI: 10.2514/1.C032251.

[Wolf-71] D. Wolf. "Dynamic stability of a nonrigid parachute and payload system". In: *J. Aircr.* 8.8 (Aug. 1971), pp. 603–609. DOI: 10.2514/3.59145.

[Yakimenko-09] O. Yakimenko, N. Slegers, and R. Tiaden. "Development and testing of the miniature aerial delivery system snowflake". In: *20th AIAA Aerodynamic Decelerator Syst. Technol. Conf. and Seminar*. Seattle, WA, USA, May 2009, pp. 1–15. ISBN: 978-1-60086-969-3. DOI: 10.2514/6.2009-2980.

[Yakimenko-16] O. A. Yakimenko. "Autonomous Parachute-Based Precision Delivery Systems". In: *Encyclopedia of Aerospace Engineering*. Hoboken, NJ, USA: Wiley, July 2016. ISBN: 978-0-470-68665-2. DOI: 10.1002/9780470686652.eae1104.

[Yang-20] Y. Yang, X. Liu, W. Zhang, X. Liu, and Y. Guo. "A nonlinear double model for multisensor-integrated navigation using the federated EKF algorithm for small UAVs". In: *Sensors* 20.10 (May 2020), pp. 1–23. DOI: 10.3390/s20102974.

[Zhang-19] M. Zhang, K. Li, B. Hu, and C. Meng. "Comparison of Kalman filters for inertial integrated navigation". In: *Sensors* 19.6 (Mar. 2019), pp. 1–26. DOI: 10.3390/s19061426.

Author Index

Subject Index